2017-03-01

The Development of a Vertical-Axis Wind Turbine Wake Model for Use in Wind Farm Layout Optimization with Noise Level Constraints

Eric Blaine Tingey
Brigham Young University

The Development of a Vertical-Axis Wind Turbine Wake Model for Use in Wind Farm Layout Optimization with Noise Level Constraints

Eric Blaine Tingey

A thesis submitted to the faculty of
Brigham Young University
in partial fulfillment of the requirements for the degree of

Master of Science

Andrew Ning, Chair
Julie Crockett
Steven Gorrell

Department of Mechanical Engineering

Brigham Young University

ABSTRACT

The Development of a Vertical-Axis Wind Turbine Wake Model for Use in
Wind Farm Layout Optimization with Noise Level Constraints

Eric Blaine Tingey
Department of Mechanical Engineering, BYU
Master of Science

This thesis focuses on providing the means to use vertical-axis wind turbines (VAWTs) in wind farms as an alternative form of harnessing wind energy in offshore and urban environments where both wake and acoustic effects of turbines are important considerations. In order for VAWTs to be used in wind farm layout analysis and optimization, a reduced-order wake model is needed to calculate velocities around a turbine quickly and accurately. However, a VAWT wake model has not been available to accomplish this task. Using vorticity data from computational fluid dynamic (CFD) simulations of VAWTs and cross-validated Gaussian distribution and polynomial surface fitting, a wake model is produced that can estimate a wake velocity deficit of an isolated VAWT at any downstream and lateral position based on nondimensional parameters describing the turbine speed and geometry. When compared to CFD, which takes over a day to run one simulation, the wake model predicts the velocity deficit at any location with a normalized root mean squared error of 0.059 in about 0.02 seconds. The model agrees with two experimental VAWT wake studies with a percent difference of the maximum wake deficit of 6.3% and 14.6%. Using the actuator cylinder model with predicted wake velocities of multiple turbines, aerodynamic loads can be calculated on the turbine blades to estimate the power production of a VAWT wind farm.

As VAWTs could be used in urban environments near residential areas, the noise disturbance coming from the turbine blades is an important consideration in the layout of a wind farm. Noise restrictions may be imposed on a wind farm to limit the disturbance, often impacting the wind farm's power producing capability. Two specific horizontal-axis wind turbine farm designs are studied and optimized using the FLORIS wake model and an acoustic model based on semi-empirical turbine noise calculations to demonstrate the impact a noise level constraint has on maximizing wind farm power production. When a noise level constraint was not active, the average power production increased, up to 8.01% in one wind farm and 3.63% in the other. Including a noise restriction in the optimization had about a 5% impact on the optimal average power production over a 5 decibel range. By analyzing power and noise together, the multi-modality of the optimization problem can be used to find solutions were noise impact can be improved while still maximizing wind farm power production.

Keywords: vertical-axis wind turbine, wind farm optimization, wake model, turbine acoustics, computational fluid dynamics

ACKNOWLEDGMENTS

I would like to express my appreciation to my adviser, Dr. Andrew Ning, for his work and support of my research efforts. He has been a huge part of directing my research towards producing valuable results and providing insight into problems and questions I encounter. I admire his work ethic, focus, and commitment to helping his students become better people. I know that I have become a better student and researcher, as well as a better person, from his guidance and instruction. He has also helped me see the bigger picture of life and how to set myself up for success, not only for graduate school, but for my future career in the engineering field.

I would also like to thank the members of my graduate committee, Dr. Julie Crockett and Dr. Steven Gorrell, for their support in my research efforts. I have had the opportunity to take classes from both of them and I have appreciated the time they took to teach me about various fluids topics. Not only has it helped me better understand different aspects of my graduate research, but it has helped me see the importance these topics have in the world in creating better engineering solutions for society. They have both been very willing to meet with me and give me feedback and support with questions I have had during my research and educational pursuits. I would also like to recognize Dagan Pielstick for his work in the turbine computer simulations, programming and coding, and the other behind-the-scenes work to support this research effort.

During my time as a graduate student, I received the BYU Graduate Research Fellowship from the BYU Graduate Society for which I am also grateful. It helped me financially to attend graduate school at BYU as well as assisting my travel to San Diego for an AIAA conference I attended to present my work on VAWT wake research to an academic audience. I was able to network with individuals in my field as well as learn about new advancements in all areas of aerospace research. It was a great opportunity to develop myself both academically and professionally.

My family and friends have also played a huge part in my ability to accomplish my research efforts. My parents and grandparents have always been a huge support to me in motivating me to follow my dreams and to do hard things they knew I could accomplish. They have often listened

to me practice presentations and talk through difficult concepts I am struggling to understand, and they have given me the motivation to keep pushing on even when things get tough. I am where I am with life due to their guidance, support, and love. The friends I have had throughout my BYU experience have also been a large part of my academic success. Working on tedious homework assignments and class projects late into the night can turn into happy memories if you do them with people who make the experience fun.

Finally, I would like to express my deep appreciation for my amazing wife, Megan, who has been a support to me throughout my graduate experience. It can be hard to have to spend evenings, weekends, and even holidays letting me run computer simulations, debug codes, or finish up a paper submission, but she has always been supportive of my work in allowing me to have the time needed to get things done well. She has also been supportive of me as I obtained valuable experiences through a study abroad, two engineering conferences, and a summer engineering internship. The needs of our home and family are always taken care of, even when I am not able to help, because of her efforts. I am truly grateful for such a faithful companion by my side.

TABLE OF CONTENTS

LIST OF TABLES

LIST OF FIGURES

NOMENCLATURE

A_s	swept area of turbine blades
a	starting point of downstream wake integration (turbine location)
α	angle of attack of a blade section used in the BPM equations
B	number of turbine blades
b	ending point of downstream wake integration
β_r	rotation position of turbine blades
C_f	skin friction of a surface
C_P	turbine power coefficient
C_T	tangential force coefficient
c	turbine blade chord length
c_0	speed of sound
c_2	distance from the pitch axis of a turbine blade to the trailing edge
D	turbine diameter
d	radial position along a blade from the hub of a HAWT
δ	boundary layer thickness
δ^*	boundary layer displacement thickness
δ_b	blade curvature angle
f	noise frequency used in BPM equations
γ	vorticity strength
H_{hub}	turbine hub height
h	trailing edge thickness of blade section
ht	height position along a blade from the bottom of a VAWT
κ	skew parameter of the exponentially modified Gaussian distribution
L	length of a blade segment in BPM equations
l	spanwise extent of the blade tip vortex shedding
λ	tip-speed ratio (TSR) $= (\Omega R)/U_\infty$
M	Mach number $= V/c_0$
M_c	convective Mach number
μ	location parameter of the exponentially modified Gaussian distribution
ν	kinematic viscosity
Ω	rotation rate
ω	vorticity
P	power production
P_{wind}	available wind energy
$P_{turbine}$	turbine power production
Φ_e	blade span reference directivity angle to observer location used in BPM equations
Ψ	solid angle between the sloping surfaces upstream of the trailing edge of a blade section
ψ	spread parameter of the exponentially modified Gaussian distribution
R	turbine radius
Re	Reynolds number $= (Vc)/\nu$
r_e	observer distance from a noise source (a turbine blade in the case of this thesis)
ρ	air density
s	spacing between two turbines

St	Strouhal number $= (f\delta)/V$
σ	solidity $= (Bc)/R$
τ_w	wall shear stress
Θ_e	blade chord reference directivity angle to observer location used in BPM equations
U_∞	free stream wind velocity
u	x-component of velocity (downstream direction)
u_*	friction velocity of a surface
u_b	x-component of velocity due to blade interaction (downstream direction)
u_w	x-component of velocity due to exterior wake interaction (downstream direction)
$\hat{u}$	predicted velocity deficit
V	wind velocity (typically in the downstream direction or over the blades of the turbine)
v	y-component of velocity (lateral direction)
v_b	y-component of velocity due to blade interaction (lateral direction)
v_w	y-component of velocity due to exterior wake interaction (lateral direction)
w	lateral extent of wake integration
y_w	y^+ wall value
ζ	scale parameter of the exponentially modified Gaussian distribution

CHAPTER 1. INTRODUCTION

Wind is a valuable source of alternative energy because it is renewable, available in many parts of the world, and has the ability to produce twenty times more power than the world currently consumes [15]. Recently, there has been increased interest in using turbines in offshore locations, where the wind is stronger and more consistent than land-based locations [16], as well as urban environments closer to population centers [17]. Vertical-axis wind turbines have shown promise in these environments due to their easy maintenance access, effective operation independent of wind direction, and ability to produce more power when placed close together [18, 19]. However, the ability to calculate wind velocities between turbines in a wind farm quickly and accurately is necessary to produce an optimal wind farm layout design—an ability not available for vertical-axis wind turbines. If turbines are located near residential areas, noise disturbance must also be considered in the layout of the wind farm. The purpose of this thesis is to provide a way to use vertical-axis wind turbines in wind farm layout optimization with noise level constraints through the development of a reduced-order wake model and the implementation of turbine acoustic modeling.

This chapter includes a brief overview of wind turbines and their operational dynamics, including an introduction to turbine wakes and turbine noise. Following this overview, the purpose of the thesis and its contributions to the field of wind energy are explained. Finally, an outline of the rest of the thesis is provided.

1.1 Wind Turbines

Wind turbines convert wind energy flowing over their blades into usable electrical power through the use of several internal mechanisms that work together to ultimately spin a power generator. These various mechanisms include gears, sensors, brakes, and adjustment controls that maintain the turbine's rotation rate, the pitch of the blades, and the direction the turbine faces, as illustrated in Fig. 1.1. A turbine's potential in converting the wind energy to electrical power

depends on the efficiency of these different mechanisms working together. Wind can turn turbine blades either through drag (the force in the direction of the wind flow) or lift (the force perpendicular to the wind flow), and while drag-based turbines do exist, lift-based turbines are typically more efficient for producing power and are the type of turbine considered in this research [20]. Often, many wind turbines are grouped together within specified boundaries, called a wind farm, in order to increase power production for a given area of land.

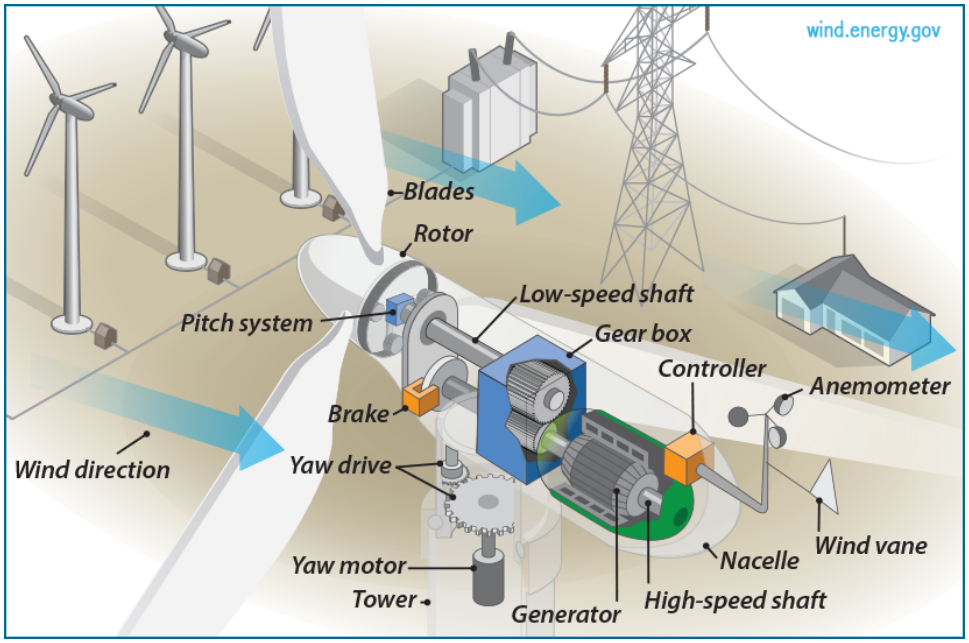

Figure 1.1: A diagram of the internal systems of a horizontal-axis wind turbine from the U.S. Department of Energy with blue arrows indicating wind moving in the downstream direction [2].

Horizontal-axis wind turbines (HAWTs) are traditionally used in secluded, land-based locations and efficiently produce the majority of the wind power used worldwide [15]. Their efficiency comes from the blades continuously engaging the incoming wind as they rotate around a horizontal axis. While HAWTs are currently the main source of harnessing wind energy, their tower height and size of the blades needed to capture large amounts of wind energy present financial and logistic challenges for HAWTs used in offshore and urban environments [16, 21]. Increased maintenance costs of HAWTs also come from the required yaw and pitch systems used to align the turbine with the wind direction and regulate power [15].

Vertical-axis wind turbines (VAWTs) address some of these challenges with their simpler design and operation, especially for use in offshore and urban environments. Access to the VAWT's mechanical systems is easier, particularly in unstable ocean environments, as these systems can be located near the base of the turbine [18]. VAWTs are typically smaller than HAWTs and can be placed much closer together making them more ideal for crowded urban environments [15], and research has even indicated that the close placement of VAWT pairs can increase their overall power production [10, 11, 19]. Additionally, VAWTs operate independently of wind direction, eliminating the need for a complex yaw system. These features make VAWTs a potential concept for more effective offshore and urban power production [18, 22]. An example of an H-rotor VAWT design from Uppsala University in Sweden can be seen in Fig. 1.2, which is used as the model for the computer simulations presented later in this thesis [3].

Figure 1.2: A computer model based on the 12 kW H-rotor VAWT found at Uppsala University in Sweden [3].

During the design of a wind farm layout, many aspects are considered, such as geography and electrical infrastructure, to make the energy conversion process efficient and the wind farm

financially and logistically feasible. While there are several aspects that are considered in actual wind farm layout designs, this thesis focuses on two main areas: turbine wakes and turbine noise.

1.1.1 Turbine Wakes and Reduced-Order Wake Modeling

As turbines extract energy from the wind, there is a reduction in wind momentum and increased turbulence behind the turbine. This region is called a wake, and as wakes propagate, the interference with downwind turbines can significantly impact their power production, as shown in Fig. 1.3, potentially costing a wind farm millions of dollars annually [23–25]. Due to this impact, efforts are made to position turbines in such a way that minimizes the wake interference. This can be accomplished using wind farm analysis and optimization where the wind velocity profile throughout the wind farm is calculated using wake modeling.

Figure 1.3: An example of wind turbine wake interference from Horns Rev Wind Farm in Denmark. (Christian Steiness/Vattenfall, "Horns rev offshore wind farm," January 13, 2010 via Flickr, Creative Commons Attribution)

Because calculating the wind velocity behind a turbine is a very complex process involving fluid dynamics and turbine blade interactions, accurate high-fidelity wake modeling is typically computationally expensive and time consuming. As explained in Chapter 3, computer simulations

of a single turbine wake used in this research took over a day to run using 64 parallel processors. Reduced-order wake models, which simplify the complex wake behavior into fundamental mathematical relationships, offer an improvement to high-fidelity wake modeling by calculating the wind velocity much faster. Optimization of wind farm layouts with reduced-order wake models for HAWTs has been studied extensively [14, 26–31]. These past research efforts have found optimized layouts of wind farms that maximize power production mainly by minimizing the negative effects of turbine-wake interactions. However, a reduced-order wake model has not been available to perform similar wind farm layout studies of VAWTs.

Although a VAWT wake model has not been available, there have been several studies involving the operation of VAWTs and the wakes they produce. Sandia National Laboratories conducted research in the 1970s and 1980s comparing the performance of different types of VAWT designs, which produced a compilation of blade aerodynamic properties and power for various VAWT configurations [32–34]. More recently, Delft University of Technology in the Netherlands conducted research based on the near wake formation of VAWTs using particle image velocimetry (PIV) that provided significant insight into the near wake development of VAWTs and a knowledge of contributing factors in turbine wake behavior [7, 35–38]. Shamsoddin and Porté-Agel also conducted wake research looking further downstream of a VAWT using large eddy simulation (LES) modeling, matching the wake velocities of a previous water tunnel experiment with an 87% accuracy [39].

There have also been some efforts to create a VAWT wake model for wind farm applications. Research at the California Institute of Technology proposed a wake model using a single point vortex and a doublet to simulate a VAWT (rotating cylinder flow) with simple expansion and decay models to predict the wake velocity distribution [40]. It was a good first step for a VAWT wake model, but could not be used in a generalized sense because it was tuned to a specific turbine. Hesaveh et al. recently developed a VAWT wake model based on actuator line theory, LES, and Reynolds-averaged Navier-Stokes equations [41], but the computational cost of its high-fidelity wake modeling techniques makes it difficult for use in large-scale wind farm layout optimization. For VAWTs to be used effectively in wind farm optimization, a robust and parameterizable reduced-order wake model is needed that can predict the wake velocities within the wind farm with a low computational cost.

1.1.2 Turbine Noise and Acoustic Modeling

Wind turbine noise generation is another important consideration for wind farm layout optimization as this noise can cause disturbances to residential areas located in the vicinity of wind farms, especially in urban environments. While the sound coming from wind turbines poses no physical or psychological harm to humans, it can be an annoyance to individuals living near wind farms [1]. The annoyance from turbine noise can potentially limit the areas available to build wind farms to remote locations away from populated regions, require costly alterations of the turbine blades to make them quieter, or slow the turbines' rotation rate and decrease the power production of the wind farm. Ideally, a wind farm layout should constrain the turbine noise disturbance during the initial design process below a specified limit while maximizing power output. This noise limit varies throughout the world, ranging from 35 to 60 decibels—about the loudness of a refrigerator to the loudness of a normal conversation [42–44]. The main source of turbine noise is the turbulence-induced noise from the wind flowing over the blades [45], which is illustrated in Fig. 1.4. While other sources of noise exist, such as the noise of the mechanical systems or the interaction of the blades with the tower, the noise coming from the blades is the type of noise explored in this research.

Wind farm layout optimization that considers turbine acoustics has not been studied extensively, but previous research efforts performed by Kwong et al. and Sorkhabi et al. produced an analysis of a HAWT layout optimization using a simple wake model and the ISO-9613-2 standard that predicted only the propagation of turbine noise [46, 47]. From these studies, they showed that turbines could be arranged in a way that allowed the wind farm to trade off power production for turbine noise. These trade-offs are important to consider when designing a wind farm layout in order to reduce the noise disturbance while still maximizing the power production. As the turbulence of wake interactions between turbines also affect the noise produced by turbines, noise calculations are made based on inflow velocities in front of turbines with respect to wake interference.

1.2 Research Purpose

This thesis focuses on establishing a way to use VAWTs effectively in wind farm layout analysis and optimization with noise level constraints. To accomplish this purpose, a reduced-

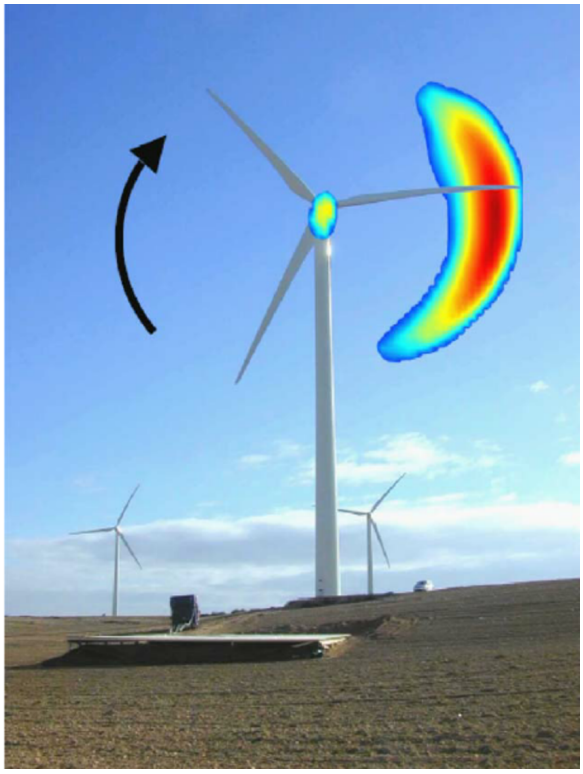

Figure 1.4: An illustration of a G58 wind turbine with an averaged acoustic distribution of the blades projected on the picture, taken from the work of Oerlemans et al. [4]

order, parameterizable VAWT wake model is developed based on higher-fidelity computer modeling. The wake data used in developing the model is obtained from many computer simulations of a VAWT to allow the wake model to be robust and applicable to a wide range of turbines. Cross-validated Gaussian distribution and polynomial surface fitting of the wake data allows the model to have robust predictive ability, especially at conditions where the computer simulations were not run. The results of the wake model are compared to computational and numerical data to demonstrate the wake model's accuracy. By extending the model's ability to predict multiple wake interaction with aerodynamic blade loading to calculate turbine power, the developed wake model has the potential to meet the needs of wind farm layout analysis and optimization with low computational costs.

The next part of the thesis addresses how limiting noise affects the power production of a wind farm, as VAWTs could be used in urban environments near residential areas. Two case studies using traditional HAWT wind farm layouts are presented that illustrate how limiting the noise

level of a wind farm can affect its average power production. In the previous studies of Kwong et al. and Sorkhabi et al. exploring how acoustics affect the results of wind farm layout optimization, a gradient-free optimization was used along with a simple wake model and an acoustic model that only predicted propagation with respect to atmospheric conditions [46, 47]. The previous studies also allowed turbines to be moved only to predetermined locations, limiting the potential of maximizing a wind farm's power production. In this research, a gradient-based optimization approach is used and turbines are allowed to move freely within the bounds of the wind farm. A more accurate wake model and an acoustic model that predicts noise levels based on the turbine's geometry, rotation rate, and distance from an observer are implemented to gain a better understanding of the effects that noise restrictions have on a wind farm layout. Adjustments made to the acoustic model to allow the use of VAWTs in similar acoustic studies are also described.

1.3 Thesis Outline

To outline the remainder of the thesis, Chapter 2 covers fundamental topics relating to wind energy, fluid dynamics, acoustics, and optimization. Chapter 3 describes the development of the reduced-order VAWT wake model using material from a conference paper presented at the 2016 ASME Wind Energy Symposium and a pending journal article submitted to the *AIAA Journal* [48, 49]. This chapter also discusses the work to account for multiple turbine wake interaction and power calculations from aerodynamic blade loading. Chapter 4 discusses two case studies of trading off the acoustic measurement of sound pressure level and the average power production of HAWT wind farms, based on a conference paper presented at the 2015 IEEE Conference on Technologies for Sustainability and the work of a pending journal article submitted to *Renewable Energy* [50, 51]. Chapter 5 concludes the thesis covering the main points of the research as well as areas for future work.

CHAPTER 2. TURBINE WAKE AND ACOUSTIC FUNDAMENTALS

In this chapter, some fundamental principles are addressed to better understand the processes needed to use VAWTs in wind farm layout optimization with acoustic constraints. The following sections describe relevant aerodynamic principles of turbine wakes, turbine acoustic modeling, and techniques used in wind farm layout optimization.

2.1 Aerodynamics of Turbine Wakes

The previous chapter described turbine wakes and the impacts they can have on the functionality of a wind farm. As discussed, wake regions have less momentum and more turbulence, making it difficult for turbines to extract wind energy. Two measures of the wake region's influence on turbine power production are velocity and vorticity. Wind velocity (V, or U_∞ when describing the free stream wind velocity) is simply a measure of how fast the wind is moving, and it is used in describing the energy available in the wind (P_{wind}) with the equation:

$$P_{wind} = \frac{1}{2}\rho A_s U_\infty^3 \tag{2.1}$$

where ρ is the air density and A_s is the area swept by the blades of the turbine. As seen in the equation, the available wind energy is significantly affected by velocity as a unit change in velocity impacts the available wind energy by a power of three. Minimizing the negative wake interference and wind speed reductions in a wind farm is important to maximize the available wind energy for the turbines.

While the energy available to be extracted exists in the wind, wind turbines are not capable of extracting all of this wind energy. The turbine's ability to extract wind energy is described using a power coefficient (C_P) and is specific to the design and operation of each turbine. The theoretical maximum C_P value a turbine could attain, known as the Betz limit, is 16/27 (0.593) and HAWTs

generally peak of around 0.5 while VAWTs peak around 0.4 [52]. Using the C_P value, the power production of a turbine ($P_{turbine}$) can then be calculated with:

$$P_{turbine} = C_P P_{wind} = C_P \frac{1}{2} \rho A_s U_\infty^3 \tag{2.2}$$

Vorticity (ω) is a measure of the rotation of the wind flow in the wake and is related to two-dimensional velocity using the equation:

$$\vec{\omega} = \nabla \times (V_x, V_y, 0) = 0\vec{x} + 0\vec{y} + \left(\frac{\partial V_y}{\partial x} - \frac{\partial V_x}{\partial y} \right) \vec{z} \tag{2.3}$$

As described in Chapter 3, vorticity is used as a basis of the wake velocity and the relationships in Eq. (2.3) are implemented to transform the vorticity data obtained from the computer simulations in the z-direction into velocity data in the x- and y-directions for the wake model development.

Two other nondimensional measures of turbine speed and geometry used in this thesis are tip-speed ratio (TSR; λ) and solidity (σ). The TSR is a ratio of how fast the turbine is rotating with respect to the incoming wind, defined by:

$$\lambda = \frac{\Omega R}{U_\infty} \tag{2.4}$$

where Ω is the rotation rate and R is the turbine radius. TSR is often used in power plots to determine the turbine speed that produces peak turbine performance.

Solidity is a measure of how much wind can flow freely through the turbine and is calculated by:

$$\sigma = \frac{Bc}{R} \tag{2.5}$$

where B is the number of turbine blades and c is the blade chord length. Higher solidities mean that more area is covered by the turbine blades reducing the air flow passing through the turbine and lower solidities indicate that more area is available for free air flow through the turbine, both illustrated in Fig. 2.1. TSR and solidity are used later in Chapter 3 as nondimensional values in the wake model parameterization.

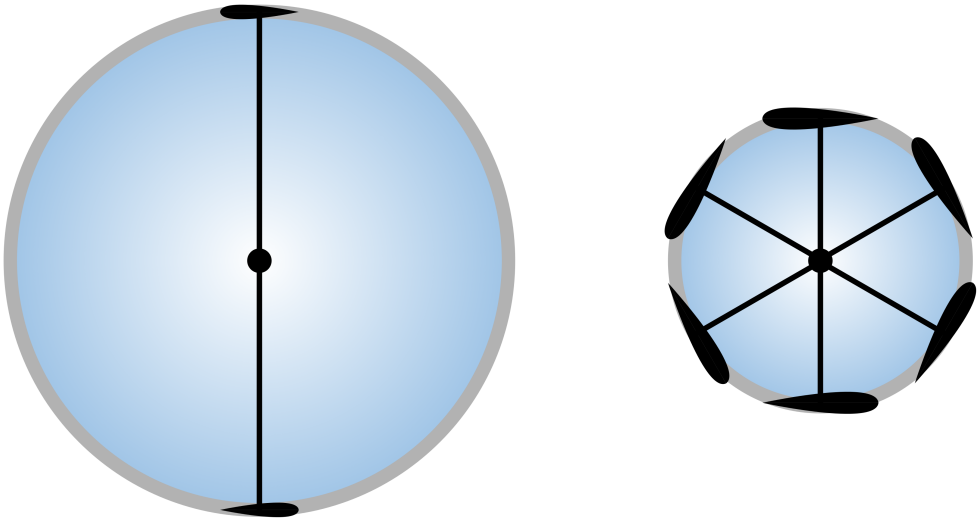

Figure 2.1: Examples of VAWTs with low solidity (left) and high solidity (right).

2.2 Turbine Acoustics

The noise produced by turbines comes from several sources along the turbine blades, tower, and mechanical systems. In order for turbine noise to be included in an optimization, models and equations are developed to predict the sound. The model chosen for describing turbine noise in this thesis is based on the equations developed for HAWT acoustics by Brooks, Pope, and Marcolini (described as the BPM acoustic equations) due to their ability to parameterize the noise by geometry and speed of the turbine [5]. The BPM equations describe different sources of noise: the trailing edge of the turbine blade and vortex shedding from the laminar boundary layer, the bluntness of the trailing edge, the tips of the blades, and noise coming from separation stall. Each of these sources produce a sound pressure level (SPL) measured in decibels (dB) and a representation of each of these noise sources can be seen in Fig. 2.2. The SPL from each noise source is added together using:

$$SPL_{total} = 10 \log \left(\sum_{i=1}^{N} 10^{SPL_i/10} \right) \tag{2.6}$$

for N noise sources to produce a total SPL coming from the turbine blades.

The noise level perceived from the turbine depends on the orientation and distance an observer is from the trailing edge of a turbine blade. To account for these factors, directivity functions

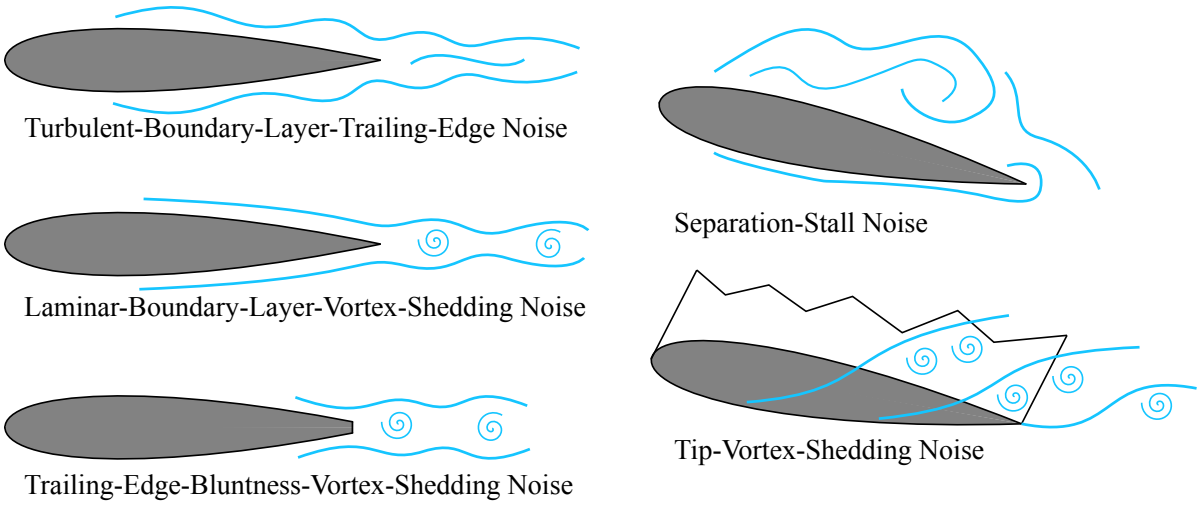

Figure 2.2: Illustrations of the turbine blade noise sources used in the BPM equations.

are used based on the angular position from the blade to an observer in the chord reference (Θ_e) and span reference (Φ_e) and the distance between the turbine blade and an observer (r_e). These area all illustrated in Fig. 2.3, and the noise is loudest when both angular positions approach 90° or 270°. As HAWT blades rotate in a single plane with small angles of attack, a dipole-shaped acoustic distribution is produced, as shown in Fig. 2.4, where the noise is loudest upstream and downstream of the turbine and quieter to the sides.

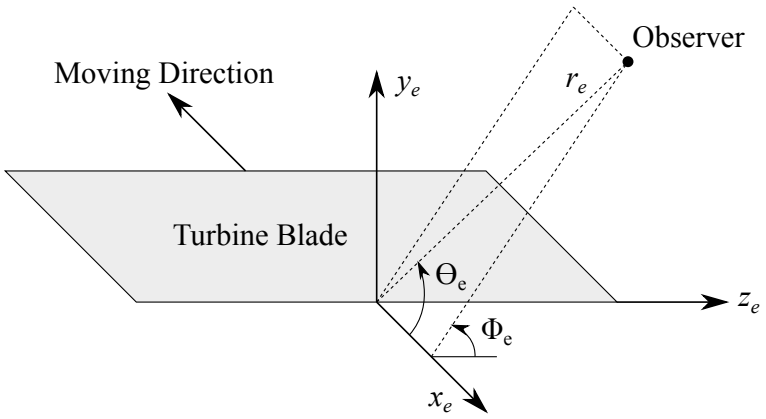

Figure 2.3: A diagram indicating important parameters used for the directivity functions, adapted from the work of Brooks et al. [5]

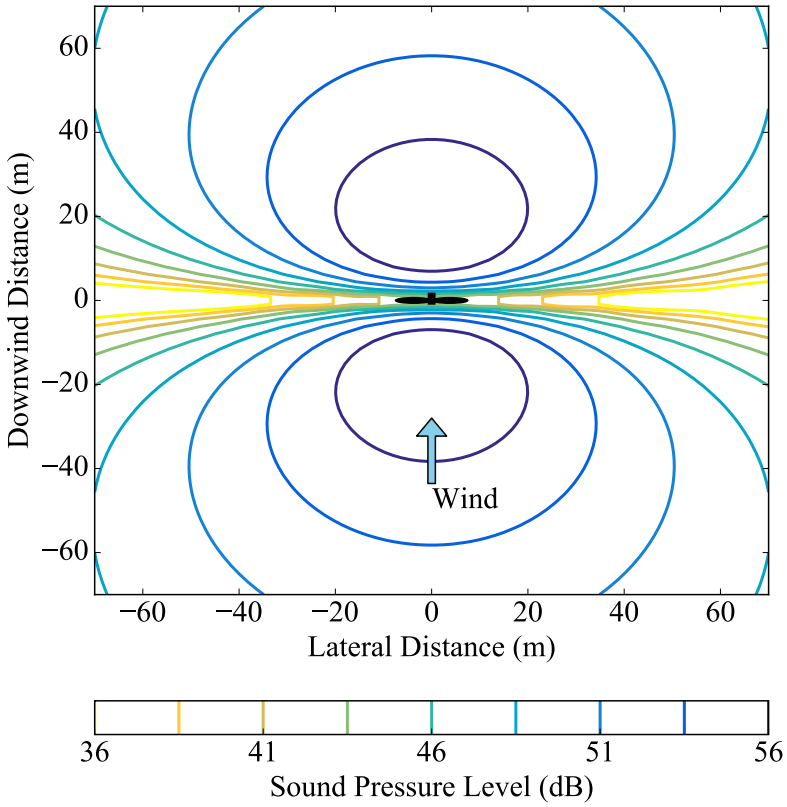

Figure 2.4: An example of the sound pressure level distribution calculated by the BPM equations for the Atlantic Orient Corporation 15/50 turbine in 8 m/s wind with three 7.5-meter long blades rotating at a rate of 64.6 RPM [6]. The sound pressure level measurement, in decibels (dB), is calculated for an observer at a given lateral and downwind position from the turbine, in meters, at ground level.

These semi-empirical equations were all developed using NACA 0012 airfoil data and validated with experimental studies by Brooks et al. [5] Later work by Moriarty and Migliore compared the equations with different configurations of blade shapes and wind speeds and found mixed results with the acoustic model predicting SPLs within 2 dB of experimental data in some configurations and 6 dB or more in other configurations, the best results coming from using a NACA 0012 airfoil [6]. The use the BPM acoustic equations provided a way to predict the noise levels of a wind farm for layout optimization based on the position of each turbine from observer locations and the turbine rotation rates. The implemented acoustic code in this thesis was validated against the FAST Noise code from NREL [6], producing the acoustic distribution in Fig. 2.4. The com-

plete description of the BPM equations used in this thesis and how they are implemented can be found in Appendix C.

One important understanding of noise mechanics is that decibels are measured on a logarithmic scale rather than a linear scale. This means that twice the loudness perceived by the human ear corresponds to about a 10 dB increase. An example decibel scale can be seen in Table 2.1, taken from the report of the American Wind Energy and Canadian Wind Energy Association [1]. As described in the previous chapter, wind turbines heard by residential areas are generally in the range of 35-60 dB [42–44].

Table 2.1: Typical Sound Pressure Levels Measured in the Environment and Industry [1]

Noise Source at a Given Distance	A-Weighted Sound Level in Decibels	Qualitative Description
Carrier deck jet operation	140	
	130	Pain threshold
Jet takeoff (200 feet)	120	
Auto horn (3 feet)	110	Maximum vocal effort
Jet takeoff (1000 feet)	100	
Shout (0.5 feet)		
N.Y. subway station	90	Very annoying
Heavy truck (50 feet)		Hearing damage (8-hour, continuous exposure)
Pneumatic drill (50 feet)	80	Annoying
Freight train (50 feet)	70 to 80	
Freeway traffic (50 feet)		
	70	Intrusive (Telephone use difficult)
Air conditioning unit (20 feet)	60	
Light auto traffic (50 feet)	50	Quiet
Living room	40	
Bedroom		
Library	30	Very quiet
Soft whisper (5 feet)		
Broadcasting/Recording studio	20	
	10	Just audible

2.3 Optimization Techniques

In any optimization, an algorithm is used to navigate the design space and find the minimum function value. This can be done by sampling a large number of points in the design space and comparing their function values to each other. This process, known as gradient-free optimization, can be very computationally expensive as function values must be calculated at each of the many points every iteration. An alternative method of optimization uses gradients, or slopes of the functions, allowing the optimizer to be guided through the design space at each iteration to smaller function values and requiring significantly fewer function calls. In order for a gradient-based optimization to operate correctly, evaluated function values must be smooth and continuous to allow the optimizer to identify a new value each iteration. This research implements a gradient-based optimization technique with finite-differencing to compute gradients through the use of the Sparse Nonlinear OPTimizer (SNOPT), a sequential quadratic programming optimizer used for solving large, nonlinear problems [53].

CHAPTER 3. VERTICAL-AXIS WIND TURBINE WAKE MODEL

As described in Chapter 1, wind farm power production depends largely on the amount of wake interference between turbines. Reduced-order wake models allow researchers to use wind farm layout optimization to study turbine layouts and obtain both wind velocity and power production data of the farm relatively quickly. However, as previously addressed, a reduced-order wake model for VAWTs to be used in optimization has not been available. In this chapter, the development of a reduced-order, parameterizable wake model for VAWTs is presented, including the computer simulations of VAWT wakes, the trend analysis of the wake data, and the validation studies of the developed wake model with experimental results. Methods are also described to account for multiple turbine wake interaction and the power calculation of a VAWT based on the aerodynamic loading of the blades.

3.1 CFD Turbine Simulations

In order to perform an analysis or optimization of a wind farm, wake models are used to provide accurate wind speed calculations around the turbines in a reasonable amount of time. If a wake model is created based on a very specific configuration of a turbine, it becomes less useful for generalized wind farm analysis. As a robust parametric wake model that could be applied to a wide range of turbines is needed for wind farm studies, wake data at many different wind speeds, rotation rates, and turbine geometries was obtained to form the basis of the model. The data was obtained using computational fluid dynamics (CFD) software, which was faster and simpler than obtaining the data experimentally. Using the CFD program from CD-adapco called STAR-CCM+, an isolated VAWT was simulated with different speed and geometry configurations using unsteady, two-dimensional Reynolds-averaged Navier-Stokes equations, each which took a little over a day to run on the local BYU supercomputer using 64 processors. The VAWT was modeled in 2D rather than 3D as the fundamental process of energy conversion of a VAWT happens in the plane

normal to the turbine's axis of rotation [35]. While a 2D simulation does not account for finite blade effects, such as trailing and tip vortices, it provided a way to systematically obtain the large amount of wake data reasonably quickly due to simpler wake calculations.

Verification and validation of the CFD model was necessary to ensure that the model was refined enough and was producing results comparable to experimental data. For the verification, a grid convergence study was performed based on the design of the 12 kW H-rotor VAWT from Uppsala University in Sweden with a 6-meter diameter and three NACA 0021 blades, each with a chord length of 0.25 meters (illustrated in Fig. 1.2) [3]. The wind speed was set at 15 m/s producing a Reynolds number of about 6,000,000. Keeping the tip-speed ratio at 3.25 (about the peak of performance from the experimental study of Kjellin et al. [3]), simulations using STAR-CCM+ were run ranging from cell counts of about 400,000 to almost 5 million by reducing the base cell size of the CFD model by a factor of 1.4 each time. The turbine power coefficient was monitored and reported at each cell count, and the results of this grid convergence study comparing the CFD cell count with the turbine power coefficient can be seen in Fig. 3.1.

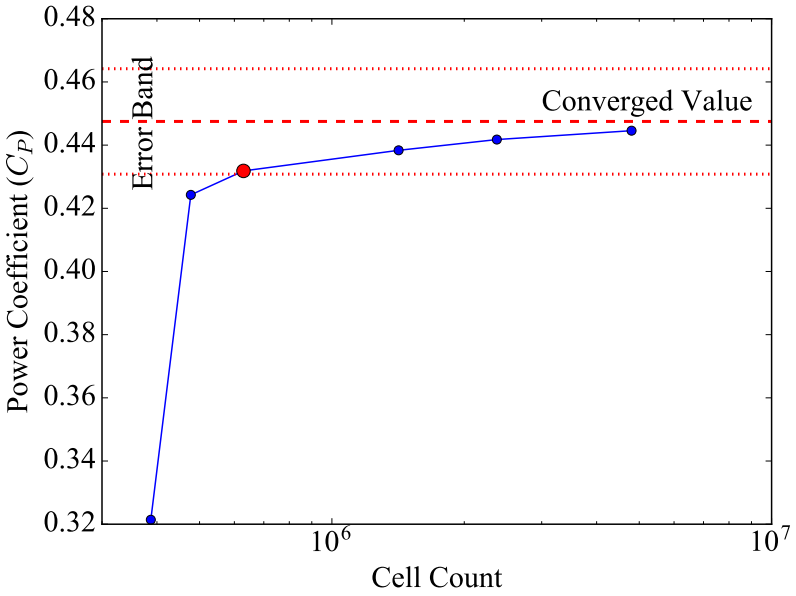

Figure 3.1: A plot of the grid convergence of the CFD model at a tip-speed ratio of 3.25. The converged power coefficient calculated with Richardson extrapolation (dashed line) as well as the error band of the converged value (dotted lines) are shown. The cell count used in the research is indicated by the red dot at about 630,000 cells.

Using Richardson extrapolation, the converged power coefficient was calculated to be 0.447 with an error band of 3.73%, both indicated in Fig. 3.1. In ideal circumstances, one would run the CFD models as refined as possible, but further refinement means more computational time of the CFD solution. Therefore, a balance must be made between computational run time and sufficient refinement. In this case, a cell count of about 630,000 cells was selected for the CFD model as it produced a power coefficient of 0.432, which was within the error band, and provided results in a little over a day (this point is indicted by the red dot in Fig. 3.1).

The wake velocity of the CFD model was also validated to ensure that the CFD cell size was refined enough in the wake region. To do this, a study conducted by Tescione et al. was used where a small turbine was tested in a wind tunnel at Delft University of Technology and velocities were measured with particle image velocimetry (PIV) [7]. The turbine consisted of two straight NACA 0018 blades with a chord length of 0.06 meters. The turbine had a diameter of 1.0 meter and solidity of 0.24. The VAWT was tested in a wind speed of 9.3 m/s, producing a Reynolds number of about 600,000, and run at a tip-speed ratio of 4.5. Plots showing the calculated velocities using PIV and the CFD model at six downstream distances are shown in Fig. 3.2.

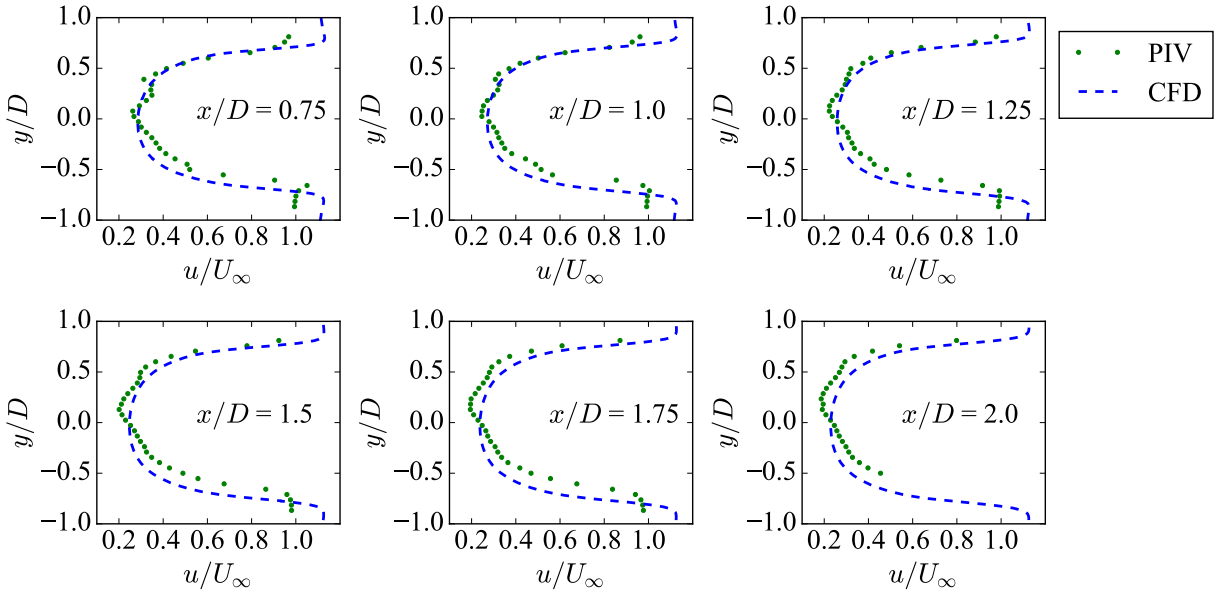

Figure 3.2: The wake velocity comparison between the PIV study conducted by Tescione et al. [7] and the CFD model. The velocity (u) is normalized by the free stream wind velocity (U_∞) and the downstream (x) and lateral (y) positions are normalized by the turbine diameter (D).

The CFD model was compared against the PIV data using the root mean squared (RMS) error normalized by the free stream wind velocity (U_∞), calculated by the equation:

$$RMS\ error = \frac{\sqrt{\frac{1}{N}\sum_{i=1}^{N}(u_i - \hat{u}_i)^2}}{U_\infty} \tag{3.1}$$

where u is the velocity deficit from the CFD model and $\hat{u}$ is the predicted velocity deficit from the experimental data for N data points. An RMS error was used in measuring wake comparison accuracy, as opposed to a relative error, because many of the velocity deficits were close to zero, causing the denominator to often be very small. The RMS error normalized by the free stream wind velocity of the CFD was 0.113 and the greatest percent difference in maximum velocity deficit was 5.8%. This difference, as well as the asymmetry of the experimental data, could be due to the differences of the three-dimensional experimental setup with the ideal wind conditions of the two-dimensional CFD model. It is also reported in the experimental study that the asymmetry in the wake velocities is caused by wake self-induction and stronger vorticity on one side as well as the influence of the turbine tower [7]. The wake velocities from the CFD also exceed the free stream wind velocity approaching $y/D = \pm 1.0$ while the experimental velocity data remains below the free stream wind velocity. This could be a result of the wider domain of the CFD, which allows wind to speed up freely, as opposed to the constraints of the wind tunnel used for the experiment. The regions of increased wake velocity calculated by the CFD simulation correspond to similar results found by Shamsoddin and Porté-Agel leading to more confidence in the results [39].

The CFD models used in this research were created to obtain large amounts of wake data systematically rather than maximizing accuracy with experimental data. Therefore, the simplifications and differences of the two-dimensional CFD models resulting in small errors allowed for CFD simulations to be completed in a little over a day. The CFD modeled the rotating turbine blades and axis as no-slip walls in a fluid region consisting of velocity inlets and a pressure outlet. Prism layers were used to account for boundary layers with thicknesses ranging from 0.0005 to 0.024 meters and y^+ = 1.0 wall values ranging from 1.95e-5 to 2.33e-5 meters, depending on the chord length of the blade. Wake refinements were also made behind the turbine to more accurately capture wake velocities. A meshed CFD model is shown in Fig. 3.3 and a detailed overview of all the CFD settings and boundary layer equations can be found in Appendix A.

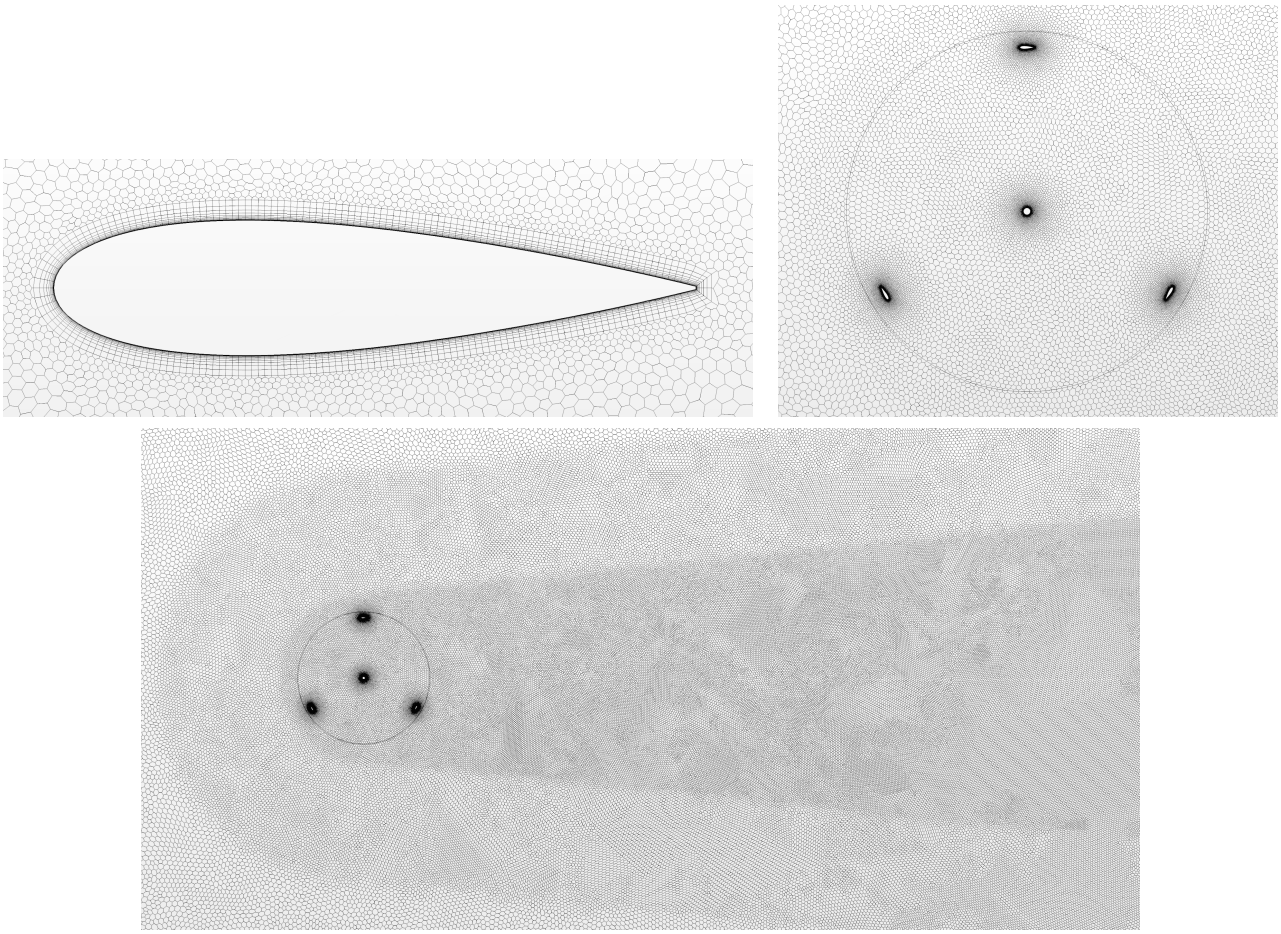

Figure 3.3: An example of the mesh used in the STAR-CCM+ VAWT simulations showing the turbine blade with prism layers, the rotating turbine region with finer meshing around the individual blades and turbine axis, and a far-field view showing the wake refinement regions.

3.2 CFD Data Analysis

Effective reduced-order wake models are made to be parameterized to calculate velocity under various operational circumstances. Nondimensional parameters allow a wake model to be generalized to a large range of turbines regardless of aspects like specific size or rotation rate of the turbine. In order to form a wake model based on relevant nondimensional parameters in this research, the tip-speed ratio (TSR) and solidity were used to describe aspects of speed and geometry, respectively. The CFD simulations were run at twenty-three TSRs ranging from 1.5 to 7.0 and five solidities ranging from 0.15 to 1.0 based on the turbine diameter and airfoil shape of the Uppsala University 12 kW H-rotor VAWT (Fig. 1.2) [3]. Four simulations were also run at

each TSR/solidity configuration with different Reynolds numbers in the range of 5 to 6 million by varying the wind speed, resulting in a total of 460 simulations (illustrated by Fig. 3.4).

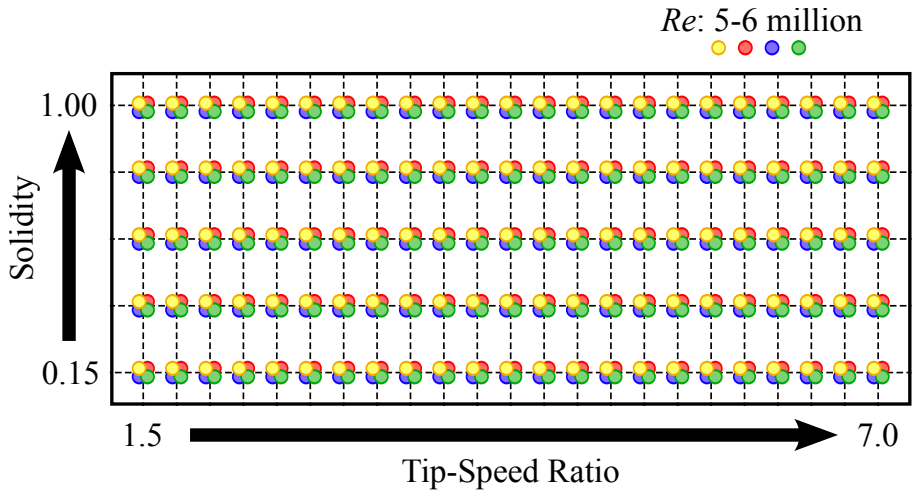

Figure 3.4: An diagram of the CFD simulations at 23 tip-speed ratios between 1.5 and 7.0, five solidities between 0.15 and 1.0, and four Reynolds numbers between 5 and 6 million.

Once all of the simulations were completed, the wake data could then be analyzed and trend fitted. An example of the time-averaged normalized x-velocity distribution is shown in Fig. 3.5 at a TSR of 4.5 and a solidity of 0.25. As can be seen, the velocity distribution was fairly complex with slightly slower moving wind velocities in front of the turbine, faster wind velocities on the sides of the wake region, and the wake decaying at about 10 diameters downstream. The possibility of creating a wake model based on the velocity data was explored as the benefits of this method include the rapid computation time of direct velocity calculations and its ability to easily add data sets for increased accuracy. However, one of the difficulties in fitting the velocity data with a mathematical model was its complex shape consisting of induced velocities in both the x- and y-directions all around the turbine. The slight wind velocity increase on the edges of the main deficit region also presented difficulties in modeling. Implementing combinations of Gaussian, quadratic, exponential, power, and piecewise distributions to fit the complex data resulted in a very complex equation with an extensive data implementation that failed to capture the complete velocity distribution, as shown in Fig. 3.6.

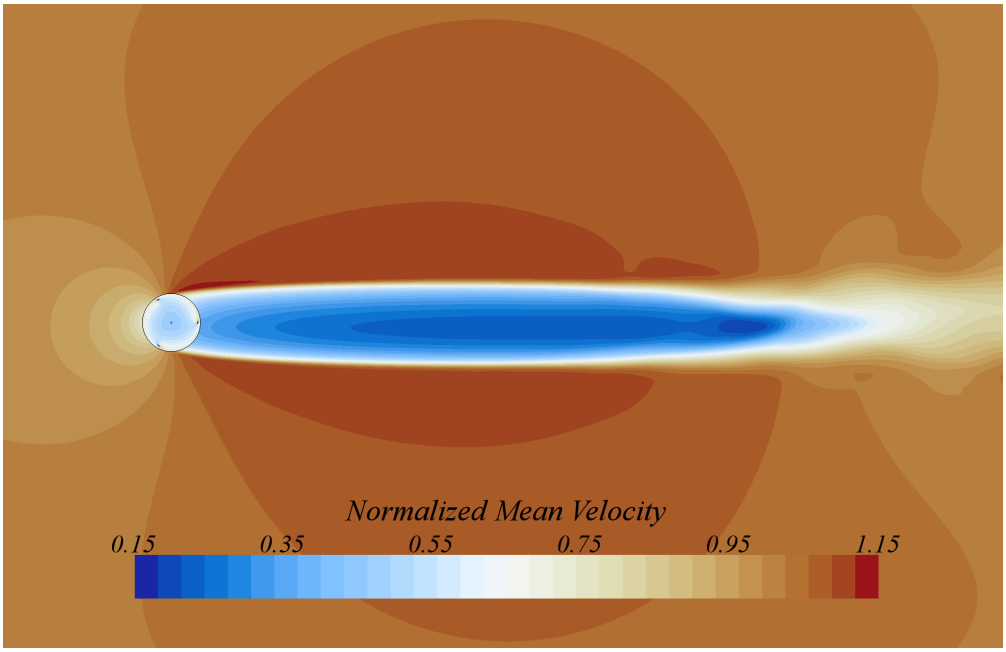

Figure 3.5: An example of the time-averaged x-velocity field from the CFD model at a TSR of 4.5 and a solidity of 0.25. The velocity is normalized by the free stream wind velocity of 8.87 m/s.

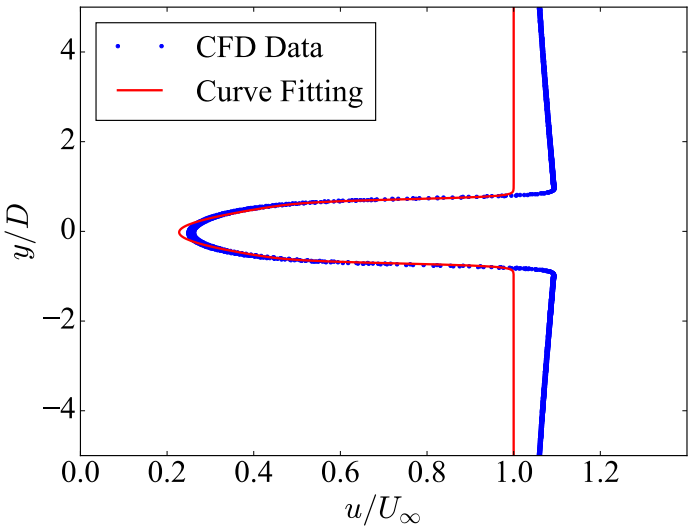

Figure 3.6: An example of the x-velocity (u) normalized by the free stream wind velocity (U_∞) calculated by the CFD simulation at 16.667 diameters downstream of the turbine with a TSR of 4.0 and a solidity of 0.25. The lateral position (y) is normalized by the turbine diameter (D). An attempted curve fitting of the velocity distribution is overlaid.

An alternative method that proved to be successful for wake modeling was capturing the vorticity data. A time-averaged normalized vorticity distribution at a TSR of 4.5 and a solidity of 0.25 can be seen in Fig. 3.7. This distribution consists of concentrated streams of vorticity on both sides of the wake region behind the turbine until decaying at about 10 diameters downstream, similar to the velocity distribution. Using the relationship presented in Eq. (2.3), the vorticity data, only located behind the turbine, could be integrated and produce induced velocities in the x- and y-directions in front, to the sides, and behind the turbine. The ability to calculate induced velocities is important for the possibility of placing VAWTs close together for increased power production as shown in other research efforts [10, 11, 19]. In using Eq. (2.3), it was discovered that a wake model based on fitting of the complete vorticity profile produced the most accurate estimates of velocity.

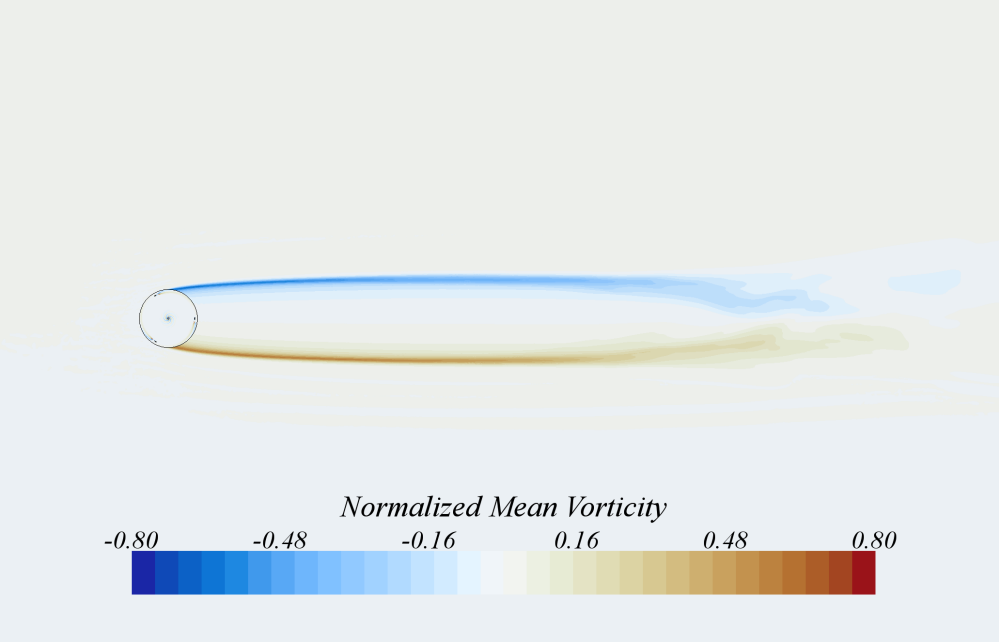

Figure 3.7: An example of the time-averaged vorticity field from the CFD model at a TSR of 4.5 and a solidity of 0.25. The vorticity is normalized by the rotation rate of 13.3 rad/s.

To extract the numerical data from the CFD simulations, thirty lateral cuts were made in the wake region to a point downstream where the wake had effectively decayed, which ranged from 2 to 35 diameters downstream based on TSR and solidity (illustrated in Fig. 3.8). The vorticity data cuts produced distributions with skewed peaks on each side of the wake and long tails towards the center, as seen in Fig. 3.9. After exploring several probability distributions to capture the trends

in vorticity data, such as the skewed normal, Gompertz, and Weibull distributions, the best fit with the lowest error was attained using the probability density function of an exponentially modified Gaussian (EMG) distribution, defined in Eq. (3.2) with respect to an arbitrary variable (q). The EMG distribution demonstrates the same shape as the vorticity data with a skewed peak and a long tail towards the center. Four parameters are used to create the EMG distribution that describe the approximate location (μ) and height, or scale (ζ), of the peak and the spread (ψ) and skew (κ) of the curve, all illustrated in Fig. 3.10. These parameters correspond to elements of turbulent wake statistical moments from other studies (mean, standard deviation, etc.), demonstrating a reasonable implementation of the EMG distribution in modeling the wake [54–56]. Two EMG distributions were used, one reflected over both the x- and y-axes, to fit the vorticity strength (γ) normalized by the rotation rate (Ω), shown in Fig. 3.11.

$$EMG(q;\ \mu,\psi,\kappa,\zeta) = \zeta\left[\frac{\kappa}{2}\exp\left(\frac{\kappa}{2}\left(2\mu+\kappa\psi^2-2q\right)\right)\ \operatorname{erfc}\left(\frac{\mu+\kappa\psi^2-q}{\sqrt{2}\psi}\right)\right] \tag{3.2}$$

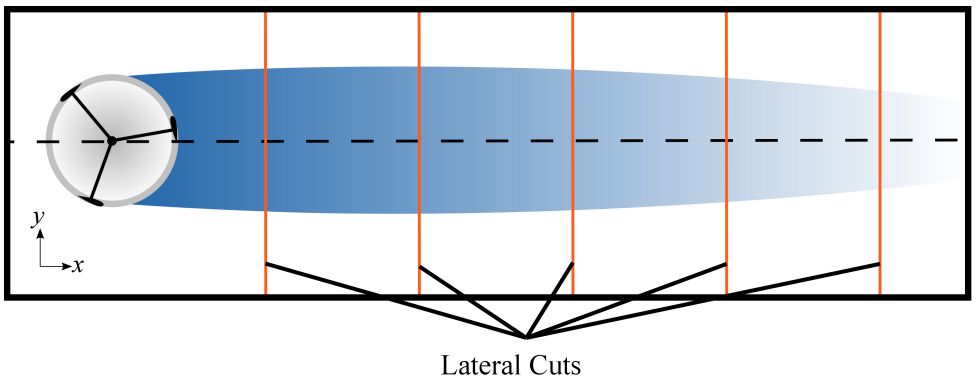

Figure 3.8: A simple representation of the five lateral cuts (shown in orange) made to analyze the wake data numerically. Thirty cuts were made of the CFD wake data until a point where the wake had effectively returned to free stream wind velocity. The downstream (x) and lateral (y) positions were normalized by the turbine diameter (D).

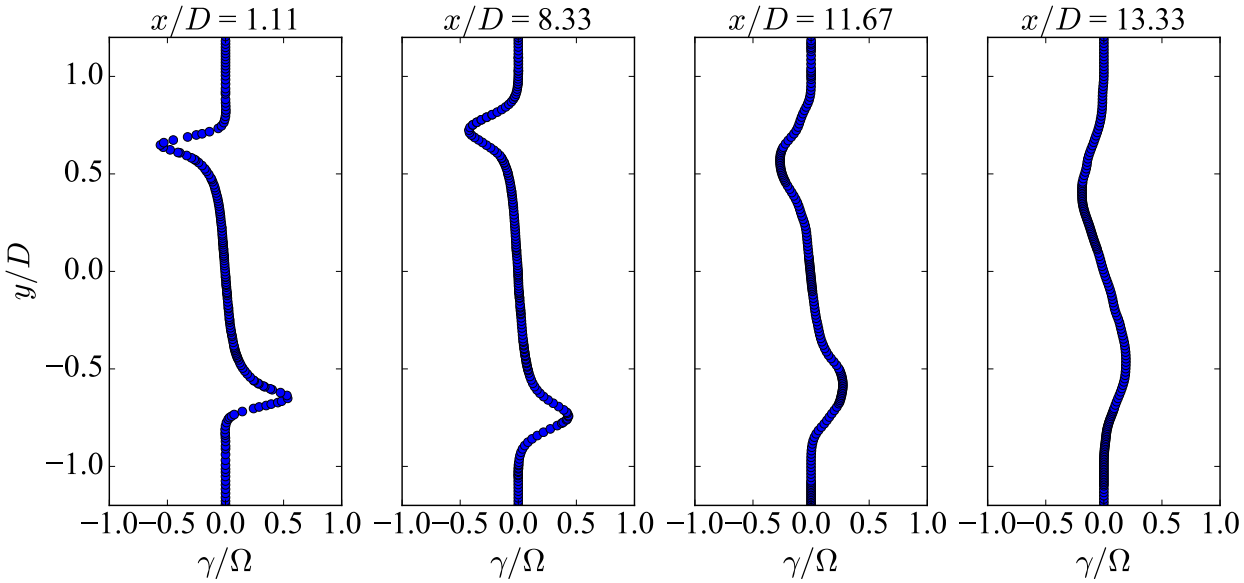

Figure 3.9: An example of the vorticity data obtained from four lateral cuts at a TSR of 4.0 and a solidity of 0.25. The vorticity strength (γ) is normalized by the rotation rate (Ω) and the lateral position (y) is normalized by the turbine diameter (D).

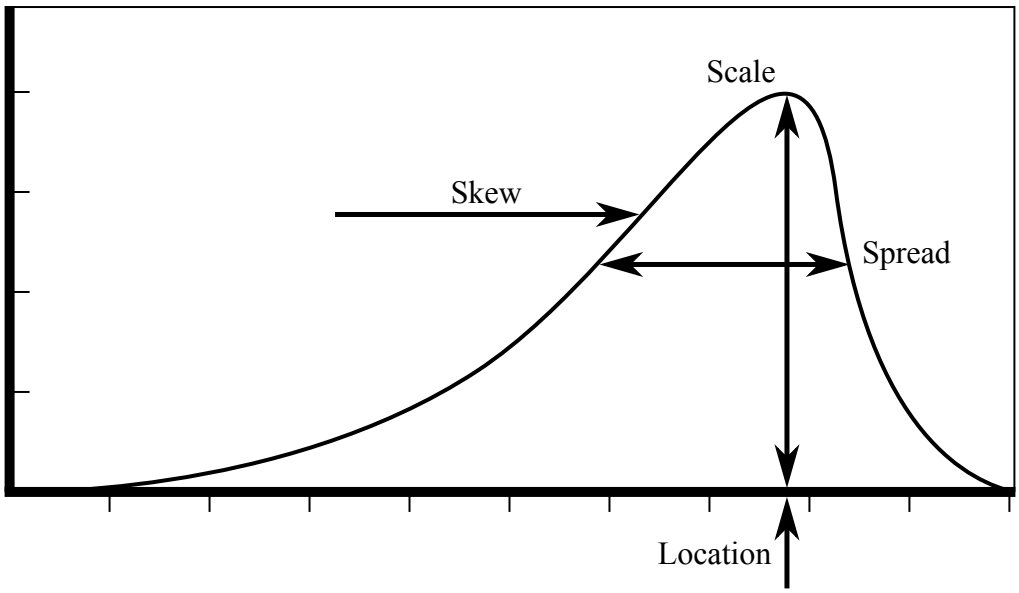

Figure 3.10: An example of the exponentially modified Gaussian distribution showing the four parameters of location (μ), spread (ψ), skew (κ), and scale (ζ) and how they approximately affect the shape of the distribution.

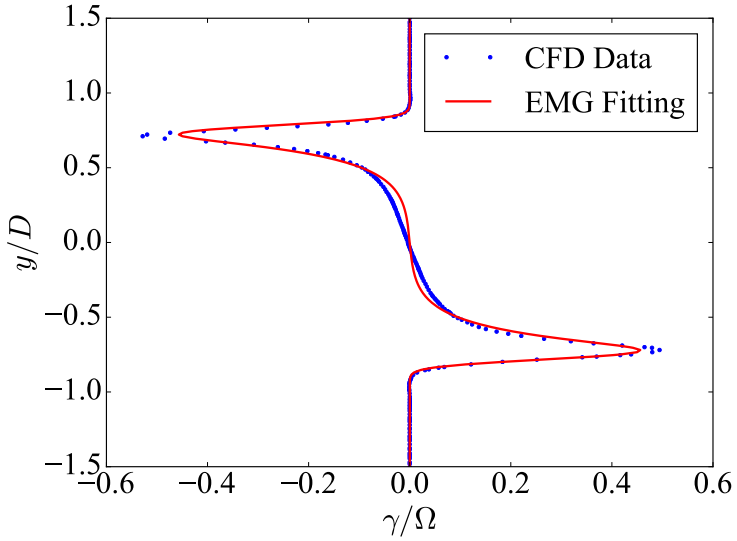

Figure 3.11: An example of the vorticity strength (γ) normalized by the rotation rate (Ω) calculated by the CFD at the same location and configuration as Fig. 3.6. The lateral position (y) is normalized by the turbine diameter (D). The EMG fitting of the data is overlaid.

3.3 Wake Model Development

The purpose of a reduced-order wake model is to accurately and quickly calculate wake velocity deficits of a turbine. In large-scale wind farm analysis and optimization, these benefits are required to produce velocity calculations at every turbine within a matter of minutes. While the CFD data obtained was very accurate in modeling the VAWT wake, it was time consuming to run each simulation of a single VAWT and would take significantly longer for larger numbers of turbines. Therefore, the improved performance of reduced-order wake models is necessary when analyzing the velocity throughout a wind farm with many turbines.

To produce the wake model, trends in the vorticity data needed to be parameterized in the downstream and lateral directions as well as across the TSRs and solidities of the CFD simulations, as these parameters could vary as the turbines are repositioned in a wind farm. The EMG distribution, multiplied by the rotation rate (Ω), was fitted to the vorticity strength on both the left ($_L$) and right ($_R$) side of the wake in the normalized lateral direction (y/D) using the equation:

$$\gamma(y/D) = \Omega\,[\,EMG(y/D;\ \mu_L, \psi_L, \kappa_L, \zeta_L) - EMG(y/D;\ \mu_R, \psi_R, \kappa_R, \zeta_R)\,] \tag{3.3}$$

As the wake's size and strength varied moving downstream of the turbine, each of the four EMG variables needed to vary as a function of normalized downstream direction. In order to determine what combination of equations should be used to model the variation of the EMG variables moving downstream as well as the coefficients used in the equations at each TSR and solidity, hold-out cross-validation was implemented with 70% of all the CFD vorticity data used as the training set and the remaining 30% as the validation set. This process was done three times and the averages of the results were computed to reduce any bias that may exist in the training or validation sets. Cross-validation was important in forming the wake model in order to eliminate any outliers in the CFD data that may influence the wake model to reflect behavior specific to that turbine configuration. These outliers could come from CFD simulations that had not fully converged or that demonstrated wake behavior not consistent with the rest of the data set.

In performing the cross-validation, combinations of quadratic and linear distributions were explored for the μ, ψ, and κ variables. Because ζ represented the total vorticity strength at a downstream position (which should remain nearly constant before decaying rapidly), a sigmoid distribution was selected for its ability to model a constant value before a rapid decay to zero. As each of the coefficients used in these equations also varied as a function of TSR and solidity, polynomial surfaces were used to model the variations at each TSR/solidity configuration. A rectangular bivariate spline fitting was initially used to fill in the TSR/solidity configurations not calculated by the CFD. This allowed for highly accurate fits at the calculated CFD configurations, but created an overfitting that occasionally resulted in poor predictive ability at conditions where CFD was not run. The use of polynomial surfaces, instead of spline fits, allowed for a more robust predictive ability across all the TSR/solidity combinations.

Implementing the cross-validation with a least-squares regression fitting between the entire CFD vorticity data set and the wake model, over 1,000 combinations of the equations and polynomial surfaces were explored. Cross-validation was performed with each combination three times, using different random training and validation sets, and the sum of the squared errors between the fit and the data was averaged. The best result was identified as the lowest squared error with the lowest order fit of all the equations to keep the model as simple as possible. As there were a few results with similar squared errors, the lowest order fit between them was selected, resulting in the use of a quadratic distribution for the location parameter (μ), linear distributions for the spread (ψ)

and skew (κ) parameters, and a sigmoid distribution for the scale parameter (ζ), all as a function of normalized downstream position. The high symmetry in the data allowed for the number of required variables to be reduced by half in describing both of the vorticity streams. These fits can be visualized in Fig. 3.12 for a TSR of 4.0 and a solidity of 0.25, each showing the symmetry between the two streams of vorticity data. As the scale parameter rapidly decreases to zero after its initial decay, the need to capture the turbulent data shown in the figure (at about 12 diameters downstream) is not necessary to accurately model the wake.

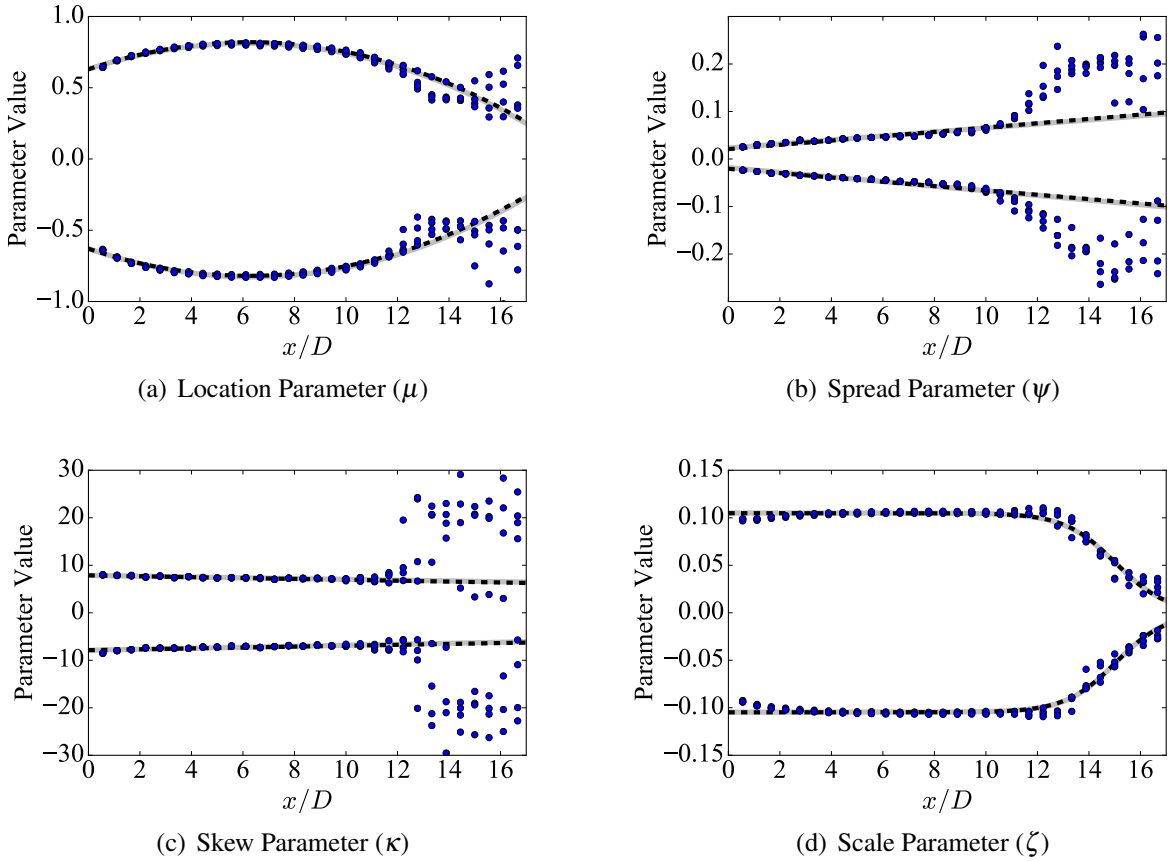

(a) Location Parameter (μ)

(b) Spread Parameter (ψ)

(c) Skew Parameter (κ)

(d) Scale Parameter (ζ)

Figure 3.12: An example of the different distributions used to capture the EMG parameters with respect to the downstream position at a TSR of 4.0 and a solidity of 0.25. The blue dots represent the values from independent CFD data trend fitting of each side of the vorticity for four different Reynolds numbers. The solid grey lines represent quadratic, linear, and sigmoid curve fits of each data set and the dashed black lines represent an average of the two sides (showing high symmetry in the data). The downstream position (x) is normalized by the turbine diameter (D). The spreading of data points near the far downstream end is caused by increasing turbulence.

Each of the four distributions used for the EMG parameters are produced using Eq. (3.4) with respect to the normalized downstream position (x/D). To account for the trends across TSR and solidity configurations, polynomial surfaces were formed using combinations of 2nd- and 3rd-order fits with respect to TSR and solidity to calculate each of the ten coefficients needed for the four EMG variables (represented with subscript numbers in Eq. (3.4)). The model was retrained using all of the CFD vorticity data, and an example of the final polynomial surface for ζ_3 can be seen in Fig. 3.13. For the case of ζ_3, smaller TSRs produce higher coefficient values and the values also decrease with higher solidities overall. Part of using the polynomial surfaces also involved limiting the coefficient values to appropriate ranges to both produce expected trends of the wake and provide numbers that the EMG distribution can handle. For example, ζ_3 was limited to positive values to ensure the wake decays downstream of the turbine. The complete set of polynomial surface curves and coefficient values are described in more detail in Appendix B.

$$\begin{aligned}
\mu(x/D) &= \mu_1 (x/D)^2 + \mu_2 (x/D) + \mu_3 \\
\psi(x/D) &= \psi_1 (x/D) + \psi_2 (x/D) \\
\kappa(x/D) &= \kappa_1 (x/D) + \kappa_2 (x/D) \\
\zeta(x/D) &= \frac{\zeta_1}{1 + \exp\left[\zeta_2 \left((x/D) - \zeta_3\right)\right]}
\end{aligned} \tag{3.4}$$

The x- and y-components of the induced wake velocity for any given downstream (x_o) or lateral (y_o) position in the fluid domain were then calculated by integrating the vorticity strength (a function of normalized downstream and lateral position, TSR (λ), and solidity (σ)) in the downstream (x) and lateral (y) directions using the equations:

$$\begin{aligned}
u(x_o, y_o) &= \int_a^b \int_{-w}^{w} \frac{\gamma(x/D, y/D, \lambda, \sigma)}{2\pi} \left[\frac{y - y_o}{(x - x_o)^2 + (y - y_o)^2} \right] dy\, dx \\
v(x_o, y_o) &= \int_a^b \int_{-w}^{w} \frac{\gamma(x/D, y/D, \lambda, \sigma)}{2\pi} \left[\frac{x_o - x}{(x - x_o)^2 + (y - y_o)^2} \right] dy\, dx
\end{aligned} \tag{3.5}$$

Each equation was integrated in the downstream direction from the position of the turbine (a) to a point where the wake had effectively decayed (b), which varied significantly across TSR/solidity configurations between 2 and 35 diameters. The equations were also integrated in the lateral direction a specified distance from the turbine (w). Rather than integrating over a large area around

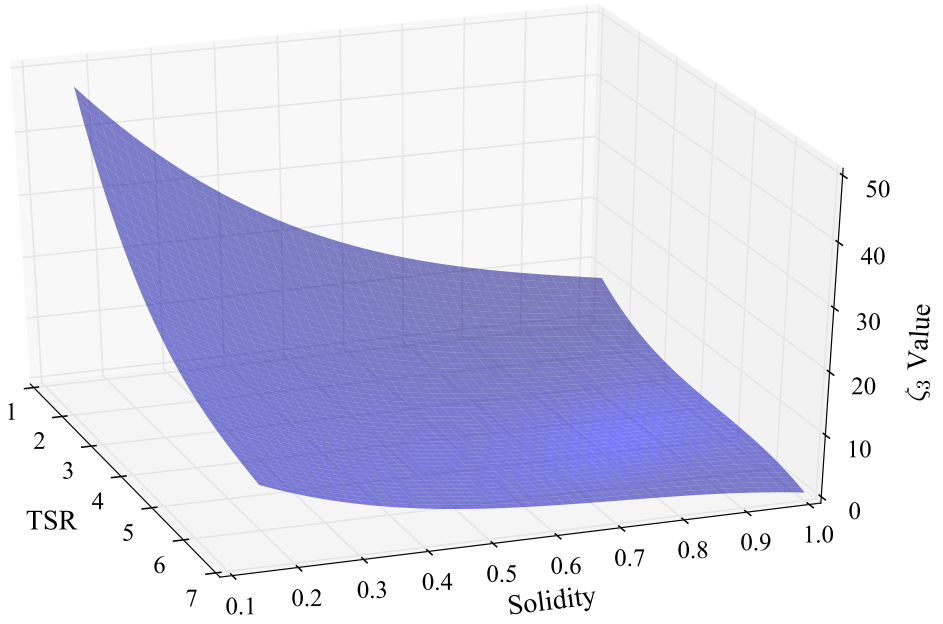

Figure 3.13: An example of a polynomial surface fit used to calculate ζ_3 as a function of TSR and solidity. The surface is limited in this case to only positive values to ensure the wake decays downstream of the turbine.

the turbine and its wake, the equations are only integrated in the downstream direction (b) five diameters after the vorticity strength sharply decreases (ζ_3) and in the lateral direction (w) only one diameter from the turbine. This was done to reduce the amount of unnecessary computations for areas with insignificant vorticity strength. Compared to integrating across the entire domain, integrating using the smaller region reduced the computational time by half, with only a 0.2% average percent difference for the case with a TSR of 4.0 and a solidity of 0.25. Since the integration of the model is done numerically due to the complex nature of the equations, the ability is included in the model to use either a slower, more accurate integration technique (based on a 21-point Gauss-Kronrod quadrature rule from SciPy) or a faster, less accurate integration technique (based on the Simpson's rule for integration with variable domain division). Each method could be used when either speed or accuracy is desired by the end user. The following section describes the results of the wake model's accuracy and speed in greater detail.

3.4 Results

While using a reduced-order model increases the speed of wind farm analysis and optimization, one must verify the accuracy of the model in predicting the velocity deficits of the turbine wakes. This verification was first done by comparing the CFD wake velocity data (Fig. 3.14) with the wake velocities calculated by the developed reduced-order VAWT wake model (Figs. 3.15 and 3.16). The wake model was able to capture the general trends of slower moving wind in front of the turbine, slight wind speed increases on the sides of the wake region, and a decay far enough downstream of the turbine, all with correct velocity magnitudes in the correct regions. While the CFD demonstrates near symmetry with slight asymmetric regions around the wake, the wake model predicts velocities with complete symmetry due to the simplification of reducing the required EMG parameters by half.

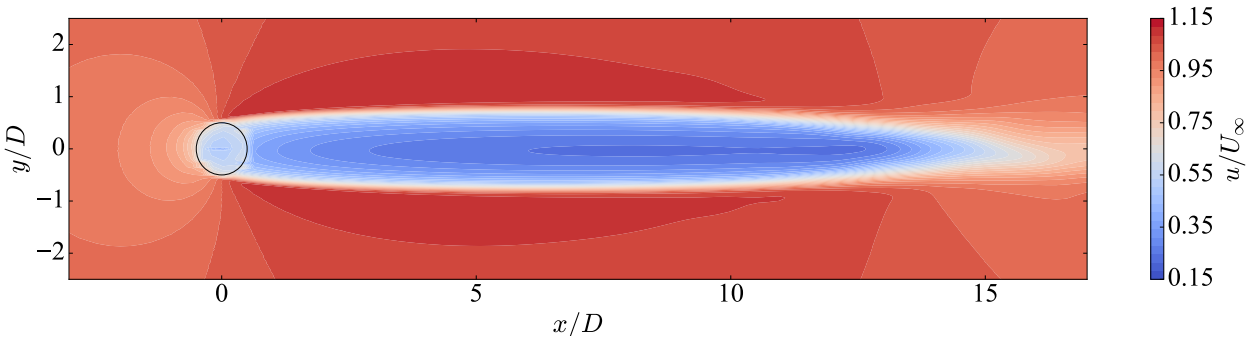

Figure 3.14: The x-velocity profile over the fluid domain calculated by the CFD simulation. The downstream (x) and lateral (y) positions are normalized by the turbine diameter (D) and the velocity (u) by the free stream wind velocity (U_∞).

The Simpson's rule integration created a coarse wake structure with a smaller number of subdivisions compared to the Gauss-Kronrod method. The coarseness is an acceptable compromise for its speed as a 220x200 grid subdivision in the integration (shown in Fig. 3.16) can calculate the velocity at a given point in about 0.02 seconds with an average percent difference of about 1.1% of the Gauss-Kronrod method, which on average calculates velocity at any point in about 0.3 seconds. Only about 12% of the points were above a percent difference of 10% where the coarseness along the wake, seen in Fig. 3.16, differs from the smoothness of the Gauss-Kronrod method in Fig. 3.15. This can be visualized in the error plot of Fig. 3.17 showing the percent

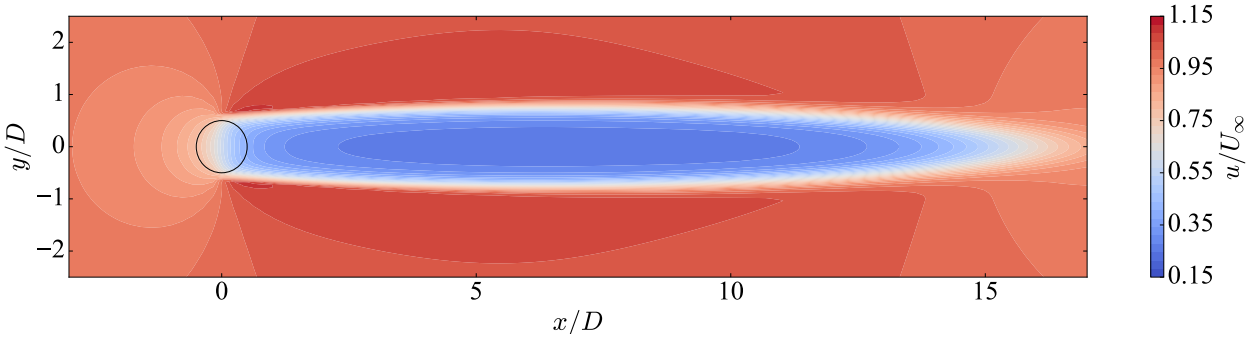

Figure 3.15: The x-velocity profile over the fluid domain calculated by the reduced-order wake model using a 21-point Gauss-Kronrod quadrature rule. The downstream (x) and lateral (y) positions are normalized by the turbine diameter (D) and the velocity (u) by the free stream wind velocity (U_∞).

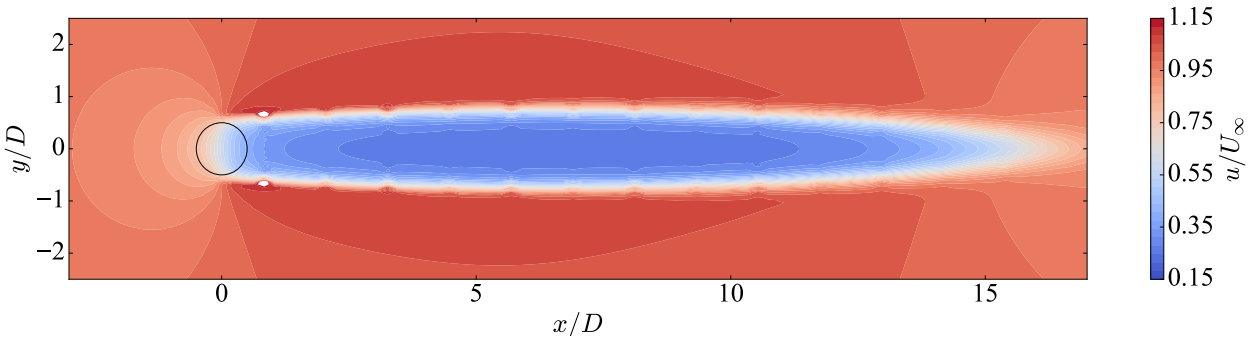

Figure 3.16: The x-velocity profile over the fluid domain calculated by the reduced-order wake model using the Simpson's rule with the downstream domain divided into 220 segments and the lateral domain divided into 200 segments. The downstream (x) and lateral (y) positions are normalized by the turbine diameter (D) and the velocity (u) by the free stream wind velocity (U_∞).

difference error of the Simpson's method with the Gauss-Kronrod method with the highest errors along the sides of the wake in the coarse regions. As the Simpson's method would produce less accurate results but would most likely be used for wind farm layout analysis and optimization, the following validation studies are all based on integration using the Simpson's method understanding that the Gauss-Kronrod method would produce more accurate results with a longer computation time.

Numerical validation was carried out by first comparing the wake model with the CFD model using velocity profiles at various downstream distances. Fig. 3.18 shows an example of this comparison using six downstream distances at a TSR of 4.0 and a solidity of 0.25. Overall, the

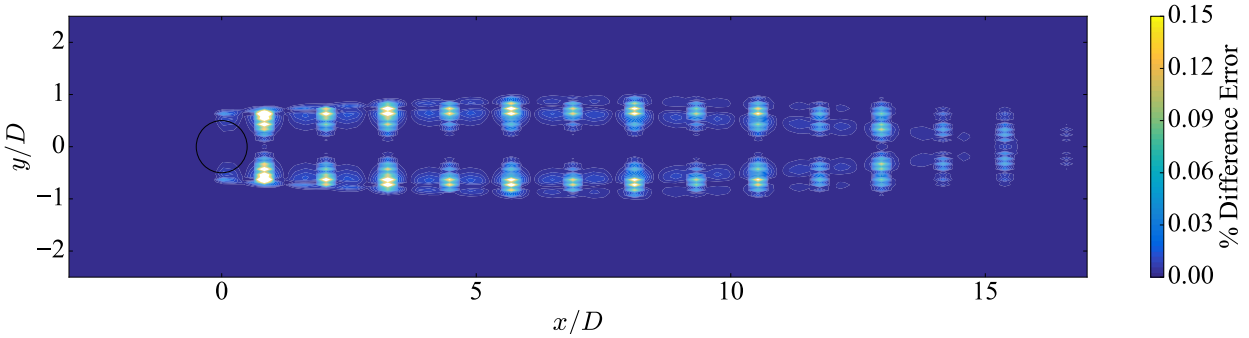

Figure 3.17: The average percent difference in velocity calculations between the Gauss-Kronrod method and the Simpson's method based on the velocity calculations shown in Figs 3.15 and 3.16. The error overall remains near zero with the exception of the regions on the side of the wake where the error exceeds 10% difference in coarser areas of the Simpson's method calculation. The downstream (x) and lateral (y) positions are normalized by the turbine diameter (D).

wake model follows the general trend of the CFD data by capturing the velocity deficit region of the wake directly behind the VAWT, but slight differences between the two can be observed. One difference between the CFD data and the wake model is the slight flattening of the model between $y/D = \pm 0.5$ rather than the the CFD's rounded profile. This behavior was exhibited due to the fact that between $y/D = \pm 0.5$, the EMG curve decreased to a normalized vorticity strength of 0.0 slightly faster than the CFD data (see Fig. 3.11). In this region, less vorticity than is actually present is predicted causing the slight flattening in the velocity profile. Cross-validation also contributed to the behavior as the model was fit across all CFD configurations rather than just at this one. This means that a slightly higher error at a given TSR/solidity configuration could have a better fit overall across all of the TSRs and solidities modeled. The wake model also decays about 2.5 times faster than the CFD at this configuration, as seen at $x/D = 20.0$ (Fig. 3.18(f)). This behavior is due to the sigmoid distribution fit of Eq. (3.4) decreasing faster than the CFD data when the wake begins to decay far enough downstream of the turbine.

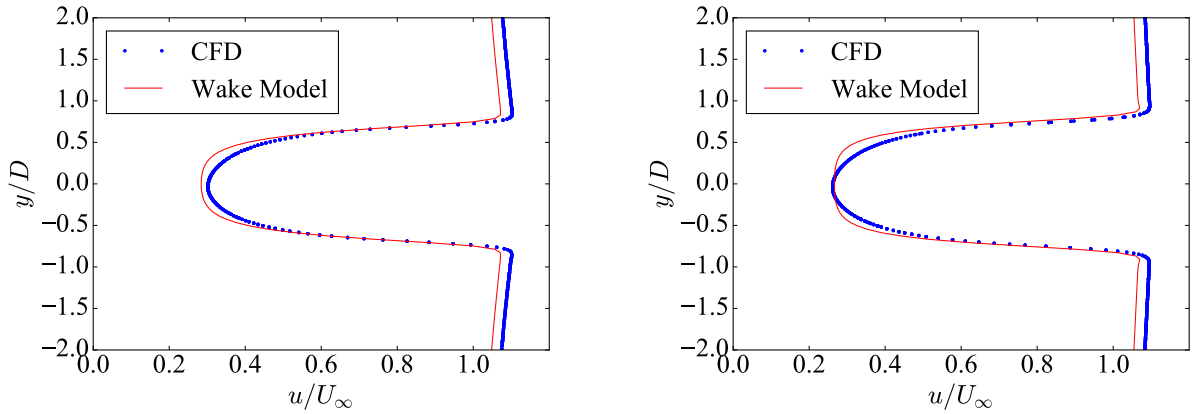

(a) $x/D = 2.0$; RMS = 0.0298

(b) $x/D = 4.0$; RMS = 0.0362

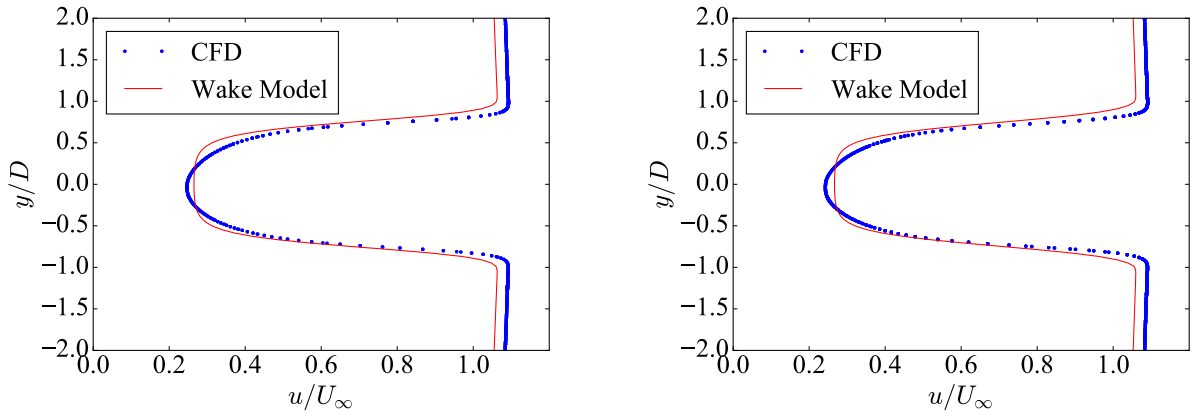

(c) $x/D = 8.0$; RMS = 0.0428

(d) $x/D = 10.0$; RMS = 0.0406

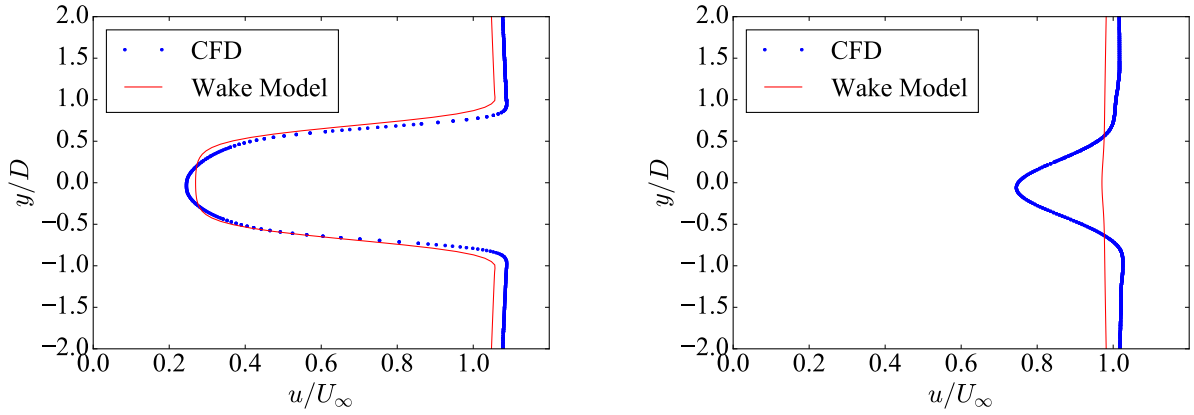

(e) $x/D = 15.0$; RMS = 0.0299

(f) $x/D = 20.0$; RMS = 0.0652

Figure 3.18: Examples of normalized x-velocity profiles of the CFD data and the wake model at a TSR of 4.0 and a solidity of 0.25. The root mean squared (RMS) errors of velocity deficit normalized by the free stream wind velocity (U_∞) between the CFD and wake model are shown. The downstream (x) and lateral (y) positions are normalized by the turbine diameter (D).

To calculate the accuracy of the wake model over all of the CFD data obtained, a comprehensive comparison of all TSR and solidity configurations was conducted making measurements at 2, 4, 8, 10, 15, and 20 diameters downstream of the turbine. An RMS error normalized by the free stream wind velocity was calculated between the wake model and the CFD data, and the errors at each downstream distance were then averaged together at each TSR/solidity configuration, shown in Fig. 3.19. As seen in the error plot, the wake model compared well with the CFD overall with an average normalized RMS error of 0.059 for all the TSR/solidity configurations. The error was higher at a TSR of 3.5 and a solidity of 2.5 where the shape of the wake model velocity distribution differed with the specific CFD model, demonstrating the power of cross-validations in protecting against outlying trends in the data. The worst error reached near 0.15 at a TSR of 7.0 and a solidity of 1.0 due to the wake model returning to the free stream wind velocity faster than the CFD data, similar to the case presented previously. Overall, this comparison demonstrates good accuracy of the wake model with the CFD data points while maintaining its robustness due to the cross-validated polynomial surfaces used to calculate the EMG parameters.

The reduced-order wake model was also compared to the experimental PIV study conducted by Tescione et al. described at the beginning of the chapter [7]. The velocity profiles of the PIV, the CFD validation study, and the reduced-order wake model were overlaid and can be seen in Fig. 3.20. As expected from a CFD-based reduced-order wake model, the wake model follows the near symmetric trend of the CFD data rather than the asymmetry of the experimental data. Overall, the wake model matched the PIV data with an RMS error normalized by the free stream wind velocity of 0.119, slightly higher than the normalized RMS error of 0.113 for the CFD. The percent difference of the maximum velocity deficit of the wake model was 6.3%, also slightly higher than the 5.8% of the CFD. As the wake model was created based only on the CFD data using the specifications of Kjellin et al. [3], the comparison with the PIV data demonstrates the applicability of the wake model to different geometric configurations.

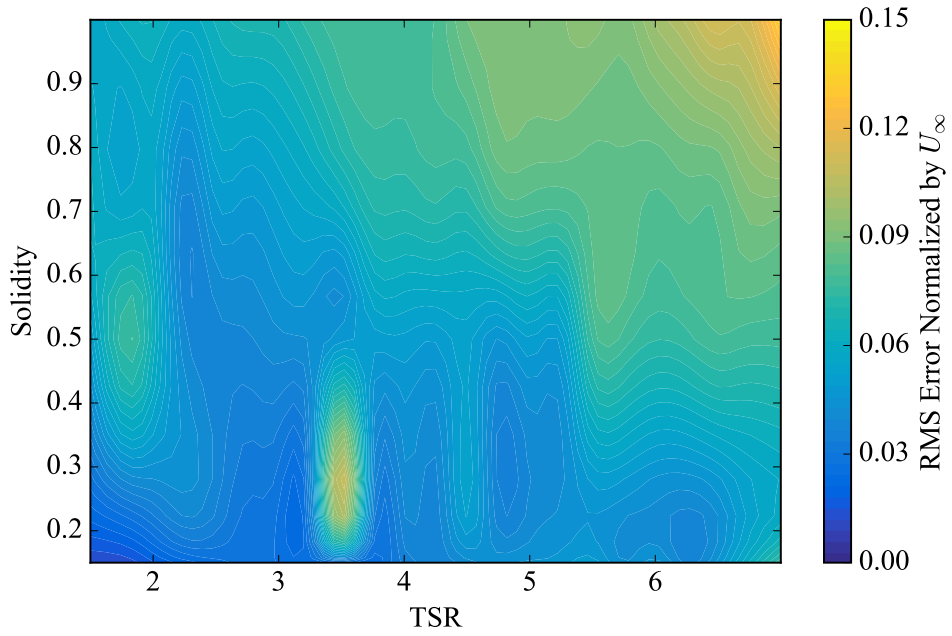

Figure 3.19: The average normalized RMS error of the velocity deficits predicted by the reduced-order wake model compared to the CFD data. The values shown are averages of the normalized RMS errors at 2, 4, 6, 8, 10, 15, and 20 diameters downstream.

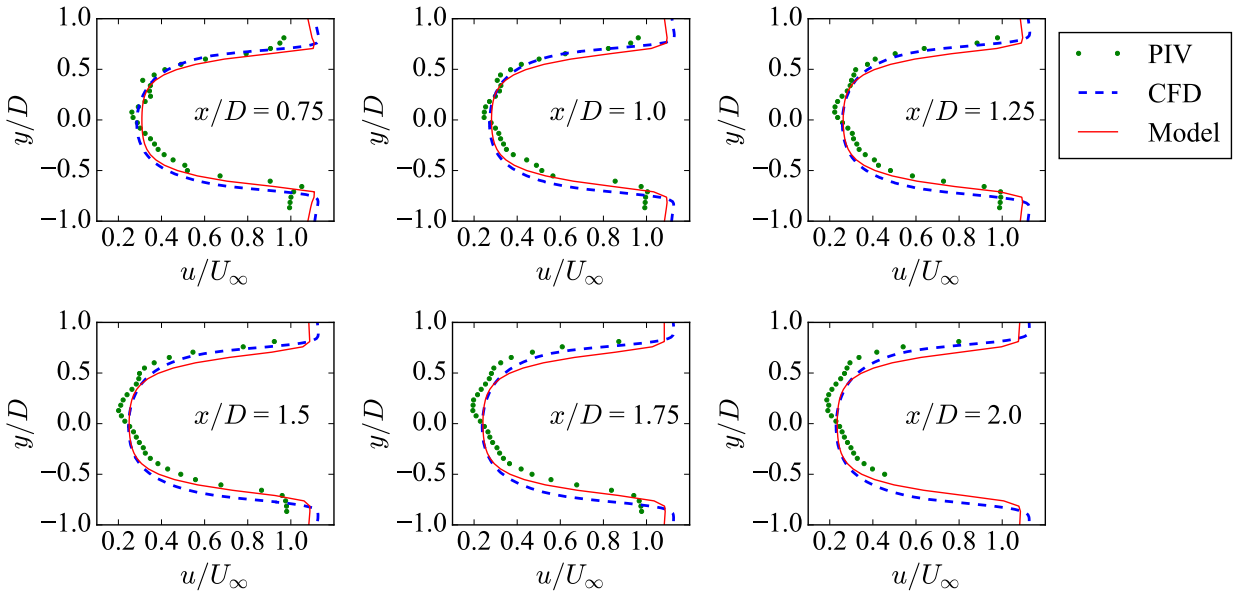

Figure 3.20: The wake velocity comparison seen in Fig. 3.2 with the reduced-order wake model added. The velocity (u) is normalized by the free stream wind velocity (U_∞) and the downstream (x) and lateral (y) positions are normalized by the turbine diameter (D).

For further validation, the wake model was also compared to a wind tunnel study conducted by Battisti et al. [8] In this study, a three-bladed VAWT with a 1.03-meter diameter was placed in a wind tunnel with a wind speed of about 16 m/s resulting in a Reynolds number of about 1,000,000. The wind tunnel had a removable test room in which the VAWT could be placed and tests were run in both a closed configuration (the test room enclosed over the VAWT) and an open configuration (the test room removed and the VAWT open to the outside air). As VAWTs are generally operated in the open, the open configuration was used to compare to the wake model. The wake velocity was recorded 1.5 diameters downstream of the turbine and the data was overlaid with the wake model's calculations as seen in Fig. 3.21.

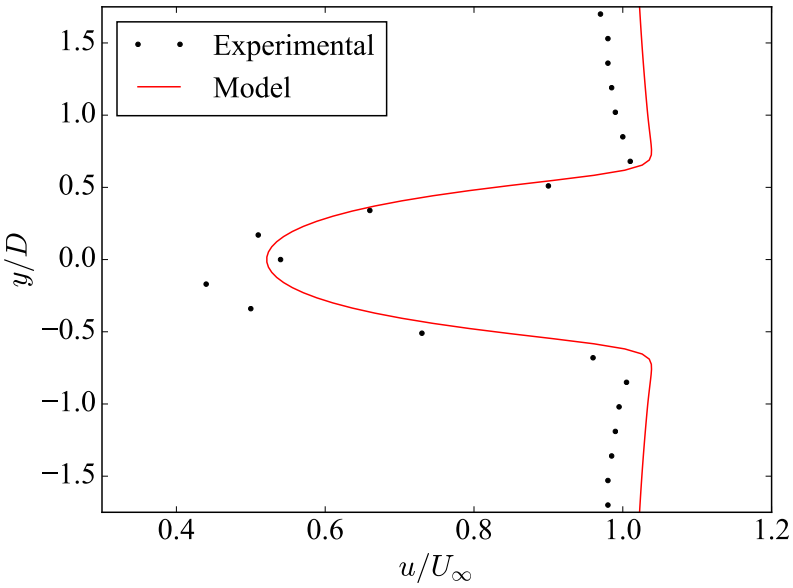

Figure 3.21: The wake velocity comparison between the study conducted by Battisti et al. [8] and the reduced-order model at 1.5 diameters downstream. The velocity (u) is normalized by the free stream wind velocity (U_∞) and the lateral (y) position is normalized by the turbine diameter (D).

The wake model matched the experimental results with a normalized RMS error of 0.061. The percent difference of the maximum velocity deficit was 14.6%, but this value could be slightly high due to the noisiness of the data points at the maximum velocity deficit. These two validation studies demonstrate the reduced-order wake model's robustness in matching experimental data with RMS errors below 0.119 and percent differences of the maximum wake deficit below 14.6%

in the cases presented with different turbine geometries and setups than the original CFD models used for the basis of the wake model.

3.5 VAWT Power Adaptation

As described in Chapter 2, wind farm power production is based on the energy available in the wind and the turbines' capacity to convert the available energy into power, described by the power coefficient (C_P) (see Eq. (2.2)). The developed wake model has the ability to predict wake velocity within a wind farm at any given point, and therefore able to predict the available wind energy for the turbines. However, equations describing VAWT aerodynamics are necessary to calculate a turbine's power coefficient and the power production of a wind farm.

A method to calculate the aerodynamics of a VAWT has been developed by Madsen, referred to as the actuator cylinder (AC) model [9]. This model works by dividing the flight path of the turbine blades into distinct points. The velocities at each of these points is calculated in the lateral and downstream directions based on the influence every other point has on a given point. Using these wind velocities, forces are calculated on the turbine blades based on the lift and drag of the airfoil as well as the rotation direction (see Fig. 3.22). These forces produce a torque on the turbine that is then used to calculate the turbine's power in the equation:

$$P_{turbine} = \frac{\Omega B}{2\pi} \int_0^{2\pi} RT(\beta_r) d\beta_r \tag{3.6}$$

were Ω is the rotation rate of the turbine, B is the number of blades, R is the turbine radius, and $T(\beta_r)$ is the torque on the turbine as a function of rotational position, β_r. The equation is integrated over the full rotation of the turbine from 0 to 2π.

The code of the AC model used in this thesis was originally developed by Ning for use with multiple VAWTs [11]. However, only one VAWT was analyzed with the AC model to calculate the induced velocities within the turbine region due to blade interaction (u_b and v_b), and influences from other turbines were calculated with the developed wake model. The turbine's flight path is discretized into 36 points, a value used by both Ning and Madsen in the implementation of the AC model in their respective studies [11, 57], and the torque (T) is calculated using the normal and tangential components of the velocity (V_n and V_t) at each rotational position using the equations:

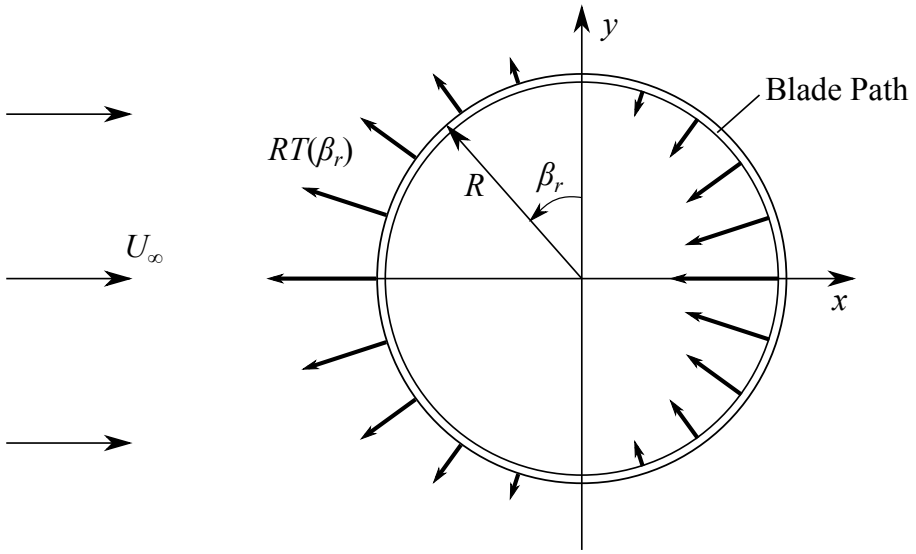

Figure 3.22: An illustration of the actuator cylinder method taken from the work of Madsen showing the division of the VAWT blade flight path into points and the calculation of the force ($RT(\beta_r)$) at each point in free stream wind velocity (U_∞) [9].

$$
\begin{aligned}
V_n &= [U_\infty(1+u_b)+u_w]\sin(\beta_r) - [U_\infty v_b + v_w]\cos(\beta_r) \\
V_t &= \pm\big\{[U_\infty(1+u_b)+u_w]\cos(\beta_r) + [U_\infty v_b + v_w]\sin(\beta_r)\big\} + |\Omega|R \\
T &= \frac{1}{2}C_T\rho(V_n^2+V_t^2)\frac{c}{\cos(\delta_b)}
\end{aligned}
\tag{3.7}
$$

where C_T is the tangential force coefficient for a given rotation position, ρ is the air density, c is the chord length, and δ_b is the blade curvature angle; the blade interaction velocities u_b and v_b are normalized by the free stream wind velocity (U_∞). The $\pm$ is positive for counter-clockwise rotation and negative for clockwise rotation as viewed from above. To account for turbine wake interaction, the induced velocities from the wake model (u_w and v_w) are added to the AC induced velocities at each of the 36 points as seen in Eq. (3.7). Multiple wakes from N turbines are combined using a sum-of-squares average:

$$
\begin{aligned}
u_{w,total} &= \sqrt{\sum_{i=1}^{N} u_{w,i}^2} \\
v_{w,total} &= \sqrt{\sum_{i=1}^{N} v_{w,i}^2}
\end{aligned}
\tag{3.8}
$$

There have been several studies that have indicated that closely spaced VAWT pairs could have an additive effect on the power production of both turbines [10, 11, 15, 19]. The works of Zanforlin and Nishino [10] and Ning [11] have both demonstrated this effect using CFD and the AC model, respectively. Using the AC model combined with the developed VAWT wake model in this thesis, this effect was also demonstrated, as shown in Fig. 3.23, where the sum of the powers from two counter-rotating turbines is normalized by the power of both in isolation. The results show a power increase of over 10% to the sides of the turbine with significant power decreases in the wake regions. The two studies also calculated the normalized power of a coupled pair of counter-rotating VAWTs as a function of wind direction. The wake model was used in the same procedure and plotted against the two other studies in Fig. 3.24. The model compared with 92.1% overall accuracy to the study by Ning with the wake model predicting a normalized power about 0.1 lower around 90° and 270°. The power comparisons were also conducted for co-rotating VAWT pairs and the results were nearly identical, the same conclusion found by Ning [11].

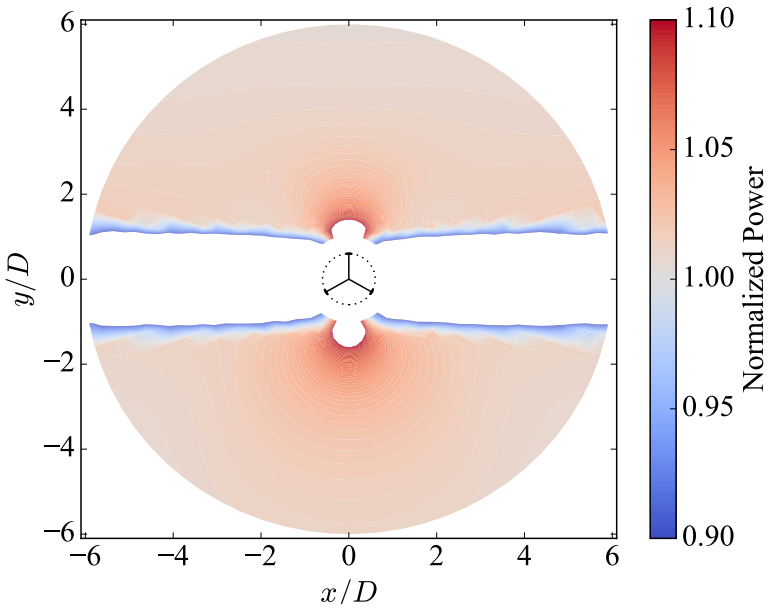

Figure 3.23: The total power distribution of two counter-rotating Mariah Windspire 1.2 kW VAWTs at a TSR of 2.625 normalized by the power of both in isolation. The turbine in the center is rotating counter-clockwise and the turbine moving around is rotating clockwise with the wind coming from the left. The color scale only shows values from 0.90 to 1.10 and centered on 1.0 to focus on the power increases and decreases of closely spaced turbines. The downstream (x) and lateral (y) positions are normalized by the turbine diameter (D).

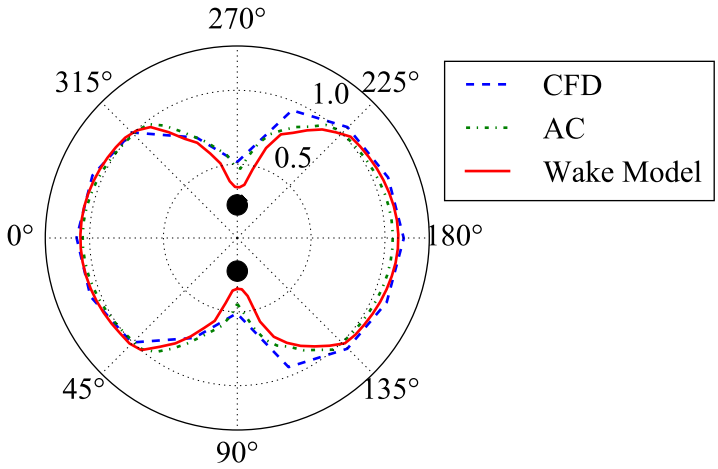

Figure 3.24: The normalized power of two counter-rotating Mariah Windspire 1.2 kW VAWTs at a TSR of 2.625 as a function of wind direction (the two black dots represent the orientation of the turbines with respect to the wind). Calculated values using the CFD model from Zanforlin and Nishino [10] and the AC model from Ning [11] are also shown.

3.6 Conclusion

As wind farm designs shift more to offshore and urban environments, VAWTs have the potential of providing energy more effectively than the traditional HAWT in these environments due to their simpler design and operation. However, the lack of a reduced-order VAWT wake model to calculate the wake velocity deficit quickly and accurately makes it difficult for VAWTs to be used in wind farm layout analysis and optimization. The wake model presented in this research has the potential to solve this problem by combining a large CFD vorticity database with the speed of computational algorithms to calculate the wake velocity of a VAWT relatively quickly and with reasonable accuracy. The model's ability to be parameterized by TSR and solidity also allow it to be used with a wide range of turbines that fall within a TSR of 1.5 and 7.0 and a solidity of 0.15 and 1.0. While this study focused mainly on the speed and geometry of the turbine and did not fully consider atmospheric conditions of the wind density and viscosity, good agreement was found with the wake model and the validation studies with Reynolds numbers between about 600,000 and 6,000,000.

In comparing the velocity results of the wake model to other methods of velocity calculation, reasonable agreement was found. Across all the CFD data, a normalized RMS error of

0.059 was calculated, with a few configurations reaching as high as 0.230 at specific downstream locations, for a significant reduction in computational time. Comparing the wake model with PIV and wind tunnel experiments, the model matched the experiments with a normalized RMS error of 0.119 in one and 0.061 in the other. These comparisons between the wake velocity measurements give validity to the wake model in its ability to predict the wake velocity with reasonable accuracy and robustness, especially with the experimental studies not affecting the wake model's development. Using the developed VAWT wake model and combining it with the AC model, a power calculation can be made of a turbine based on the aerodynamic loading of the VAWT blade.

There are many other potential additions for the wake model including further study of the effect of airfoil shapes and atmospheric conditions. As significant differences did not exist between variations of these factors in this research, it was assumed that specifying airfoil shape and atmospheric conditions was not necessary to produce a robust and parameterizable VAWT wake model, particularly for this initial model based on large amounts of CFD wake data. Future study, however, may indicate that these factors are important to consider for better accuracy of the model. Another factor that could affect the wake model is the three-dimensional effect of finite blades on the wakes produced. In this initial study, a three-dimensional wake was not modeled to provide a way to systematically obtain large amounts of wake data, but any wind farm layout study of variable-height VAWTs would certainly need to consider this effect. The wake model is also not meant to be a static, final wake model based only on the CFD vorticity data. Rather, it is intended to be extendable for adding more velocity data (both experimental and simulated) and retraining the polynomial surface parameters for more accurate velocity calculations.

CHAPTER 4. WIND FARM OPTIMIZATION USING NOISE CONSTRAINTS

The development of the reduced-order wake model described in Chapter 3 is necessary for VAWTs to be used in wind farm layout optimization to maximize power production. However, if VAWTs are used in urban areas, turbine noise must also be considered to reduce its disturbance to individuals near the wind farm. As noise restrictions impact the power production of the wind farm, it is necessary to understand the trade-offs of maximum power production and noise limitations of a wind farm. To demonstrate the impact of noise restrictions on the power production of a traditional HAWT wind farm, this chapter describes two wind farm layout optimizations using a HAWT wake model and various levels of noise constraints calculated by the BPM equations. Comparing the optimization results of the two wind farms, the impact on average power production from varying the sound pressure level constraint is explored.

4.1 Methods

In order to conduct this study, the initial wind farm layouts for the optimization and the frequency of wind directions were identified. The turbine wake and acoustic models were also defined in a way that could be used for a gradient-based optimization. This meant that the models needed to be smooth (continuous gradients), have no flat areas in the function values, and provide values both quickly and accurately. The following sections describe in more depth the wind farms chosen for the optimization, the wake and acoustic models used, and the techniques implemented for the gradient-based optimization.

4.1.1 Wind Farm Locations

In an effort to make the research applicable to a real-world situation, the general layout of two actual wind farms were used as models for the optimization. These wind farms were selected due to problems they have had with noise disturbance in the past [58, 59]. The purpose of the

research is not to suggest redesign of existing wind farms, as this would be would be unrealistic environmentally and financially. Rather it is to explore the potential benefits of including acoustic impacts during the initial layout process instead of correcting the problems later on with costly alterations of blades or significant rotation speed reductions.

The first wind farm was based on the Lissett Airfield Wind Farm in East Yorkshire, England, which was constructed on a former Royal Air Force airfield and is now run by Infinis Energy PLC [60]. It was found that high wind speeds in certain directions caused an increase in turbine noise, so efforts were made to reduce the noise by slowing the turbine rotation [58]. While slowing the turbines down decreases the turbine noise, it also decreases power production. Repositioning turbines to more optimal locations could decrease the noise disturbance from the turbines without sacrificing power production. The specifications of this wind farm include twelve Nordex N90-2.5MW turbines with 90-meter rotor diameters creating two rows of turbines [61]. The actual wind farm boundary follows the curves of the property line of the former airfield, but the wind farm boundaries were simplified to a rectangular area to allow for linear constraints. To act as points of sound measurements, seven villages and residences located near the wind farm were chosen. The wind farm layout used in the optimization can be seen in Fig. 4.1. Due to a lack of weather information of the actual wind farm, the wind direction frequencies used in the optimization were based on weather data at Humberside Airport located about 48 kilometers south of the wind farm [12]. The wind direction frequencies can be seen in the wind rose in Fig. 4.2, which is a plot describing the annual percentage of time that the the wind blows from at a given location.

The second wind farm was based on the Rosiere Wind Farm run by Madison Gas and Electric in Kewaunee County, Wisconsin. This location was an interesting case study as individuals who lease the land to the company still live within the bounds of the wind farm; they even plant crops right up to the base of the turbines in some cases [62]. Since noise control would be important to individuals living so close to the turbines, the research explored positioning and changing the rotational speed of each turbine to reduce noise while keeping the turbines within the limits of their respective leased property. The specifications of this wind farm include seventeen Vestas V47-660kW turbines with 47-meter (154-foot) rotor diameters spread out into two geographic regions separated about two kilometers from each other [62]. Simplifications were also made on the wind farm's boundaries by straightening the slightly curved property lines. Twelve residential

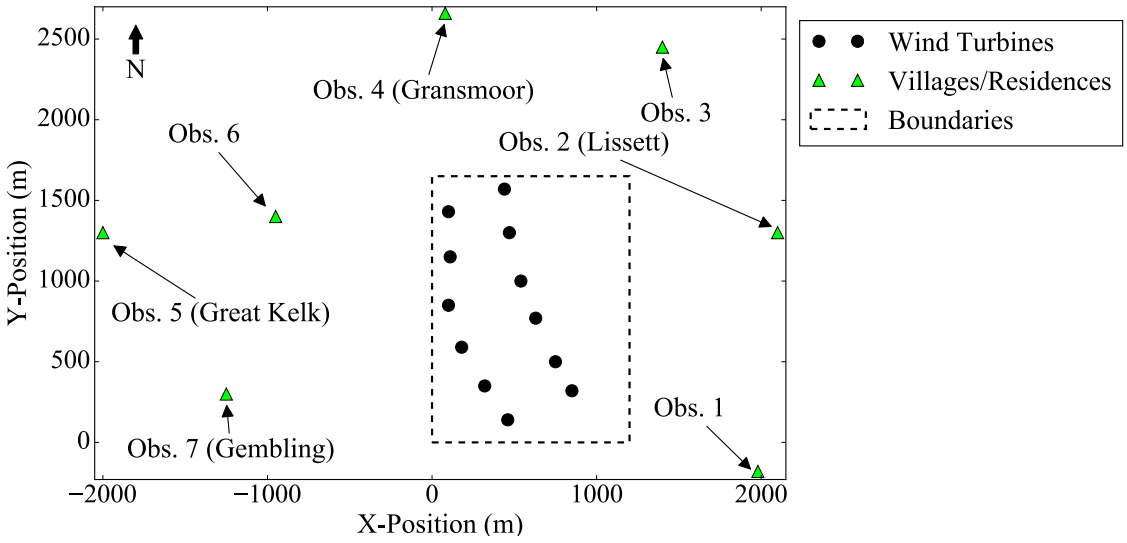

Figure 4.1: An approximation of the layout of the Lissett Airfield Wind Farm used as a reference in the first case study. Each of the seven observer locations used for the sound measurements are indicated as well as the farm boundary used in the optimization. Distances are given in meters.

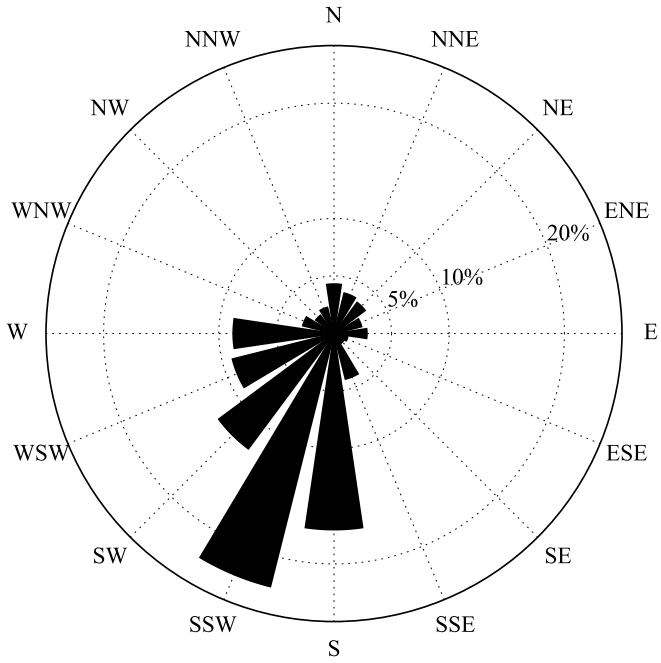

Figure 4.2: A wind rose indicating the average annual wind direction frequency at Humberside Airport located about 48 kilometers from the Lissett Airfield Wind Farm [12]. This data was used for the optimization in the first case study.

locations were used as the sound measurement references and can be seen in Fig. 4.3, located within the turbine boundaries in many cases. The wind direction frequencies were based on the company's weather database [13] shown in the wind rose in Fig. 4.4.

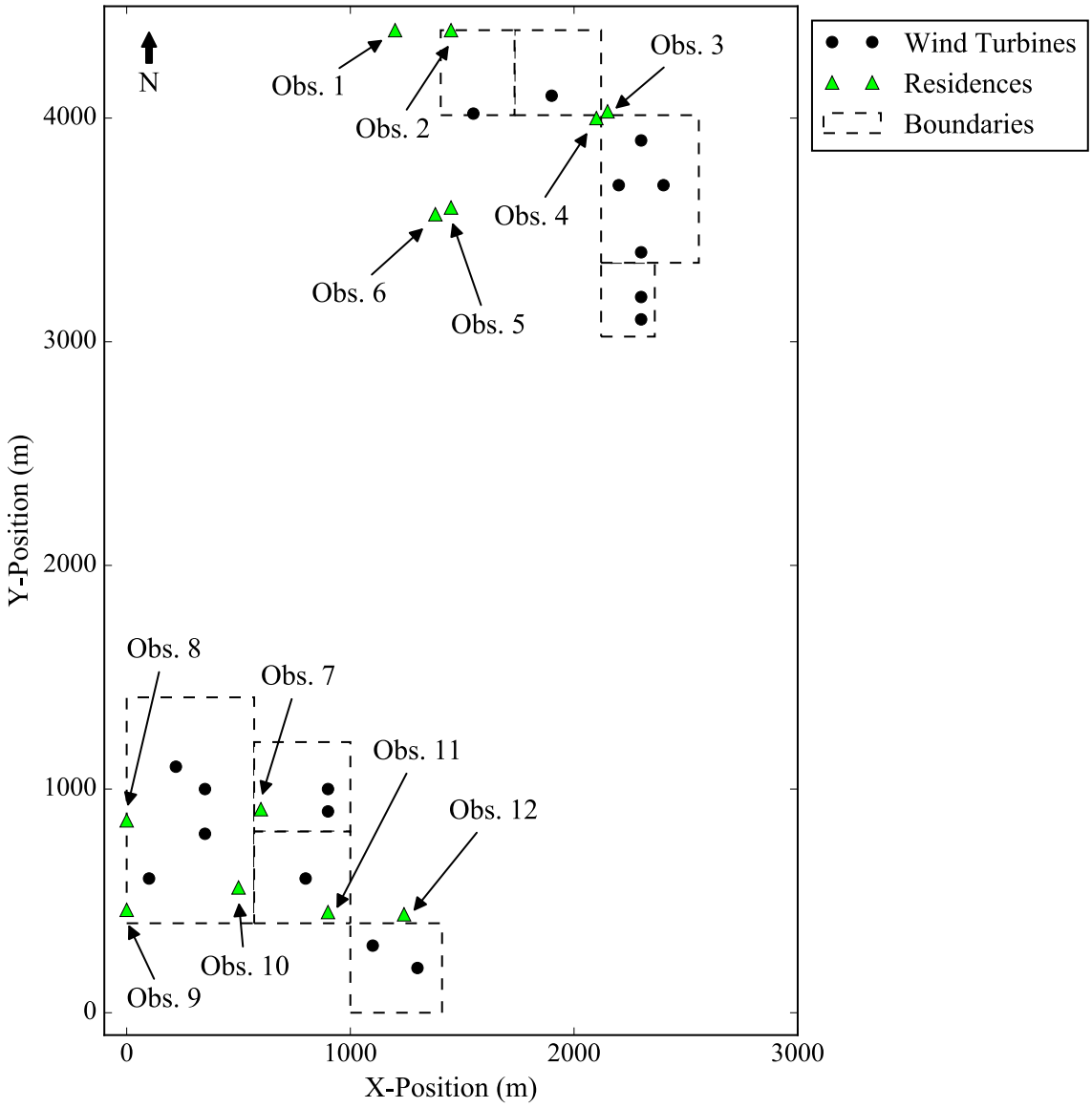

Figure 4.3: An approximation of the layout of the Rosiere Wind Farm used as a reference in the second case study. Each of the twelve observer locations used for the sound measurements are indicated. The turbines are all located within the leased boundaries shown. Distances are given in meters.

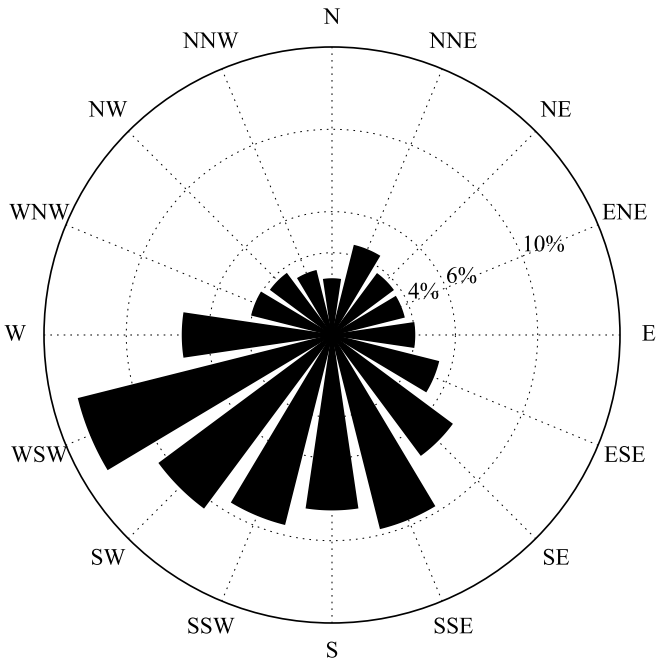

Figure 4.4: A wind rose indicating the average annual wind direction frequency at the Rosiere Wind Farm used in the second case study [13].

Although the wind speed varies during the operation of a wind farm, the wind speed used in the optimization was fixed at the rated wind speed of the respective turbines: 14 m/s for the Lissett Airfield Wind Farm and 15 m/s for the Rosiere Wind Farm. These wind velocities were chosen in order to produce the rated power of an isolated turbine. To discover at what point the average power production would approach zero for decreasing noise level limits, the rotation rates were allowed to range from zero to the maximum rotation speed of the respective turbines: 16.1 RPM for the Lissett Airfield Wind Farm and 28.5 RPM for the Rosiere Wind Farm. All of these values were based on published information for the Nordex and Vestas turbines used on the wind farms [61, 63]. Although the Vestas turbines used in the Rosiere Wind Farm operate at a fixed rotation speed, the turbines were allowed to vary in rotation rate to lower the SPL limit like the Nordex turbines in the Lissett Airfield Wind Farm and produce similar trends in average power production and SPL between the two wind farms.

4.1.2 Wake and Acoustic Models

This thesis used the FLOw Redirection and Induction in Steady-state (FLORIS) model to predict wake velocity deficits of HAWTs more accurately than the Jensen model, the wake model used in the previous research of Kwong et al. and Sorkhabi et al. [46, 47] The FLORIS model works by splitting the wake into different zones called the near wake, the far wake, and the mixing zone and accounting for decay and offset of the wake propagation while assuming constant properties in the cross-wind direction of each zone (illustrated in Fig. 4.5) [14]. Further work was conducted to refine the FLORIS model by making the wake velocity distribution smooth and providing gradients that would allow a gradient-based optimization to perform more effectively [64]. The power capacity of the turbines used in the optimization was adjusted to match the the actual turbines as much as possible using calculated power curves.

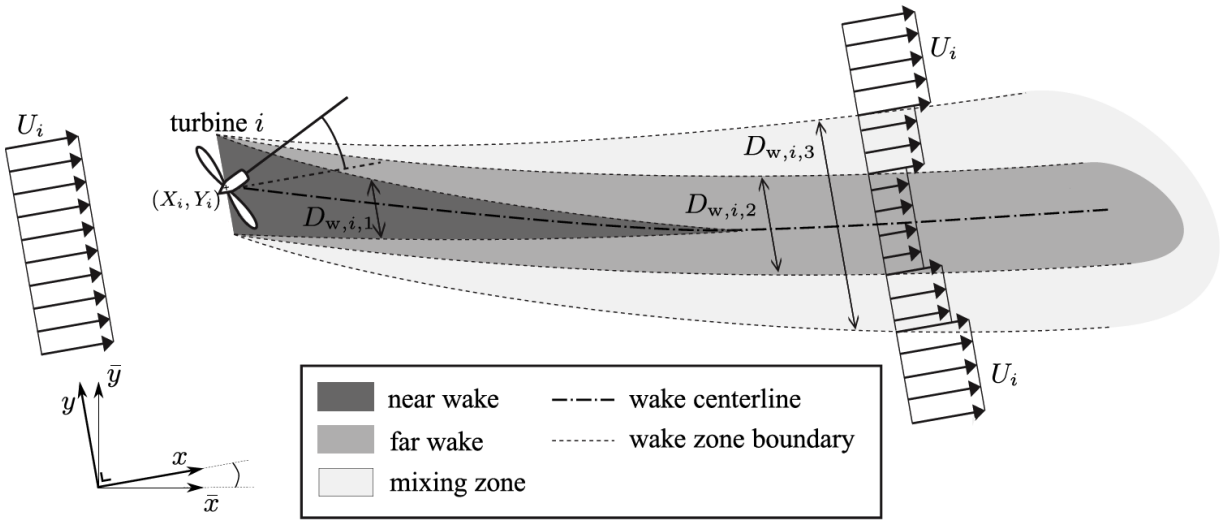

Figure 4.5: A diagram of the FLORIS model taken from the work of Gebraad et al. showing the three wake regions with respective diameters (D_w), the wind velocity in front of a turbine (U_i), and the influence turbine yaw has on the propagation of the wake downstream [14].

The acoustic model used in this research was based on the BPM equations developed for HAWTs [5], which are described in more detail in Chapter 2 and Appendix C. As explained, the acoustic equations were all developed and validated using NACA 0012 airfoil data [6]. Since the turbines used at the two wind farms do not have NACA 0012 blade cross-sections, as described

in the turbine documentation [61, 63], the acoustic model was calibrated in this research with a correction factor of 0.86 for the Rosiere Wind Farm and 0.82 for the Lissett Airfield Wind Farm to match published noise data [62, 65]. The BPM equations contained sharp discontinuities in the gradients moving to the sides and above the turbine, and quadratic fitting was used to provide a smooth transition through these discontinuous regions for more effective gradient-based optimization. Fig. 4.6 shows an example of the SPL distribution of the Nordex turbine with three 45-meter long blades rotating at 16.1 RPM in 13.5 m/s wind, illustrating how the noise is loudest in front of and behind the turbine and much quieter to the sides. The turbine noise with respect to an observer, in this case, could be minimized to the nearly an imperceivable noise level of 20 dB 400 meters to the sides of the turbine or be maximized to almost 55 dB in front and behind of the turbine.

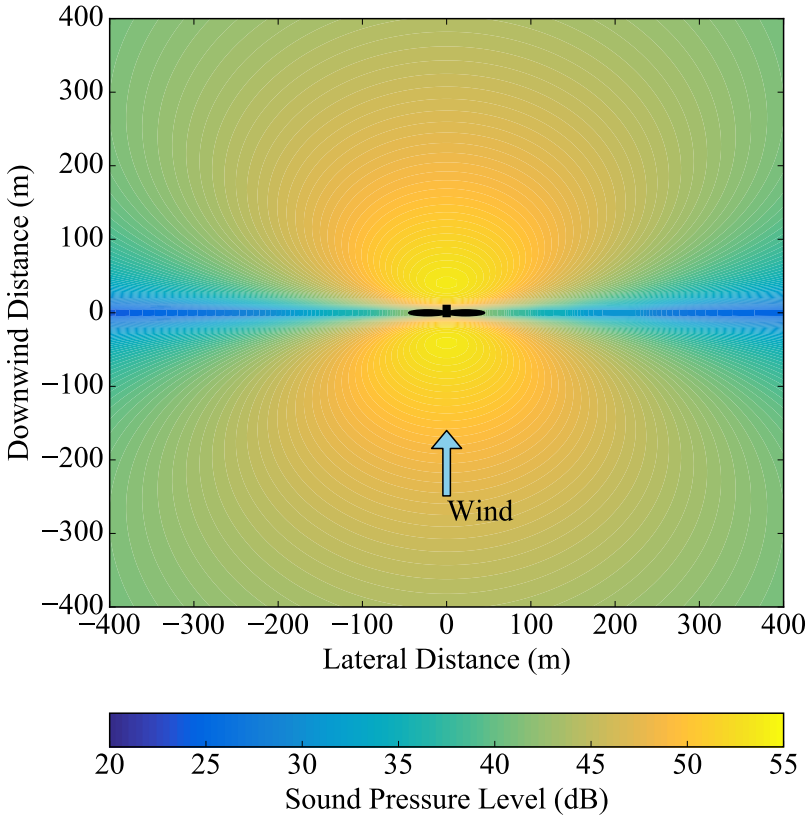

Figure 4.6: An example of the sound pressure distribution calculated by the BPM equations for the Nordex turbine with three 45-meter long blades rotating at 16.1 RPM in 13.5 m/s wind moving in the direction indicated. The sound pressure level measurement, in decibels (dB), is calculated for an observer at a given lateral and downwind position of the turbine, in meters, at ground level.

With the correction factors and smoothing made, the acoustic model was implemented with the turbine specifications of the two wind farms. Due to the lack of information of the actual geometry of the turbine blades, the blade geometry of the theoretical NREL 5MW turbine was used and dynamically scaled to bring the diameter of the turbine to the size of the turbines in the wind farms [66]. Initial power and noise levels were calculated using the wake and acoustic models based on the original positions of each of the turbines and observer locations using the described calibrations, which can be seen in Table 4.1. As shown, the Lissett Airfield Wind Farm with fewer turbines has a greater average power production than the Rosiere Wind Farm due to the higher power production of the Nordex turbines. The SPL is typically greater at the Rosiere Wind Farm due to the close proximity of the turbines to the observers within the boundaries of the wind farm.

Table 4.1: Initial Wind Farm Layout Measurements

Lissett Airfield Wind Farm	
Average Power Production: 27.27 MW	
Maximum Sound Pressure Levels	
Observer 1: 43.05 dB	Observer 5: 40.78 dB
Observer 2: 42.98 dB	Observer 6: 44.56 dB
Observer 3: 42.82 dB	Observer 7: 43.07 dB
Observer 4: 43.36 dB	

Rosiere Wind Farm	
Average Power Production: 10.78 MW	
Maximum Sound Pressure Levels	
Observer 1: 44.66 dB	Observer 7: 51.92 dB
Observer 2: 46.37 dB	Observer 8: 49.44 dB
Observer 3: 51.74 dB	Observer 9: 50.81 dB
Observer 4: 51.87 dB	Observer 10: 50.17 dB
Observer 5: 46.05 dB	Observer 11: 51.99 dB
Observer 6: 45.62 dB	Observer 12: 50.65 dB

4.1.3 Optimization

The research used the gradient-based SNOPT [53] to maximize power production of the wind farm while enforcing the bounds of the turbine positions and a specified SPL limit. For the optimization to be effective, the evaluated functions need to be smooth and free of flat areas and discontinuities to prevent the optimization from failing in these areas. The optimization in the two case studies was defined by:

$$\begin{aligned}
\text{maximize} \quad & P(x,y,\Omega) \\
\text{with respect to} \quad & x_i, y_i, \Omega_{iw}, \quad i = 0,1,...,m \\
& \qquad\qquad\qquad w = 0,1,...,q \\
\text{subject to} \quad & s_{i,j} \geq 2D, \quad i,j = 0,1,...,m \\
& x_{low} \leq x_i \leq x_{high}, \quad i = 0,1,...,m \\
& y_{low} \leq y_i \leq y_{high}, \quad i = 0,1,...,m \\
& 0 \leq \Omega_{iw} \leq \Omega_{max}, \quad i = 0,1,...,m \\
& \qquad\qquad\qquad w = 0,1,...,q \\
& SPL_k \leq SPL_{limit}, \quad k = 0,1,...,n
\end{aligned} \tag{4.1}$$

where $P(x,y,\Omega)$ is the average power production of the wind farm based on the x and y locations of each of the m turbines in the wind farm and the rotation rate (Ω) for each turbine in each of the q wind directions. The spacing between turbines i and j ($s_{i,j}$) was set to be at least two times the turbine diameter (D). The turbines were constrained between the lower and upper x and y boundaries of the wind farm limits (x_{low}, x_{high}, y_{low}, and y_{high}). The rotation rate of the turbines in this conceptual study was also constrained between zero and a given maximum rotation rate (Ω_{max}). The SPL at each of the n observers was constrained to a given SPL limit. Because different wind directions would produce a different SPL for each observer, the limit was enforced for all wind directions to ensure that an observer was never subjected to a higher SPL than specified. The feasibility tolerance was allowed to be within a tenth of a decibel, as such a small difference in SPL would not be audibly detectable by an observer [43].

4.2 Results

The optimization was run with many SPL limits for each wind farm to gain results of the impact noise level limits have on the power production of the wind farm. When the SPL limit was sufficiently high, the optimization proceeded as if there was no SPL limit and produced results similar to other wind farm layout optimization studies by moving turbines out of wake regions and maintaining an optimal rotation speed. Once the SPL constraint was lowered to make it active in the optimization, the turbines moved further from the observer locations. At some point, simply repositioning the turbines could not quiet the wind farm enough and rotation rates were slowed. The following sections present more detailed results from the Lissett Airfield Wind Farm and the Rosiere Wind Farm case studies.

4.2.1 Optimization of the Lissett Airfield Wind Farm

The optimization of the Lissett Airfield Wind Farm was conducted by starting each of the twelve turbines in their original locations with a rotation rate of 16.1 RPM. The SPL limit was varied in the range of 20 to 80 dB and did not have an effect on the results of the optimization until it dropped below 45 dB. When the SPL limit was kept above 45 dB, the optimal average power production attained was just under 29.5 MW (an 8.01% increase from the original layout) by moving turbines away from each other towards the bounds of the wind farm, as seen in Fig. 4.7. This type of behavior was expected as when turbines are far from each other, the wake interference is minimized and turbines can receive more wind energy. In each of these configurations, rotation rates were kept at about 16 RPM with a few exceptions where a slower rotation rate would maximize the turbine's power capacity with slower moving winds.

As the SPL limit was reduced below 45 dB, the turbines began to be repositioned further away from the observers and closer to each other, as seen in Fig. 4.8 where the SPL limit was set at 35 dB. Because turbines were closer together, more significant wake interference between the turbines was experienced and reduced the maximum power the turbines could attain by 74% in this case. Rotation rates were also decreased as the SPL limit was decreased further until the point where some turbines were spinning slower than 10 RPM below 33 dB. Although a rotation rate as low as zero was acceptable for this conceptual layout optimization, it would not be recommended

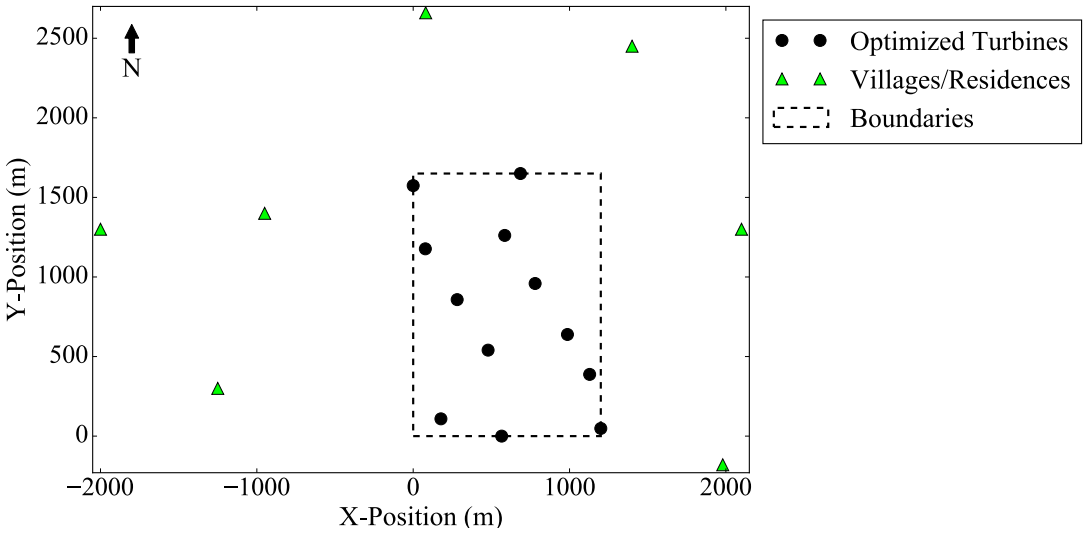

Figure 4.7: The optimized layout of the Lissett Airfield Wind Farm with no active SPL limit. Distances are given in meters.

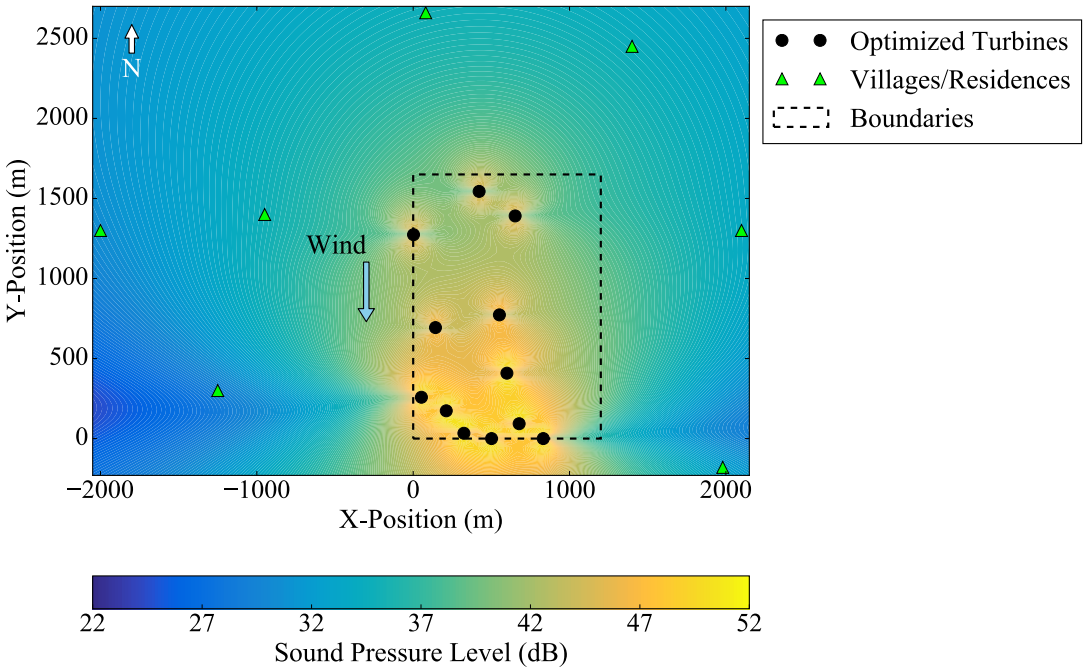

Figure 4.8: An example of the optimized layout of the Lissett Airfield Wind Farm with a 35 dB limit enforced. The contour map shows the sound pressure levels (in decibels) for the wind direction indicated that caused the highest noise levels to the observers although the optimization considered all wind directions in the turbines' positions. Distances are given in meters.

for an actual wind farm. At extremely low SPL limits, turbines had to significantly curtail power production.

Comparing the various SPL limits with the optimal average power production values obtained, a Pareto front was formed and can be seen in Fig. 4.9. The dashed lines in the chart indicate the average power production and the highest SPL from the original turbine layout as a point of reference. As seen in this specific curve, an SPL limit above 39 dB allowed the optimizer to increase the average power production from the original layout but dropping below 39 dB began to significantly impact the wind farm's ability to produce power. This represents a decrease of about 5.17 dB for the same average power production as the original layout simply by repositioning and adjusting the rotation rate of the turbines.

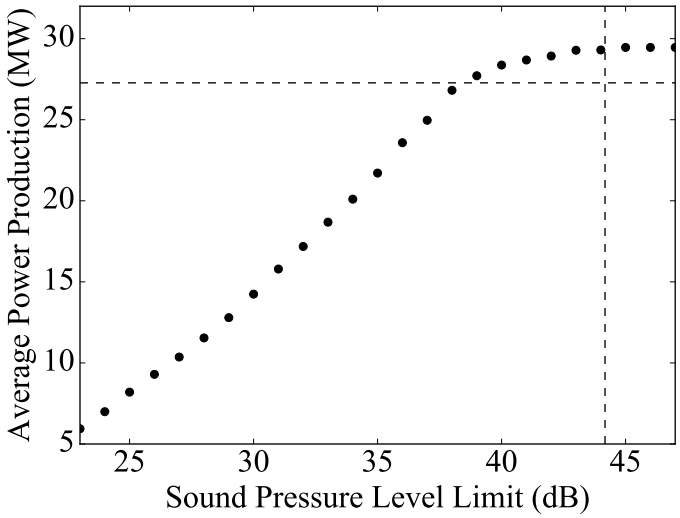

Figure 4.9: A Pareto front of the Lissett Airfield Wind Farm comparing the wind farm's average power production in megawatts (MW) to the SPL limit in decibels (dB). The dashed lines indicate the average power production and the SPL of the original layout.

4.2.2 Optimization of the Rosiere Wind Farm

The optimization of the Rosiere Wind Farm was conducted in the same way by starting the turbines in their original locations with a rotation rate of 28.5 RPM. The SPL limit was varied for the optimizations over a range from 30 to 60 dB and similar results to the previous case study were

found. While the trend in average power production decrease was the same as the Lissett Airfield Wind Farm, the different turbines used in this wind farm resulted in lower average power production values. When the SPL limit was effectively not active above 50 dB, the optimal average power production was about 11.2 MW (a 3.63% increase from the original layout) with the configuration seen in Fig. 4.10. Again, as expected, the turbines were positioned away from each other as much as possible while keeping them within their respective leased property boundaries. The rotation rate for each of the turbines also stayed near 28 RPM.

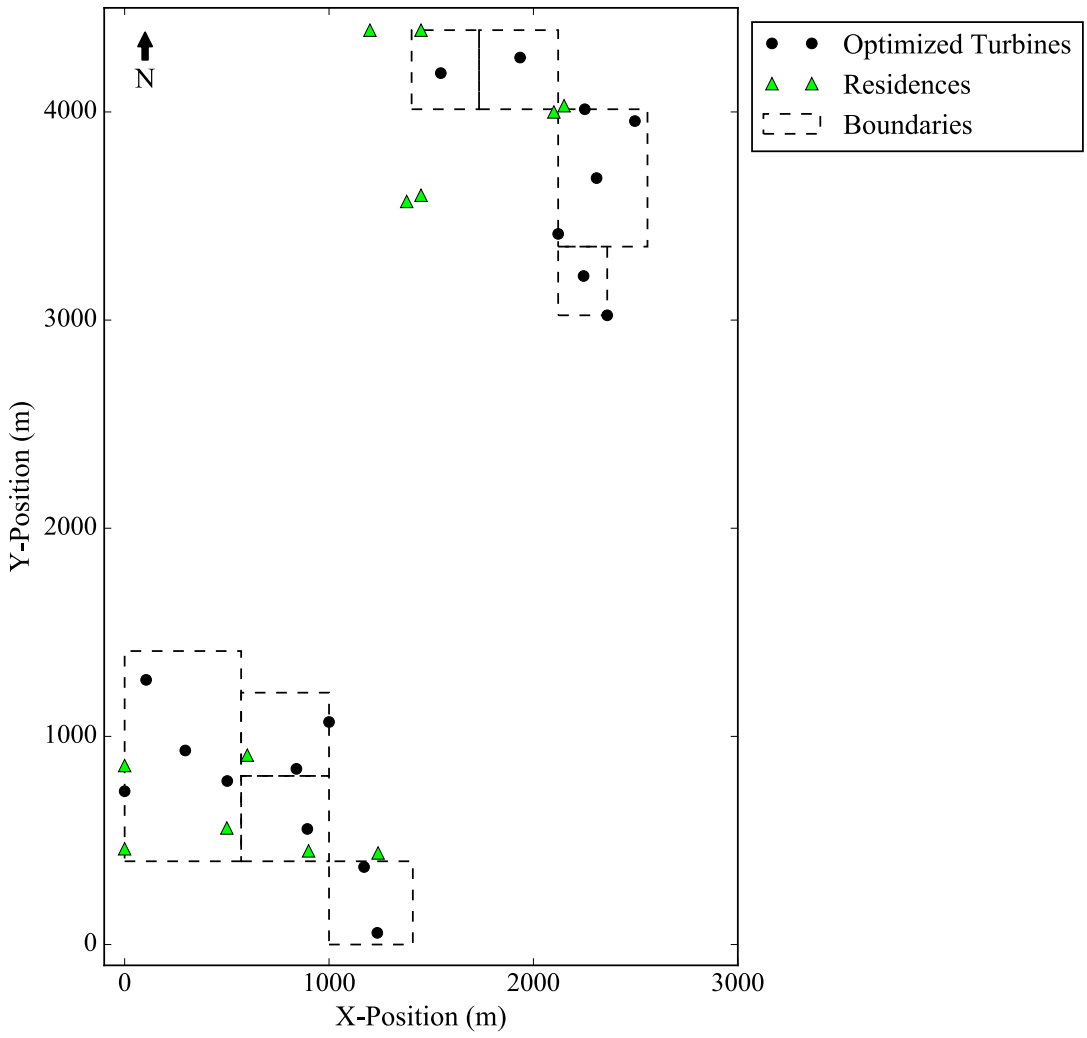

Figure 4.10: The optimized layout of the Rosiere Wind Farm with no active SPL limit. Distances are given in meters.

As the SPL limit was decreased, the optimization began to reposition the turbines away from the observers and decrease the rotation rates to minimize the noise, similar to the previous case study. Fig. 4.11 shows an example of the optimized layout with an SPL limit of 42 dB moving the turbines towards the boundaries of the wind farm away from observer locations.

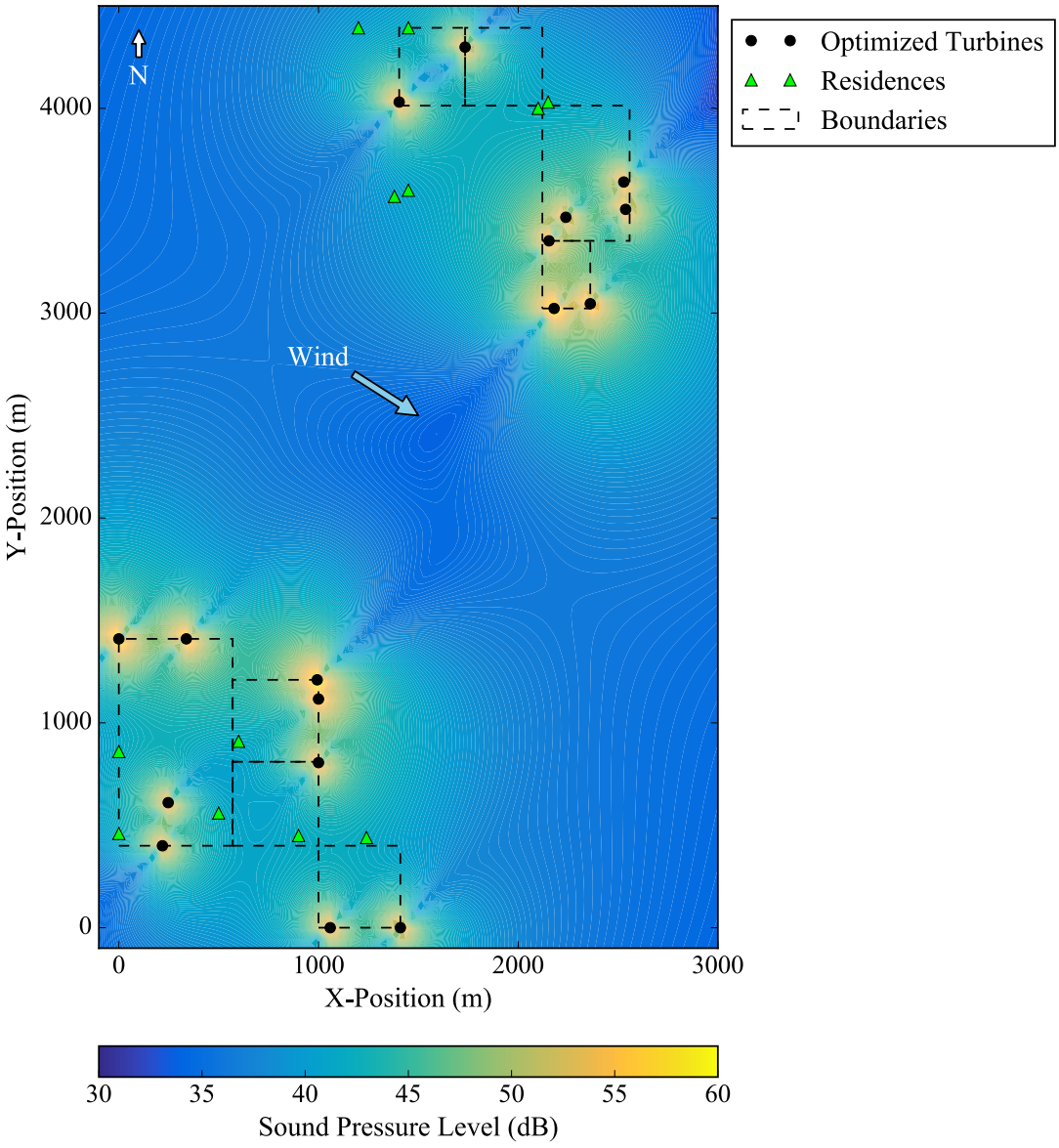

Figure 4.11: An example of the optimized layout of the Rosiere Wind Farm with a 42 dB limit enforced. The contour map shows the sound pressure levels (in decibels) for the wind direction indicated that caused the highest noise levels to the observers although the optimization considered all wind directions in the turbines' position. Distances are given in meters.

For this wind farm, a Pareto front of optimal average power productions for different noise level constraints was also created, shown in Fig. 4.12 where the dashed lines represent the values for the initial layout. As can be observed, using an SPL limit above 47 dB (4.84 dB lower than the original layout) still allowed the optimizer to increase the wind farm's average power production from the original layout, but below this the power production began to be significantly impacted.

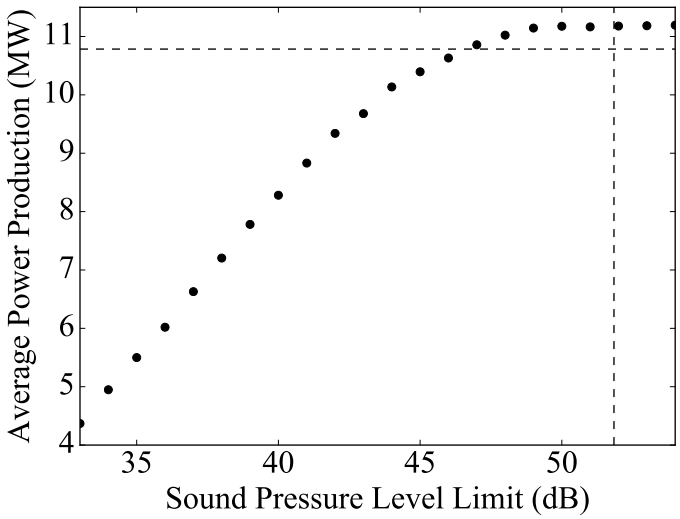

Figure 4.12: A Pareto front of the Rosiere Wind Farm comparing the wind farm's average power production in megawatts (MW) to the SPL limit in decibels (dB). The dashed lines indicate the average power production and the SPL of the original layout.

4.2.3 Discussion of Results

As shown in the two case studies, power production increased and the noise disturbance was reduced in reference to the original layout of the wind farms for a given range of SPLs. These results were possible because this optimization problem was very multi-modal, meaning that many local optimums existed in the design space (see Fig. 4.13). As the wakes behind turbines cause a very complex velocity field that turbines could be placed in, there are several turbine locations and a wide range of rotation rates that would result in an increased power production. Taking advantage of this principle, the research included a noise level constraint in the optimization rather than a sequential technique of optimizing average power production and SPL separately. Because

there were many optimal locations of turbines, the optimizer could search for a solution that had little impact on the average power production but that would reduce the noise significantly.

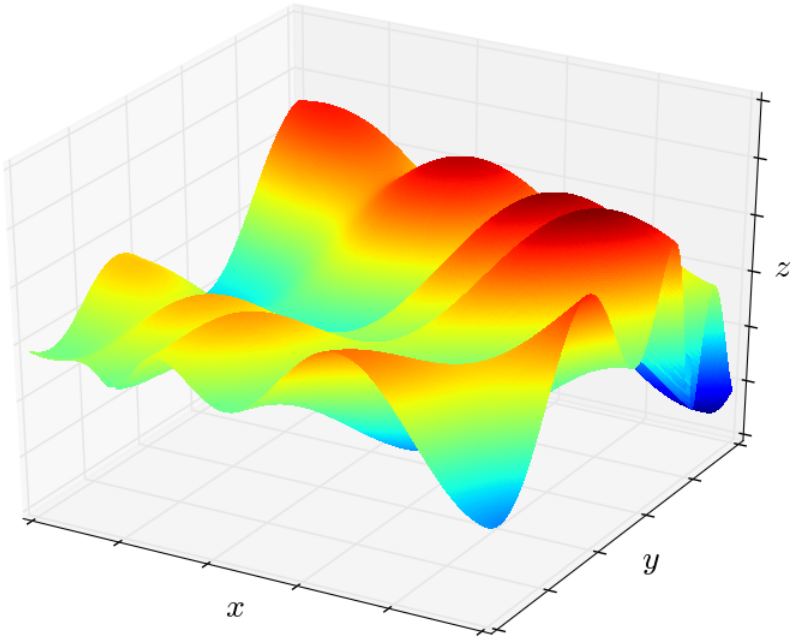

Figure 4.13: An example of a multi-modal design space across two dimensions showing many local maximums and minimums.

However, the presence of many local optimums presented challenges comparing each of the optimized average power production values at the different SPL levels. Because many solutions existed that satisfied the optimization problem, instances where a result at a lower SPL limit produced a greater average power production value than a result at a higher SPL limit were found. As this was expected due to the inherent multi-modality of the optimization, efforts were made to re-run these instances using the results of similar SPL limits to create Pareto fronts that followed the same trend. Since the purpose in this research was to compare the trade-offs between average power production and SPL limit of a wind farm optimization, this method of finding consistency in the decreasing trend of average power production values at continuously lower SPL limits allowed for a better understanding of the relationship between the two parameters.

Greater confidence was gained in the values obtained from the optimization by comparing them with real-world data. In both studies, the average power production could be increased in the decibel range of the upper 40's to the lower 50's. This agreed with the general trend of SPL limits imposed on various wind farms around the world [42–44] and gives validity to the assumptions made for both wind farms.

4.3 Acoustic Model Adjustment for VAWTs

This chapter has described the effect that a noise level constraint has on the maximum power production of an optimized wind farm using the BPM equations developed for HAWTs. Therefore, adjustments to the BPM equations are necessary in order to model the noise produced by VAWTs. The first consideration is that HAWT blades always operate at the same angle of attack with a constant downstream distance from the blades to an observer location. However, due to the vertical orientation of their blades, VAWTs operate with constantly varying angles of attack. This causes the chord reference angle (Θ_e) to vary continuously while the span reference angle (Φ_e) and the observer distance (r_e) remain relatively constant. These differences in the orientation of the directivity values can be seen in Fig. 4.14.

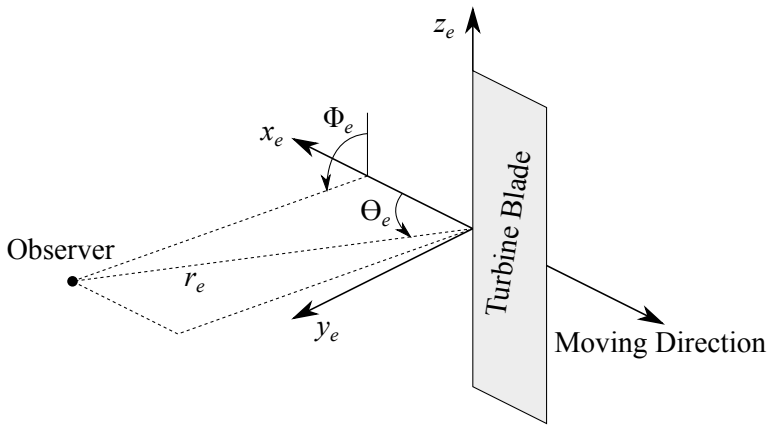

Figure 4.14: A diagram showing important parameters used for the directivity functions, similar to Fig. 2.3, oriented for the rotation of VAWT blades.

The second consideration for the VAWT acoustic adjustments is the wind speed over the turbine blades. While HAWTs generally operate with a constant incoming wind speed over their blades, the rotation of VAWT blades about a vertical axis at constantly varying angles of attack with respect to the free stream wind causes the wind speed over the blades to change at each rotational increment. Combining the velocity vectors of the free stream wind, nearby wake interference, and the motion of the blades for each rotational increment, an SPL can be computed for a VAWT using the BPM equations. The acoustic profile produced around a VAWT, as seen in Fig. 4.15, has a slight dipole-shaped distribution while radiating outward more evenly than the HAWT acoustic profile (Fig. 4.6). These changes, described in more detail in Appendix C, allow the BPM equations to be used in VAWT wind farm layout optimization with noise level constraints.

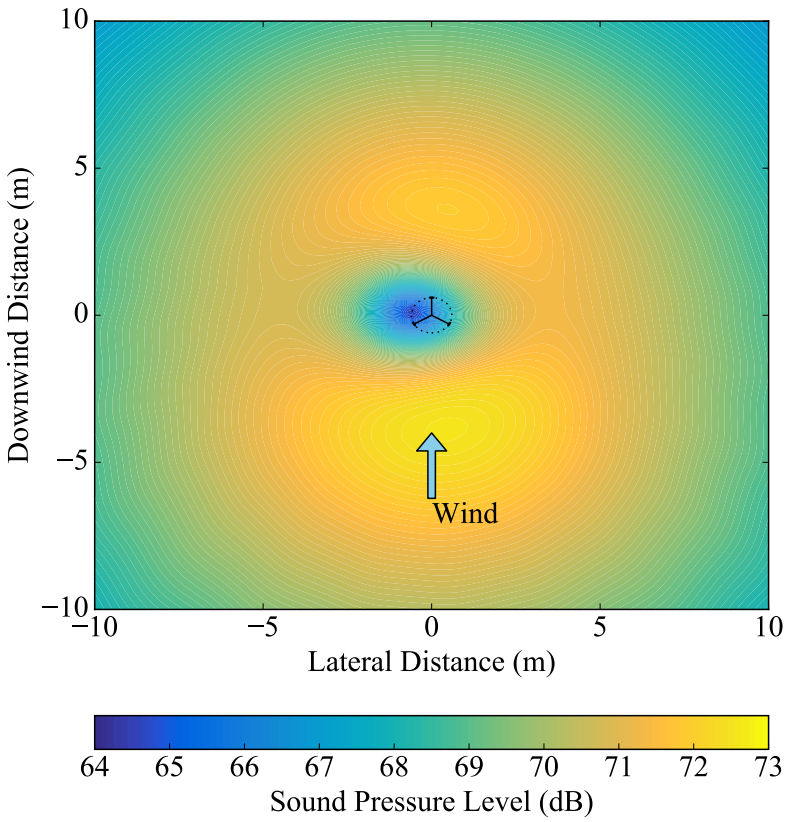

Figure 4.15: An example of the sound pressure level distribution calculated by the modified BPM equations for an isolated Mariah Windspire 1.2 kW VAWT in 8 m/s wind with a 1.2-meter diameter, three 6.1-meter long blades, and operating at a TSR of 2.625 rotating counter-clockwise. The sound pressure level measurement, in decibels (dB), is calculated for an observer at a given lateral and downwind position of the turbine, in meters, at ground level.

4.4 Conclusions

For this research, both wake interactions and turbine noise were considered in an optimization to maximize the wind farm's average power production while holding the SPL constraint at a specified level. By using the FLORIS wake model, wakes were described more accurately than the Jensen model by calculating a more detailed wake structure, decay, and expansion. The BPM equations also allowed the turbine acoustics to be modeled better than the ISO-9613-2 standard, used by previous research efforts [46, 47], by accounting for the distance and orientation of an observer location from the turbine as well as the speed and size of the turbine itself. The research also implemented an approach that allowed the optimizer to position the turbines anywhere inside the boundaries of the wind farm. Implementing these techniques with the two specific wind farms studied, the wind farm's average power production could be increased by up to 8.01% in the Lissett Airfield Wind Farm and 3.63% in the Rosiere Wind Farm by adjusting the placement of the turbines with respect to each other. As a noise restriction is active, this power output begins to diminish slightly over a range of about 5 dB, after which the average power production sharply decreases for quieter noise limitations. The significant decrease in SPL, with essentially no decrease in average power production, illustrates the benefit of introducing reasonable noise constraints during wind farm layout optimization. This advantageous result is possible because many local optimums exist when maximizing average power production, all with very similar performance, but some with lower noise levels. If noise and power are considered separately, the solution obtained for the maximum average power production would dictate the noise level of the wind farm and likely require additional acoustic shielding or curtailing of performance.

Understanding the propagation of wakes and noise from turbines can assist in designing wind farm layouts. Typically, turbines should not be placed in wake regions or close enough to residential areas where the acoustic distribution of the turbine would produce louder noise levels than acceptable environmental regulations. As this research has shown, an overly restrictive SPL limit can significantly impact the wind farm's ability to maximize its average power production and negatively affect the wind farm's cost efficiency. In order to avoid these negative outcomes, proper planning in the initial layout process is needed to determine where the turbines are located with respect to residential areas nearby as well as the wake propagation effects from other turbines to allow a wind farm to quietly maximize its power production. As seen in this study, a range of SPL

limits exist where a 5 dB quieter wind farm has about a 5% impact on its average power production due to the optimizer taking advantage of the complex, multi-modal wind velocity profile. However, as the SPL limit becomes quieter than 5 dB, the average power production is impacted by nearly 1 MW for each decibel decease.

In order for the BPM equations to be used for VAWTs, adjustments were made to the equations to reflect the specific rotation of VAWT blades and their orientation with a nearby observer. As VAWT wind farms in urban environments would need noise control, the use of the adjusted BPM equations for VAWT wind farm layout optimization is important to limit the noise produced by the turbines while maximizing the power production of the wind farm.

There are opportunities for future work in wake and acoustic modeling and optimization of wind farms. As was explained in the results section, wind farm layout optimization using wake models can have many local optimums. This means a better solution may exist by placing turbines in a different arrangement with different rotation rates. As one can never be certain the best solution has been obtained through optimization of non-convex problems, more confidence in the results can be gained by using a multi-start approach where initial turbine locations and rotation rates are varied over many optimization runs. Although the comparison study conducted did not require a multi-start approach to observe the trends of average power production and SPL, future research should look into the possibility of maximizing a wind farm's average power production even more using a multi-start approach.

CHAPTER 5. CONCLUSIONS

Wind energy is a valuable source of clean and renewable power production and VAWTs have shown particular promise in their use in offshore and urban environments due to their size and operation. In order to fully integrate VAWTs into wind farm power production, considerations of the wakes and noise VAWTs produce must be taken into account to minimize both negative wake interference between turbines and noise disturbance to nearby residential areas. To perform any wind farm layout analysis or optimization using VAWTs, a reduced-order wake model is needed to provide velocity calculations in a short amount of time with reasonable accuracy. This type of wake model has not been available for VAWTs, but this thesis has proposed a wake model for the use of VAWTs in wind farm layout applications. Through CFD modeling and trend analysis, a VAWT wake model based on CFD vorticity data was developed that compared well with experimental results. This wake model is extendable and can be made more accurate with the addition of more wake data. Using aerodynamic loading of VAWT blades, a turbine power can also be calculated for the ability to predict the power production of a wind farm layout.

In using VAWTs near residential areas, turbine acoustics was also explored in this thesis and the trade-offs between average power production and noise level restrictions was demonstrated. Using a gradient-based optimization approach with accurate wake and acoustic modeling, turbines were positioned freely within the wind farm to maximize power production while maintaining the noise below a specified limit. Because of the multi-modality of the wind farm layout optimization problem, considering both power and acoustic effects simultaneously has the benefit of finding an optimal solution that maximizes power with a significant reduction in turbine noise. An adjusted acoustic model for VAWTs was also presented that would allow for noise constraints to be imposed for a VAWT wind farm layout optimization.

The rest of this chapter outlines the main results of the thesis and presents areas of future research to continue the advancement of VAWT and turbine acoustic study.

5.1 Overview of Main Results

The efforts in this research have produced many valuable results, both in the area of turbine wake and acoustic research. Some important conclusions are:

- The CFD analysis of isolated, two-dimensional VAWTs showed consistent trends in the wake structures at different tip-speed ratios and solidities. These nondimensional parameters served as a basis to develop a parameterizable VAWT wake model.
- As the velocity structure of the VAWT wake is very complex and difficult to capture numerically, the vorticity structure (consisting of concentrated streams) was captured using an exponentially modified Gaussian distribution with four parameters. Cross-validation and the use of polynomial surfaces allowed the wake model to be accurate and robust at all tip-speed ratios and solidities within the ranges modeled.
- The developed VAWT wake model demonstrates an improvement over the CFD data, capable of predicting wake velocity deficits with a normalized root mean error of 0.059 in about 0.02 seconds. The same calculation using CFD takes about a day to perform on the local BYU supercomputer.
- Compared to two additional experimental VAWT studies considered in this thesis, the developed wake model matches with a percent difference of the maximum wake deficit of 6.3% with one and 14.6% with the other. This agreement demonstrates the applicability of the wake model with data sets other than the one used to produce the initial model.
- After adjustments were made to the wake model's implementation to account for multiple wake interaction, turbine blade loading, and power calculation, the method of using the wake model with the actuator cylinder model matches well with CFD findings showing a slight increase in power production of two closely spaced counter-rotating VAWTs.
- Using the FLORIS wake model and the BPM equations in the optimization of two HAWT wind farm layouts when a noise level constraint was not active, the average power production was increased, up to 8.01% in one farm and 3.63% in the other, simply by repositioning

the turbines within the boundaries of the wind farm and adjusting the rotation rates of the turbines. This illustrated the impact wake interference can have on a wind farm.

- When a noise level constraint was active in the optimization of the two HAWT wind farms, the average power production of the farm could be improved while reducing the noise disturbance by 5 dB. Because the optimization problems were significantly multi-modal, several optimal solutions could be found with significant noise reductions while maintaining increased power results.

5.2 Areas of Future Work

The VAWT wake and acoustic models described in this thesis are new developments for use in wind energy. The final goal of both of these models is their use in wind farm layout analysis and optimization of VAWTs while limiting the noise disturbance of the wind farm. During the research process, rough and noisy areas were found along the wake structure causing the optimizer to terminate before an optimal solution was found. In order to run an optimization using VAWTs, smoothing of the wake model is necessary for the optimizer to function correctly.

To make the process of data collection and analysis systematic over the large range of configurations studied, only two-dimensional CFD simulations were run. While the data did produce accurate wake predictions, it neglected the occurrence of tip vortex formation and the vertical growth of the wake. This initial wake model was meant to provide the means of studying VAWTs within wind farms, but can still be expanded further to account for the effects of three-dimensionality. Future studies of VAWTs with different heights would certainly need to account for the three-dimensional effects of VAWT blades.

During the CFD trend analysis and wake model validation studies, there were not significant differences in the predicted wake deficits between the different blade shapes used or atmospheric differences between Reynolds numbers of 600,000 and 6,000,000. As such, the current VAWT wake model neglects these factors while still agreeing well with the experimental studies. However, further research may indicate that these factors may be important in predicting wake deficits more accurately. The aerodynamic loading of VAWTs has already shown that blade shape is important to calculate lift and drag coefficients used in the actuator cylinder model, and future

research could explore the effects of lift and drag, as well as atmospheric conditions, in the VAWT wake structure.

In the area of acoustics, it was stated that the multi-modality of the optimization problems allowed for the power to be maximized and the noise to be constrained simultaneously. The multi-modality also lead to solutions with a higher probability of being a local optimum rather than a global. While the certainty of finding a global optimum for non-convex problems can never be sure, a higher chance of finding one is obtained when a multi-start approach is implemented. This thesis did not require multi-starting to increase the chance of finding a global optimum to illustrate the trade-offs between turbine power production and sound pressure level constraints, but future studies could investigate further ways to increase the likelihood of higher power productions in wind farm layout optimization.

To conclude, wind energy is an important resource offered to society and this thesis has presented information and results to both improve the use of wind energy and assess the ability of wind farms in producing electrical power. It is anticipated that future work will expand on the methods presented here, but this research of VAWT wakes and turbine noise will assist in the advancement of effective wind energy use. All of the materials, data, and results described in this thesis are publicly available for academic and industrial use and can be openly accessed through the BYU FLOW Lab website (`http://flow.byu.edu/publications`). The CFD simulation models and wake data can be accessed directly through Figshare (`https://figshare.com/articles/Parameterized_Wake_Model/2059947`) and GitHub repositories are also available for the VAWT wake model (`https://github.com/byuflowlab/vawt-wake-model`) and the BPM acoustic models (`https://github.com/byuflowlab/bpm-turbine-acoustics`). Through the continued effort of wind turbine research, wind energy can become a more efficient way for society to produce power.

REFERENCES

[1] Colby, W. D., Dobie, R., Leventhall, G., Lipscomb, D. M., McCunney, R. J., Seilo, M. T., and Søndergaard, B., 2009. Wind turbine sound and health effects: an expert panel review Tech. rep., American Wind Energy Association and Canadian Wind Energy Association, December. vii, 6, 14

[2] U.S. Department of Energy, 2017. The inside of a wind turbine. viii, 2

[3] Kjellin, J., Bülow, F., Eriksson, S., Deglaire, P., Leijon, M., and Bernhoff, H., 2011. "Power coefficient measurement on a 12 kW straight bladed vertical axis wind turbine." *Renewable Energy,* **36**, pp. 3050–3053. viii, 3, 17, 20, 35, 73

[4] Oerlemans, S., Sijtsma, P., and López, B. M., 2007. "Location and quantification of noise sources on a wind turbine." *Journal of Sound and Vibration,* **299**, February, pp. 869–883. viii, 7

[5] Brooks, T. F., Pope, D. S., and Marcolini, M. A., 1989. Airpower self-noise and prediction Tech. rep., NASA, July. viii, 11, 12, 13, 48, 87, 95

[6] Moriarty, P. J., and Migliore, P., 2003. Semi-empirical aeroacoustic noise prediction code for wind turbines Tech. rep., National Renewable Energy Laboratory, December. viii, 13, 48

[7] Tescione, G., Ragni, D., He, C., Ferreira, C. S., and van Bussel, G., 2014. "Near wake flow analysis of a vertical axis wind turbine by stereoscopic particle image velocimetry." *Renewable Energy,* **70**, pp. 47–61. viii, 5, 18, 19, 35

[8] Battisti, L., Zanne, L., Dell'Anna, S., Dossena, V., Persico, G., and Paradiso, B., 2011. "Aerodynamic measurements on a vertical axis wind turbine in a large scale wind tunnel." *Journal of Energy Resources Technology,* **133**, September. x, 37

[9] Madsen, H. A., 1982. "The actuator cylinder – a flow model for vertical axis wind turbines." PhD thesis, Aalborg University Centre, January. x, 38, 39

[10] Zanforlin, S., and Nishino, T., 2016. "Fluid dynamic mechanisms of enhanced power generation by closely spaced vertical axis wind turbines." *Renewable Energy,* **99**, December, pp. 1213–1226. x, 3, 23, 40, 41

[11] Ning, A., 2016. "Actuator cylinder theory for multiple vertical axis wind turbines." *Wind Energy Science*, November (accepted). x, 3, 23, 38, 40, 41

[12] RenSMART, 2010. Wind speed distribution for humberside (EGNJ). x, 44, 45

[13] Pitts, S. R., 2015. personal communication, April. xi, 46, 47

[14] Gebraad, P. M. O., Teeuwisse, F. W., van Wingerden, J. W., Fleming, P. A., Ruben, S. D., Marden, J. R., and Pao, L. Y., 2014. "Wind plant power optimization through yaw control using a parametric model for wake effects—a CFD simulation study." *Wind Energy*. xi, 5, 48

[15] Dabiri, J. O., Greer, J. R., Koseff, J. R., Moin, P., and Peng, J., 2015. "A new approach to wind energy: Opportunities and challenges." In *AIP Conference Proceedings*. 1, 2, 3, 40

[16] Bazilevs, Y., Korobenko, A., Deng, X., Yan, J., Kinzel, M., and Dabiri, J. O., 2014. "Fluid-structure interaction modeling of vertical-axis wind turbines." *Journal of Applied Mechanics,* **81**, August. 1, 2

[17] Dayan, E., 2006. "Wind energy in buildings: Power generation from wind in the urban environment- where it is needed most." *Refocus,* **7**(2), March, pp. 33–38. 1

[18] Sandia National Laboratories, 2012. Offshore use of vertical-axis wind turbines gets closer look, July. 1, 3

[19] Dabiri, J. O., 2011. "Potential order-of-magnitude enhancement of wind farm power density via counter-rotating vertical-axis wind turbine arrays." *Journal of Renewable and Sustainable Energy,* **3**(4). 1, 3, 23, 40

[20] Manwell, J. F., McGowan, J. G., and Rogers, A. L., 2009. *Aerodynamics of Wind Turbines, in Wind Energy Explained: Theory, Design and Application*., second edition ed. John Wiley & Sons Ltd., Chichester, UK, ch. 3, pp. 91–155. 2

[21] Maples, B., Saur, G., Hand, M., van de Pietermen, R., and Obdam, T., 2013. Installation, operation, and maintenance strategies to reduce the cost of offshore wind energy Tech. Rep. NREL/TP-5000-57403, National Renewable Energy Laboratory, July. 2

[22] Sutherland, H. J., Berg, D. E., and Ashwill, T. D., 2012. A retrospective of VAWT technology Tech. rep., Sandia National Laboratories, January. 3

[23] Vermeer, L., Sørensen, J., and Crespo, A., 2003. "Wind turbine wake aerodynamics." *Progress in Aerospace Sciences,* **39**, pp. 467–510. 4

[24] Crespo, A., Hernández, J., and Frandsen, S., 1999. "Survey of modelling methods for wind turbine wakes and wind farms." *Wind Energy,* **2**, pp. 1–24. 4

[25] Sanderse, B., 2009. Aerodynamics of wind turbine wakes Tech. Rep. ECN-E09-016, Energy Centre of the Netherlands. 4

[26] Changshui, Z., Guangdong, H., and Jun, W., 2011. "A fast algorithm based on the submodular property for optimization of wind turbine positioning." *Renewable Energy,* **36**, pp. 2951–2958. 5

[27] Kusiak, A., and Song, Z., 2010. "Design of wind farm layout for maximum wind energy capture." *Renewable Energy,* **35**(3), pp. 685–694. 5

[28] Eroğlu, Y., and Seçkiner, S. U., 2014. "Design of wind farm layout using ant colony algorithm." *Renewable Energy,* **44**, pp. 53–62. 5

[29] Pérez, B., Mínguez, R., and Guanche, R., 2013. "Offshore wind farm layout optimization using mathematical programming techniques." *Renewable Energy,* **53**, pp. 389–399. 5

[30] Fleming, P. A., Ning, A., Gebraad, P. M. O., and Dykes, K., 2015. "Wind plant system engineering through optimization of layout and yaw control." *Wind Energy*, March. 5

[31] Gebraad, P. M., Thomas, J. J., Ning, A., Fleming, P. A., and Dykes, K., 2016. "Maximization of the annual energy production of wind power plants by optimization of layout and yaw-based wake control." *Wind Energy*, May. 5

[32] Sheldahl, R. E., and Klimas, P. C., 1981. Aerodynamic characteristics of seven symmetrical airfoil sections through 180-degree angle of attack for use in aerodynamic analysis of vertical axis wind turbines Tech. rep., Sandia National Laboratories, Advanced Energy Projects Division 4715, Sandia National Laboratories, Albuquerque, NM 87185, March. 5

[33] Sheldahl, R. E., 1981. Comparison of field and wind tunnel darrieus wind turbine data Tech. rep., Sandia National Laboratories, January. 5

[34] Worstell, M. H., 1978. Aerodynamic performance of the 17 meter diameter darrieus wind turbine Tech. rep., Sandia National Laboratories, September. 5

[35] Ferreira, C. J. S., 2009. "The near wake of the VAWT: 2D and 3D views of the VAWT aerodynamics." PhD thesis, Delft University of Technology. 5, 17

[36] Ferreira, C. S., Madsen, H. A., Barone, M., Roscher, B., Deglaire, P., and Arduin, I., 2014. "Comparison of aerodynamic model for vertical axis wind turbines." *Journal of Physics,* **524**. 5

[37] He, C., 2013. "Wake dynamics study of an H-type vertical axis wind turbine." Master's thesis, Delft University of Technology, August. 5

[38] Dixon, K. R., 2008. "The near wake structure of a vertical axis wind turbine: Including the development of a 3D unsteady free-wake panel method for VAWTs." Master's thesis, Delft University of Technology, April. 5

[39] Shamsoddin, S., and Porté-Agel, F., 2014. "Large eddy simulation of vertical axis wind turbine wakes." *Energies,* **7**, pp. 8990–8912. 5, 19

[40] Whittlesey, R. W., Liska, S., and Dabiri, J. O., 2010. Fish schooling as a basis for vertical axis wind turbine farm design Tech. rep., California Institute of Technology, February. 5

[41] Hesaveh, S. H., Bou-Zeid, E., Lohry, M. W., and Martinelli, L., 2016. "Simulation and wake analysis of a single vertical axis wind turbine." *Wind Energy*. 5

[42] Nieuwenhuizen, E., and Köhl, M., 2015. "Differences in noise regulations for wind turbines in four european countries." In *EuroNoise 2015*, European Acoustics Association. 6, 14, 59

[43] McAleer, S., and McKenzie, A., 2011. Guidance note on noise assessment of wind turbine operations at EPA licensed sites (NG3) Tech. rep., Environmental Protection Agency, June. 6, 14, 51, 59

[44] Patriot Renewables, 2010. Spruce mountain wind project, section 5: Noise Tech. rep., Spruce Mountain Wind, LLC, January. 6, 14, 59

[45] Yang, B., 2013. "Research status on aero-acoustic noise from wind turbine blades." *Materials Science and Engineering,* **52**. 6

[46] Kwong, W. Y., Zhang, P. Y., Romero, D., Moran, J., Morgenroth, M., and Amon, C., 2012. "Wind farm layout optimization considering energy generation and noise propagation." In *Proceedings of the ASME 2012 International Design Engineering Technical Conferences & Computers Information in Engineering Conference*. 6, 8, 48, 61

[47] Sorkhabi, S. Y. D., Romero, D. A., Yan, G. K., Gu, M. D., Moran, J., Morgenroth, M., and Amon, C. H., 2016. "The impact of land use constraints in multi-objective energy-noise wind farm layout optimization." *Renewable Energy,* **85**, January, pp. 359–370. 6, 8, 48, 61

[48] Tingey, E. B., and Ning, A., 2016. "Parameterized vertical-axis wind turbine wake model using CFD vorticity data." In *ASME Wind Energy Symposium (AIAA SciTech)*. 8

[49] Tingey, E. B., and Ning, A., 2016. "Development of a parameterized reduced-order vertical-axis wind turbine wake model." *AIAA Journal* (in review). 8

[50] Tingey, E. B., Thomas, J. J., and Ning, A., 2015. "Wind farm layout optimization using sound pressure level constraints." In *IEEE Conference on Technologies for Sustainability*. 8

[51] Tingey, E. B., and Ning, A., 2016. "Trading off sound pressure level and average power production for wind farm layout optimization." *Renewable Energy* (in review). 8

[52] Jamieson, P., 2011. *HAWT or VAWT?, in Innovation in Wind Turbine Design*. John Wiley & Sons Ltd., Chichester, UK, ch. 13, pp. 211–222. 10

[53] Gill, P., Murray, W., and Saudners, M., 2005. "SNOPT: an SQP algorithm for large-scale constrained optimization." *SIAM Review,* **47**, pp. 99–131. 15, 51

[54] Singh, A., Howard, K. B., and Guala, M., 2014. "On the homogenization of turbulent flow sstructure in the wake of a model wind turbine." *Phyics of Fluids,* **26**(2), February. 24

[55] Andersen, S. J., Sørensen, J. N., Mikkelsen, R., and Ivanell, S., 2016. "Statistics of LES simulations of large wind farms." *Journal of Physics: Conference Series,* **753**. 24

[56] Ali, N., Aseyev, A. S., Melius, M. S., Tutkun, M., and Ca, R. B., 2017. *Evaluation of Higher Order Moments and Isotropy in the Wake of a Wind Turbine Array, in Whither Turbulence and Big Data in the 21st Century?*. Springer International Publishing, Switzerland, ch. 15, pp. 273–292. 24

[57] Madsen, H. A., Larsen, T. J., Paulsen, U. S., and Vita, L., 2013. "Implementation of the actuator cylinder flow model in the HAWC2 code for aeroelastic simulations on vertical axis wind turbines." In *Proceedings of 51st AIAA Aerospace Sciences Meeting*, AIAA 2013-0913. 38

[58] Copping, J., and Gray, R., 2011. Switch-off for noisy wind farms, November. 43, 44

[59] Rosenbloom, E., 2006. A problem with wind power Tech. rep., AWEO. 43

[60] Infinis, 2015. Lissett airfield wind farm. 44

[61] Nordex, 2014. Gamma generation: Proven platform–for diverse locations around the world, September. 44, 47, 49

[62] Madison Gas and Electric, 2015. Rosiere wind farm. 44, 49

[63] Vestas Wind Systems, 2003. V47-660 kW: Pitch regulated wind turbine wind optitip and optislip, March. 47, 49

[64] Thomas, J. J., Gebraad, P. M. O., and Ning, A., 2016. "Improving the FLORIS wind plant model for compatibility with gradient-based optimization." *Wind Engineering* (in review). 48

[65] Nordex, 2010. Noise levels: Nordex N90/2500 HS Sales Document, April F008_149_A03_EN. 49

[66] Jonkman, J., Butterfield, S., Musial, W., and Scott, G., 2009. Definition of a 5-MW reference wind turbine for offshore system development Tech. Rep. NREL/TP-500-38060, National Renewable Energy Laboratory, 1617 Cole Boulevard, Golden, Colorado 80401-3393, February. 50

[67] Brooks, T. F., and Marcolini, M. A., 1986. "Airfoil tip vortex formation noise." *AIAA Journal,* **24**(2), pp. 246–252. 95

[68] Vargas, L. F. d., 2008. "Wind turbine noise prediction." Master's thesis, Technical University of Lisbon, November. 98, 99

APPENDIX A. CFD SIMULATION PROCEDURES

To develop the wake model development described in Chapter 3, large amounts of computational fluid dynamics (CFD) simulations of isolated VAWTs were created to obtain wake data at many different VAWT configurations using the program from CD-adapco called STAR-CCM+. The following describes the settings used in STAR-CCM+ to create the CFD models and all of the CFD simulation models and wake data obtained can be accessed at `https://figshare.com/articles/Parameterized_Wake_Model/2059947`.

To model an isolated VAWT in free stream wind, a fluid region with an 51-meter radius (8.5 diameters) was created in front and to the sides of the turbine and continued 213 meters (35.5 diameters) downstream to capture the wake data. The boundaries used for the fluid region can be seen in Fig. A.1 and their respective settings can be seen in Table A.1. Two wake refinement regions were also used to obtain more accurate wake data consisting of circles around the turbine interface with 8- and 20-meter diameters expanding downstream with a slope of 0.1. Four slightly different Reynolds numbers were modeled by varying the wind speed between 12 and 16 m/s.

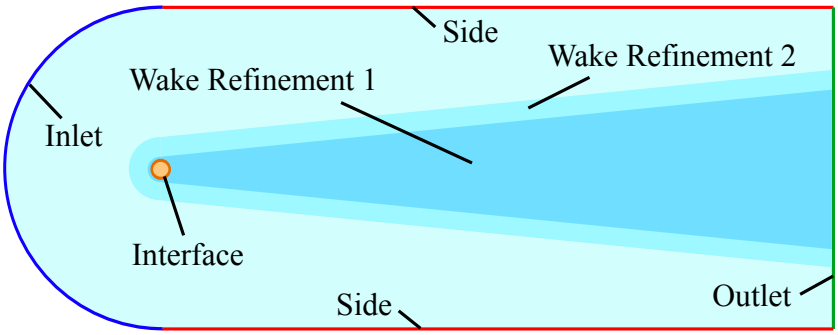

Figure A.1: The Fluid 2D region with the boundaries and wake refinement regions indicated that were used for the settings in Table A.1.

Table A.1: Fluid 2D Region Settings

Boundary	Setting	Value
Inlet and Side: Velocity Inlet	Velocity	[12.0-16.0, 0.0] m/s
	Turbulence Intensity	0.15
	Turbulence Viscosity Ratio	0.1
Interface: Internal Interface	Topology	In-place
	Intersection Tolerance	0.05
Outlet: Pressure Outlet	Backflow Direction Specification	Boundary-Normal
	Pressure Specification	Environmental
	Pressure	0.0 Pa

The rotating turbine region was created in a similar manner within a 6.6-meter diameter circle with three NACA 0021 blades and a 0.125-meter diameter axis in the middle, as shown in Fig. A.2. The specific geometry of the turbine was based originally on the Uppsala University 12 kW H-rotor VAWT with a 3-meter radius [3]. To produce the different solidities needed in the wake model parameterization, the chord length of the blades was varied between 0.15 and 1.0 meter. The settings for each of the turbine region boundaries are shown in Table A.2.

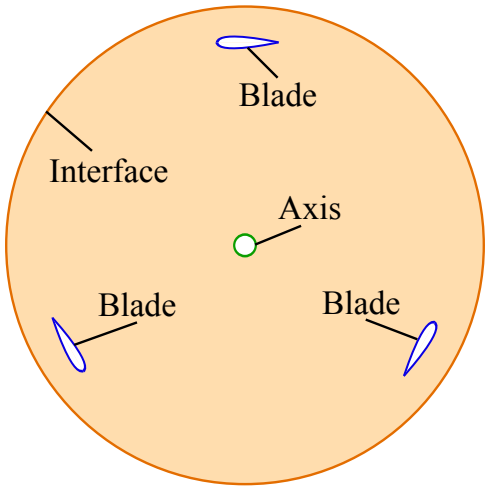

Figure A.2: The Turbine 2D region with the boundaries indicated that were used in the settings of Table A.2.

Table A.2: Turbine 2D Boundary Settings

Boundary	Setting	Value
Blade and Axis: Wall	Mesh Values	see Table A.4
	Shear Stress Specification	No-Slip
	Tangential Velocity Specification	Fixed
	Wall Surface Specification	Smooth
	Blended Wall Function- E	9.0
	Blended Wall Function- Kappa	0.42
Interface: Internal Interface	Topology	In-place
	Intersection Tolerance	0.05
Motion Specification		Stationary (steady) Rotation (transient)

To generate the mesh of the model, global settings were used, as shown in Table A.3, with values that were chosen based on the grid convergence study described in Chapter 3.

Table A.3: Global Meshing Settings

Setting	Value
Models	Polyhedral Mesher Prism Layer Mesher Surface Remesher
Base Size	1.0 m
Prism Layer Stretching	1.4
Surface Growth Rate	1.1
Minimum Surface Size	25% of Base
Target Surface Size	25% of Base
Volumetric Control 1 (wake refinement 1) Relative Size	10% of Base
Volumetric Control 2 (wake refinement 2) Relative Size	15% of Base

To model the boundary layer using prism layers on the blades and axis, the Reynolds number (Re) was first calculated:

$$Re = \frac{U_\infty c}{\nu} \tag{A.1}$$

where U_∞ is the free stream wind velocity, c is the blade chord length, and ν is the kinematic viscosity of the air. Using the Reynolds number, a boundary layer thickness (δ^*) was calculated:

$$\delta^* = \frac{0.382c}{Re^{1/5}} \tag{A.2}$$

To determine the sizing of the prism layers, the skin friction (C_f), the wall shear stress (τ_w), and the friction velocity (u_*) were then calculated using:

$$C_f = (2\ \log Re - 0.65)^{-2.3} \tag{A.3}$$

$$\tau_w = C_f \frac{1}{2} \rho U_\infty^2 \tag{A.4}$$

$$u_* = \sqrt{\frac{\tau_w}{\rho}} \tag{A.5}$$

where ρ is the density of the air. With a y^+ value of 1.0, the thickness of the first prism layer (y_w) was determined by:

$$y_w = \frac{y^+ \nu}{u_*} \tag{A.6}$$

Using the prism layer stretching value of 1.4 (see Table A.3), the number of prism layers was determined by how many layers were needed to model the entire boundary layer thickness. These values are shown for different chord lengths (to produce the different solidities) in Table A.4.

Table A.4: Boundary Layer Mesh Settings (for Blade and Axis)

Chord Length (m)	0.15	0.25	0.50	0.75	1.00
y_w Values (m)	1.95e-5	2.05e-5	2.19e-5	2.27e-5	2.33e-5
Number of Prism Layers	15	16	17	18	18
Prism Layer Thickness (m)	0.0053	0.008	0.014	0.0192	0.02415
Minimum Surface Size (m)*	0.00006	0.0001	0.0002	0.0003	0.0004
Target Surface Size (m)*	0.0015	0.0025	0.005	0.0075	0.01

* used for settings in the turbine region (see Table A.2)

Figs. A.3, A.4, and A.5 show examples of the meshes used in the far-field view of the model, the turbine region of the model, and the turbine blade using the prism layers.

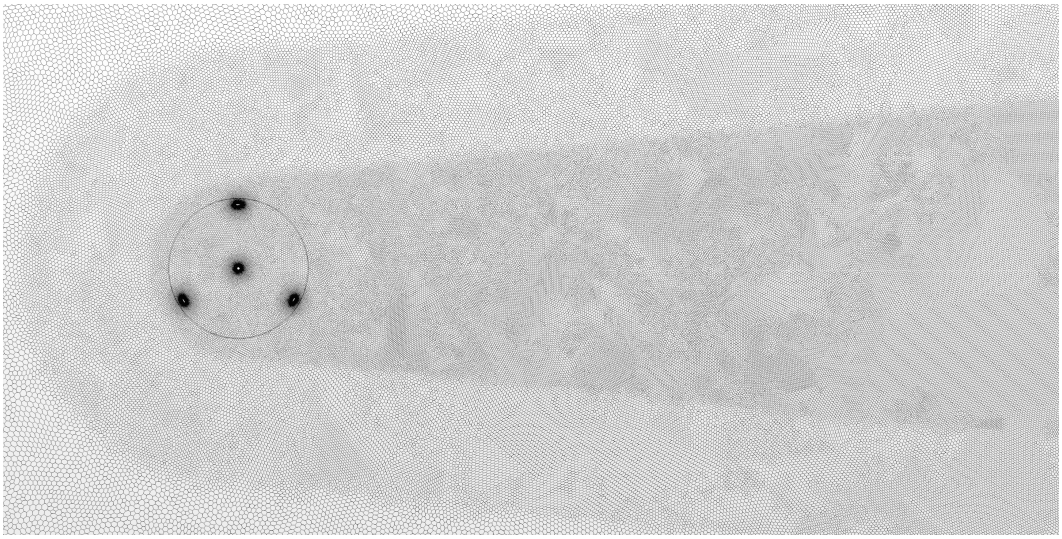

Figure A.3: An example of the CFD simulation mesh from a far-field view showing the wake refinement.

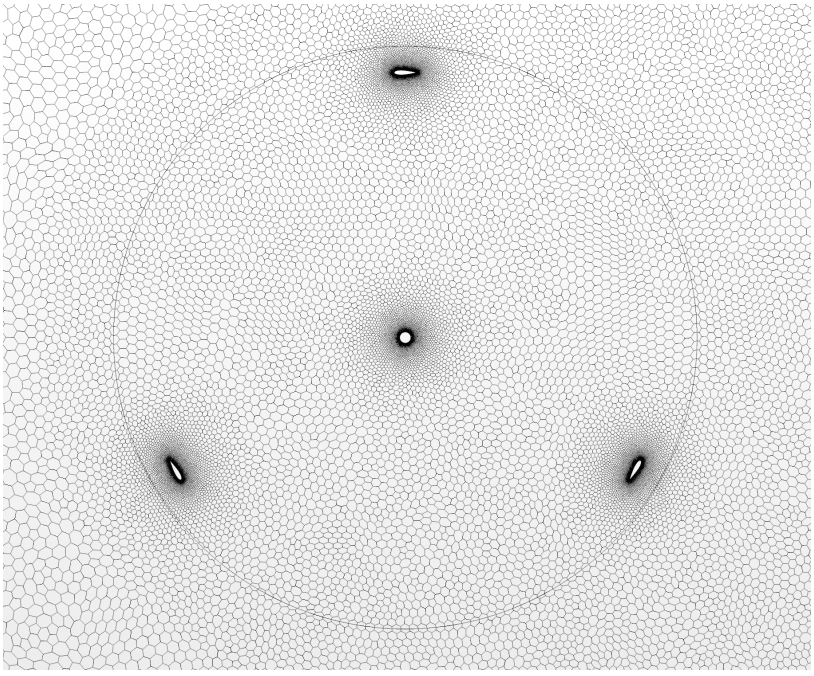

Figure A.4: An example of the CFD simulation mesh of the turbine region with refinement around the blades and axis.

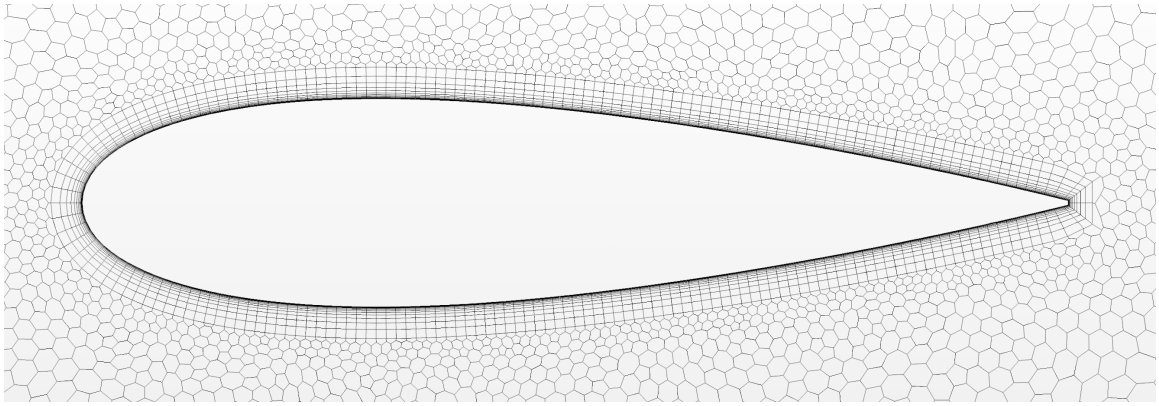

Figure A.5: An example of the CFD simulation mesh of a turbine blade showing the prism layers used to model the necessary refinement of the boundary layer.

Settings for the physics continuum of both steady and transient cases were made according to Table A.5 with Reynolds-averaged Navier-Stokes equations and K-epsilon turbulence models. A steady state solution (without the turbine rotating) was first used to converge the residual results and then the transient solution was used to solve for the wake velocities. The solvers used to calculate the fluid dynamic interactions of the simulations are described in Table A.6.

Table A.5: Physics Settings

Setting	**Value**
Models	Two Dimensional Steady (steady case)/Implicit Unsteady (transient case) Gas: Air ($\rho = 1.225$ kg/m^3, $\nu = 1.85508$e-5 Pa-s) Segregated Flow Gradients Constant Density Turbulent Reynolds-Averaged Navier-Stokes K-Epsilon Turbulence Realizable K-Epsilon Two-Layer Exact Wall Distance Two-Layer All y+ Wall Treatment
Reference Pressure	101325.0 Pa
Turbulence Intensity	0.15
Turbulence Velocity Scale	1.0 m/s
Turbulence Viscosity Ratio	0.1
Velocity	[12.0-16.0, 0.0] m/s

Table A.6: Simulation Solvers

Solver	Setting	Value
Implicit Unsteady	Time Step	0.001 s
(for Transient Physics Continuum)	Temporal Discretization	1st-order
Rigid Body Motion		
Partitioning	Partitioning Method	Per-Continuum
Wall Distance	Minimum Tree Size Threshold	500000
Segregated Flow	Velocity Under-Relaxation Factor	0.8
	Pressure Under-Relaxation Factor	0.2
	Ramp Method	No Ramp
	Max Cycles	30
	Convergence Tolerance	0.1
	Velocity Cycle Type	Flex Cycle
	Restriction Tolerance	0.9
	Prolongation Tolerance	0.5
	Sweeps	1
	Pressure Cycle Type	V Cycle
	Pre-Sweeps	1
	Post-Sweeps	1
	Max Levels	50
	Relaxation Scheme	Gauss-Seidel
K-Epsilon Turbulence	Under-Relaxation Factor	0.8
	Ramp Method	No Ramp
	Max Cycles	30
	Convergence Tolerance	0.1
	Cycle Type	Flex Cycle
	Restriction Tolerance	0.9
	Prolongation Tolerance	0.5
	Sweeps	1
	Relaxation Scheme	Gauss-Seidel
K-Epsilon Turbulence Viscosity	Under-Relaxation Factor	0.1
	Maximum Ratio	1000000.0

To indicate at what point the simulation would terminate, stopping criteria were used as shown in Table A.7. The simulations were run in a steady state for 15,000 steps and then in a transient state between 13.3 and 17.75 seconds to allow the initial wake region to move completely outside of the fluid domain of 213 meters (for $213/U_\infty$ seconds). Following this step, the wake region was time averaged for an extra 5 seconds to produce the wake data used for the reduced-order wake model.

Table A.7: Stopping Criteria Settings

Motion	**Setting**	**Value**
Steady	Maximum Steps	15000
Transient	Maximum Inner Iterations	20
	Maximum Physical Time	13.3-17.75 s
	Additional Physical Time for Time-Averaging	5.0 s

Additional settings used in the CFD simulations included the settings of the rotation orientation and rate ($\Omega = (\lambda U_\infty)/R$) with respect to TSR ($\lambda$) and the field mean monitor used for time-averaging (of both velocity and vorticity). These settings are shown in Table A.8.

Table A.8: Additional CFD Settings

Type	**Setting**	**Value**
Motions (Tools)	Rotation Axis	(0.0, 0.0, 1.0)
	Rotation Origin	(0.0, 0.0, 0.0) m
	Rotation Rate	6.0-37.333 radian/s
Field Mean (Monitors)	Delta Time Frequency	0.005 s

APPENDIX B. VAWT WAKE MODEL POLYNOMIAL SURFACES

Chapter 3 describes the development of a parameterizable reduced-order wake model for a VAWT using an exponentially modified Gaussian (EMG) distribution. To create the EMG curves, 2nd- and 3rd-order polynomial surfaces were used to calculate the coefficients used in Eq. (3.4). Limitations were imposed on the coefficient values to both produce expected trends in the wake and provide values that could be handled by the EMG distribution, which can be seen in Table B.1.

Table B.1: Limitations in the EMG coefficient values

Limitation Range	Reason
$\mu_1 \leq$ -0.001	ensure wake is concave inward
$\mu_2 \geq 0.01$	ensure slight increase in wake moving downstream
$\mu_3 \geq 0.48$	ensure wake originates from the edge of the turbine
$\psi_1 \leq$ -0.001	ensure the wake spreads downstream
$\psi_2 \leq 0.0$	ensure the wake begins spreading near the turbine
$\kappa_1 \in \mathbb{R}$	no limitations necessary
$\kappa_2 \leq 0.0$	ensure the skewness begins in the correct orientation
$\zeta_1 \geq 0.0$	ensure the maximum vorticity strength is positive
$\zeta_2 \geq 0.05$	ensure the decay of the wake downstream
$\zeta_3 \geq 0.0$	ensure the wake decays downstream of the turbine

The polynomial surface data is provided in Table B.2 based on the equation for each coefficient:

$$\text{Coefficient} = a + b\lambda + c\sigma + d\lambda^2 + e\lambda\sigma + f\sigma^2 + g\lambda^3 + h\lambda^2\sigma + i\lambda\sigma^2 + j\sigma^3 \qquad \text{(B.1)}$$

where λ is a given TSR and σ is a given solidity. These equations produce the polynomial surfaces for each of the EMG parameter coefficient shown in Figs. B.1-B.10. The wake model code for VAWTs can be accessed at `https://github.com/byuflowlab/vawt-wake-model`.

Table B.2: Coefficients used for the polynomial surface fits

Coefficient	a	b	c
μ_1	0.0025703809856661534	-0.0007386258659065129	0.004595508188667984
μ_2	-0.5047504670963536	0.23477391362058556	0.8414256436198028
μ_3	0.2878345841026334	0.11512552658662782	0.7303949879914625
ψ_1	0.08234816067475287	-0.03530687906626052	-0.3662863944976986
ψ_2	-0.07083579909945328	0.016182024377569406	0.1985436342461859
κ_1	-1.6712830849073221	1.5625053380692426	-6.180392756736983
κ_2	-3.423561091777921	-9.228795430171687	86.95722105482042
ζ_1	-0.19815381951708524	0.08438758133540872	1.2650146439483734
ζ_2	2.3932787625531815	-2.020874419612962	-8.938221963838357
ζ_3	104.40501489600803	-29.942999569370276	-174.42008279158216

Coefficient	d	e	f
μ_1	0.000380123563204793	-0.0005090098755683027	0.005744581813281894
μ_2	-0.04252528528617351	-0.06962875967504166	-0.6566907653208429
μ_3	-0.007035517839387948	-0.18284850673545897	-0.5241921153256568
ψ_1	0.003240141344532779	0.12172015102204112	0.2993048183466721
ψ_2	0.0017738254727425816	-0.09111094817943823	-0.06561408122153217
κ_1	-0.20407668040293722	-4.6476103643607685	29.380064536220306
κ_2	2.772872601988039	-11.968168333741515	-150.61261090270446
ζ_1	-0.007606115512168328	-0.2747023984740461	-0.8844640101378567
ζ_2	0.576323845480877	2.8782448498416944	16.598492450314534
ζ_3	3.708514822202037	25.14336546356742	132.35546551746415

Coefficient	g	h	i
μ_1	-4.103393770815313e-05	-0.0014146918534486358	-0.013975958482495927
μ_2	0.002839318332370807	0.00571803958194812	0.0070744372783060295
μ_3	-0.0003704899921255296	0.010972527139685873	0.04380801537377295
ψ_1	0.0	-0.009253185586804007	-0.057469126406649716
ψ_2	-0.0005115133402638633	0.009434288536679505	0.022392136905926813
κ_1	0.0	0.7502978877582536	-0.16358232641365608
κ_2	-0.24715316589674527	0.5283723108899993	4.537286811245538
ζ_1	0.0	0.01870057580949183	0.0699898278743648
ζ_2	-0.04746016700352029	-0.197101203594028	-1.3860007472886064
ζ_3	-0.16479555172343271	-1.351556690339512	-6.721810844025761

Coefficient	j	TSR Fit Order	Solidity Fit Order
μ_1	0.0	3rd order	2nd order
μ_2	0.228052864388909 95	3rd order	3rd order
μ_3	0.1724129349605399	3rd order	3rd order
ψ_1	-0.07257633583877886	2nd order	3rd order
ψ_2	0.0	3rd order	2nd order
κ_1	-19.937609244085568	2nd order	3rd order
κ_2	82.50581844010263	3rd order	3rd order
ζ_1	0.2794360008051127	2nd order	3rd order
ζ_2	-8.289767128060362	3rd order	3rd order
ζ_3	-40.39565289044579	3rd order	3rd order

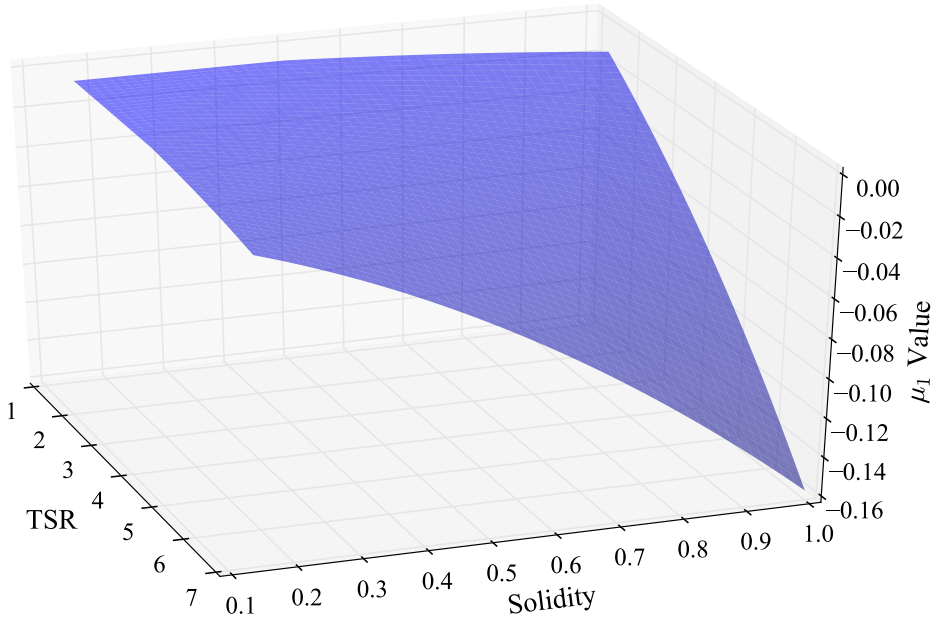

Figure B.1: The polynomial surface used to calculate μ_1 as a function of TSR and solidity.

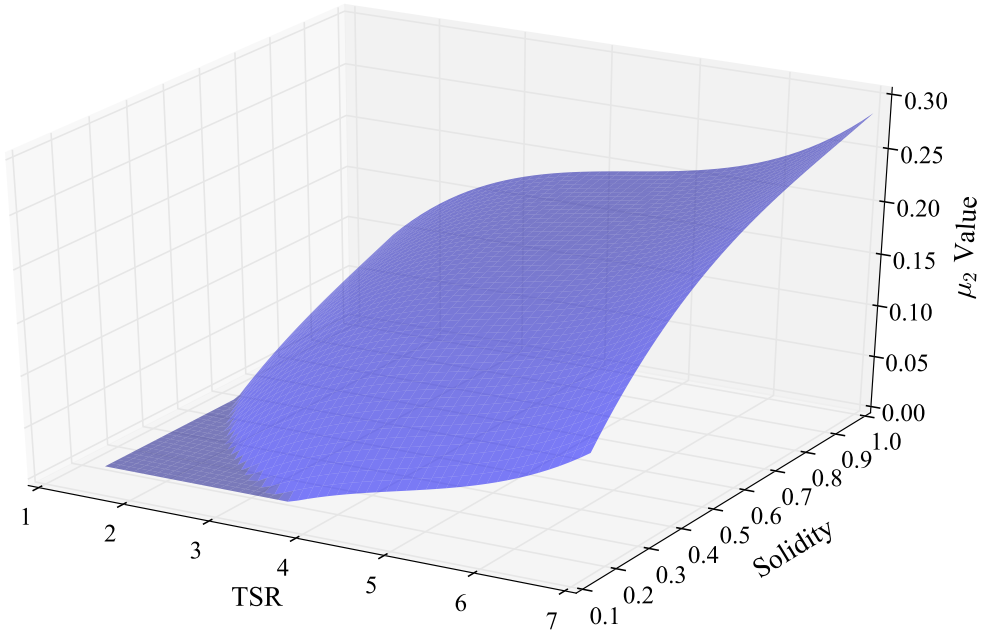

Figure B.2: The polynomial surface used to calculate μ_2 as a function of TSR and solidity.

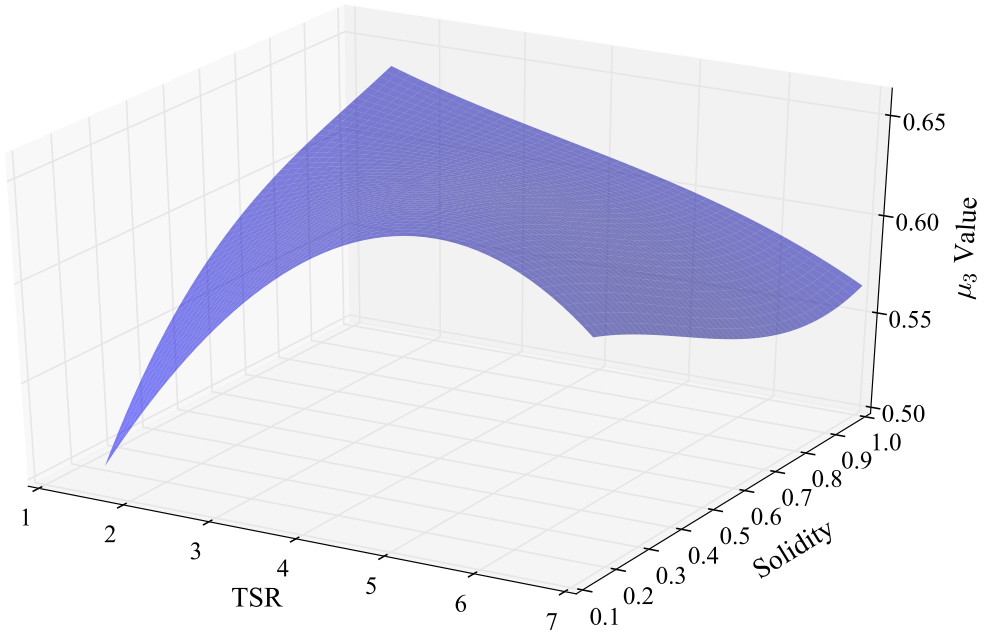

Figure B.3: The polynomial surface used to calculate μ_3 as a function of TSR and solidity.

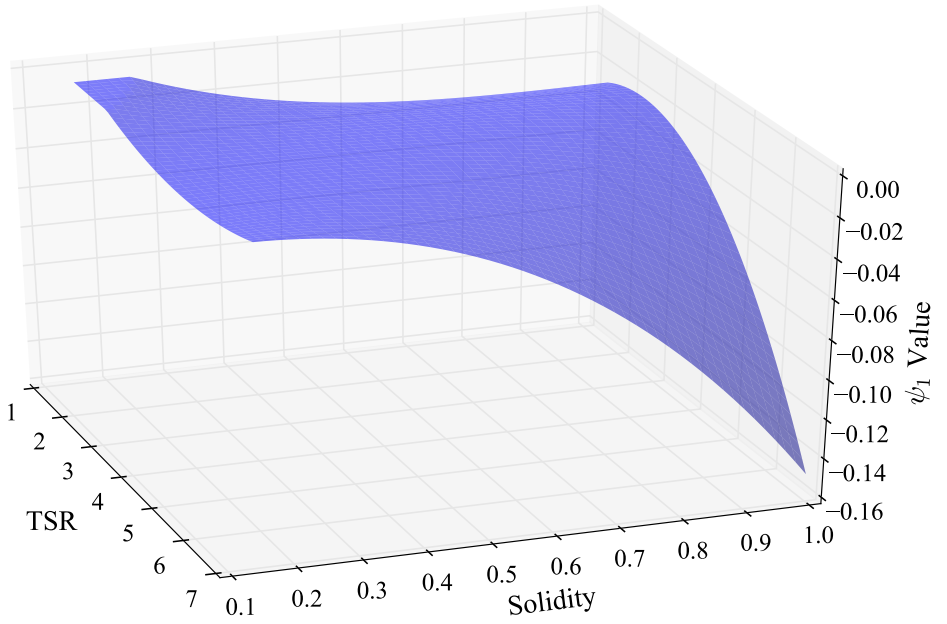

Figure B.4: The polynomial surface used to calculate ψ_1 as a function of TSR and solidity.

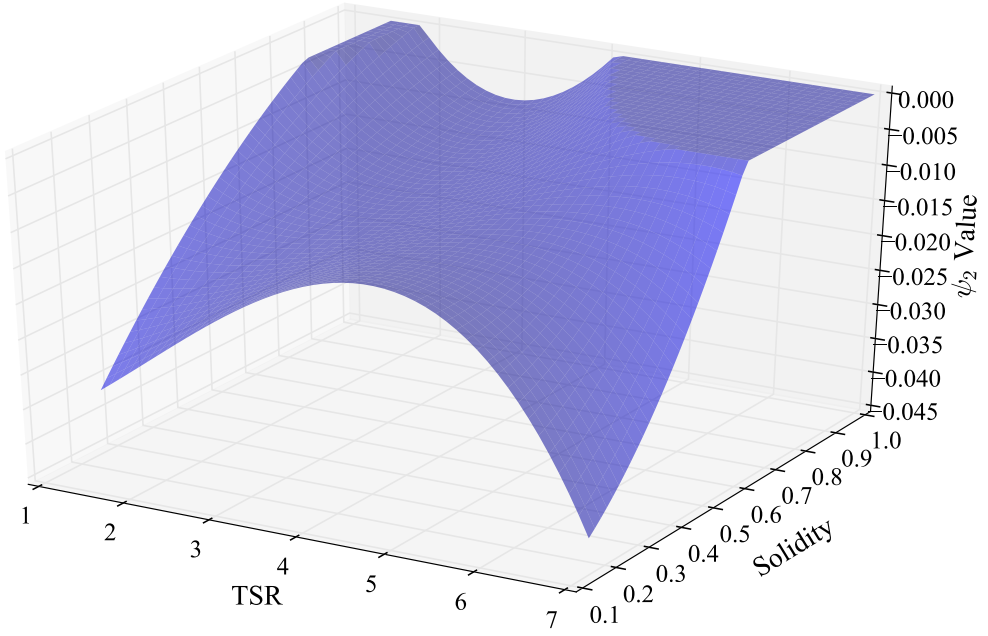

Figure B.5: The polynomial surface used to calculate ψ_2 as a function of TSR and solidity.

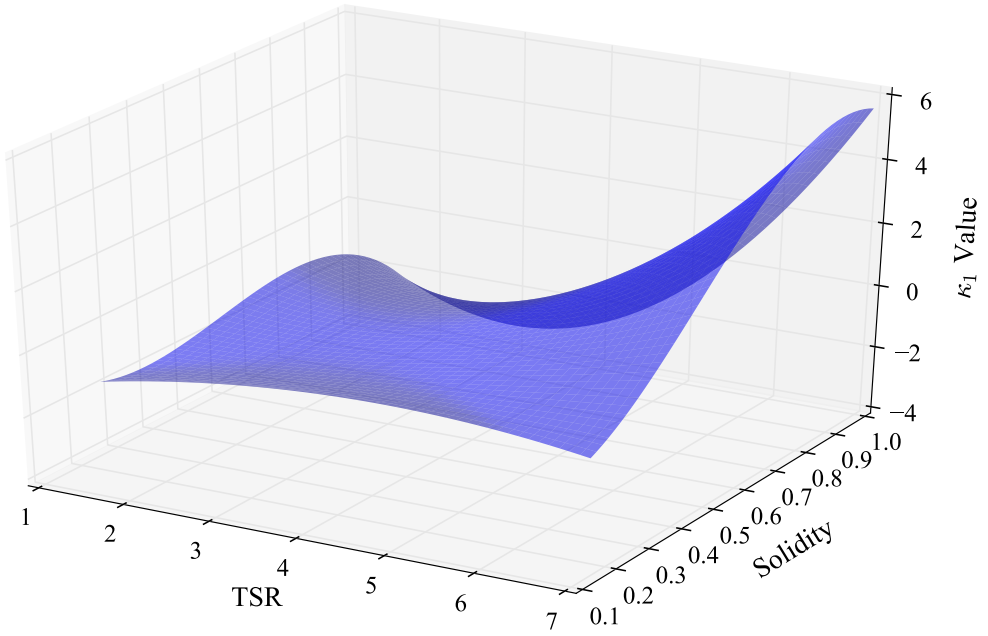

Figure B.6: The polynomial surface used to calculate κ_1 as a function of TSR and solidity.

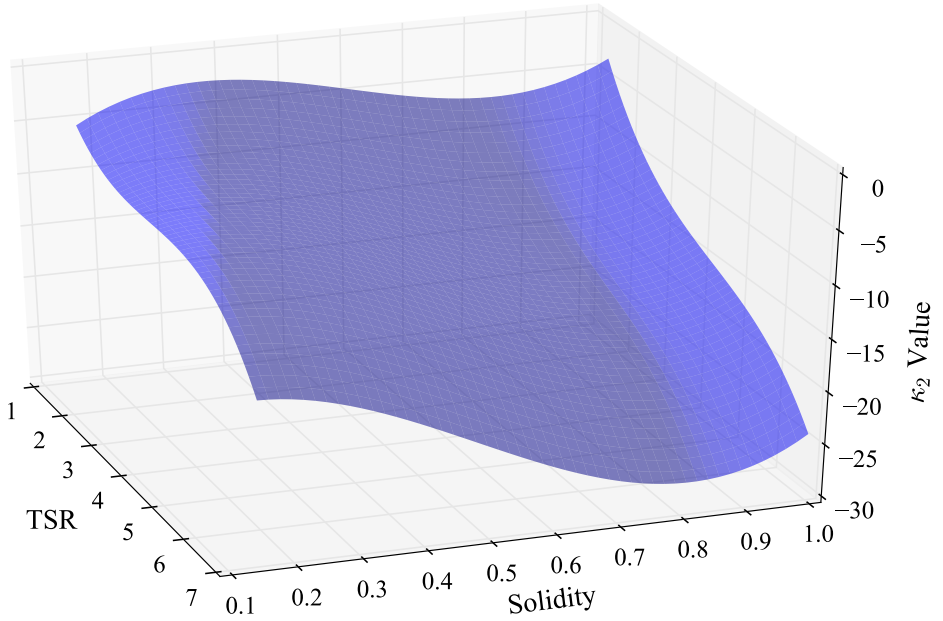

Figure B.7: The polynomial surface used to calculate κ_2 as a function of TSR and solidity.

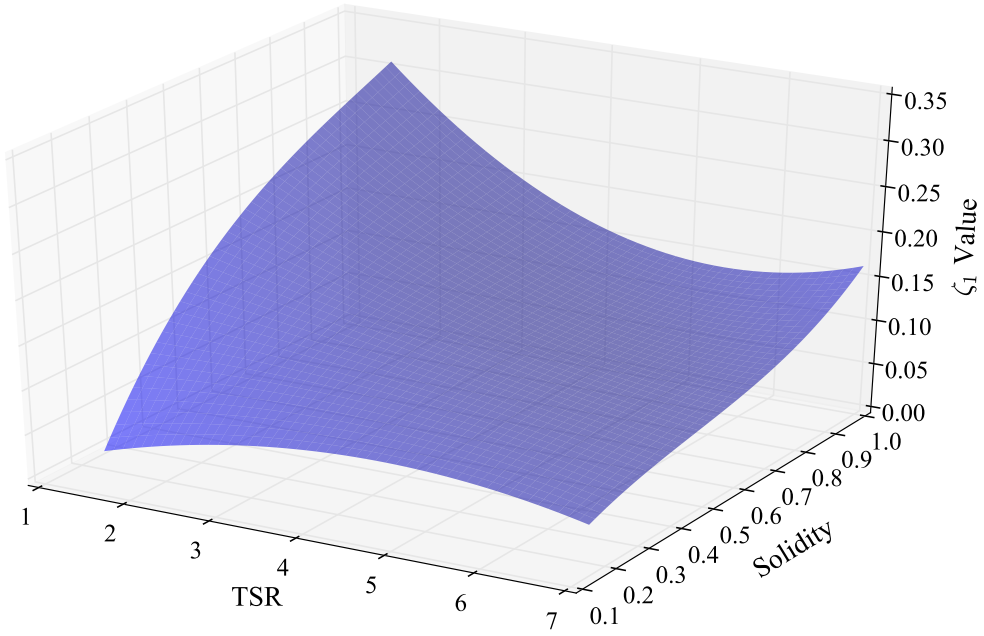

Figure B.8: The polynomial surface used to calculate ζ_1 as a function of TSR and solidity.

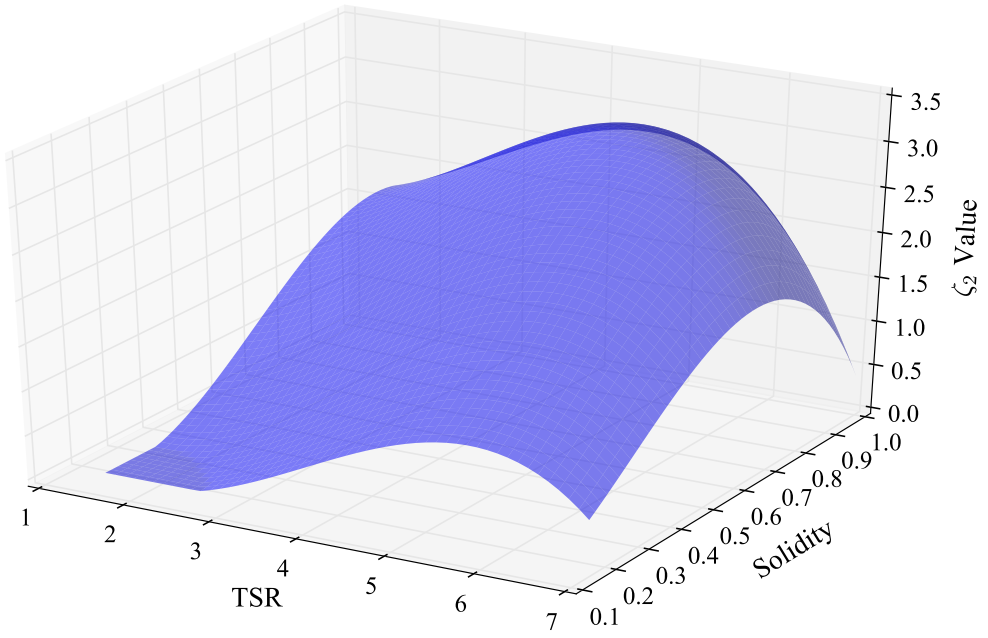

Figure B.9: The polynomial surface used to calculate ζ_2 as a function of TSR and solidity.

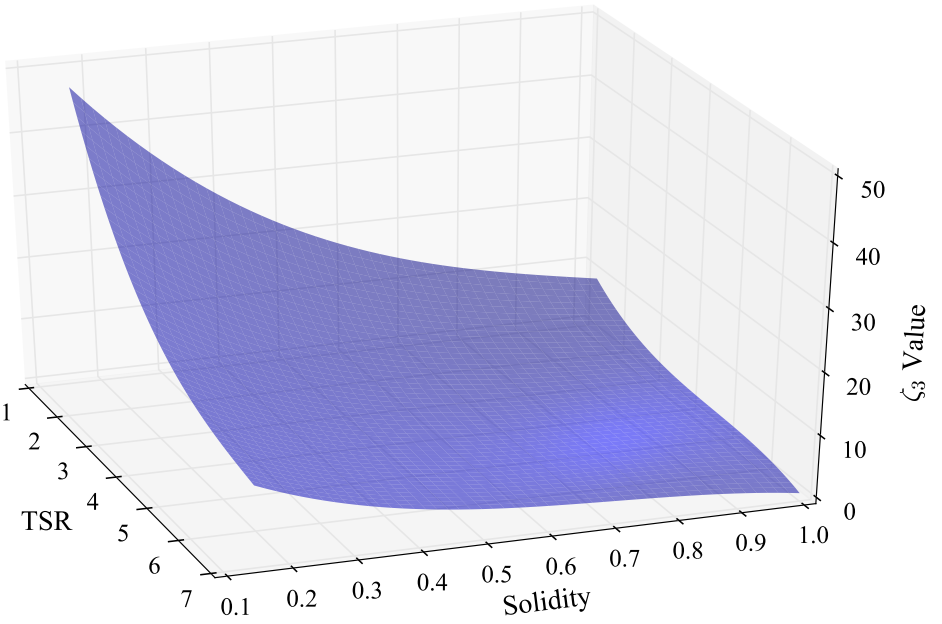

Figure B.10: The polynomial surface used to calculate ζ_3 as a function of TSR and solidity.

APPENDIX C. BPM TURBINE ACOUSTIC EQUATIONS

In Chapter 4, the BPM turbine acoustic equations were described briefly in regards to their use in predicting turbine noise for wind farm layout optimization with noise constraints. This appendix covers the equations in more depth describing each of the equations and their use in the overall acoustic calculation. These equations come from the work of Brooks, Pope, and Marcolini [5] and are divided by the different sources of sound from the turbine blade: turbulent-boundary-layer-trailing-edge, separation-stall, laminar-boundary-layer-vortex-shedding, trailing-edge-bluntness-vortex-shedding, and tip-vortex-shedding noise. The final sound pressure level (SPL) is calculated in decibels (dB). The code that implements these equations used in this thesis can be found at `https://github.com/byuflowlab/bpm-turbine-acoustics`.

C.1 Turbulent-Boundary-Layer-Trailing-Edge/Separation-Stall Noise

The first source of noise comes from the trailing edge of the turbine blade in the turbulent flow region. At high enough angles of attack, noise from the separated airflow at stall come into play. This source of noise is calculated by:

$$SPL_{TBLTE} = 10\log\left(10^{SPL_p/10} + 10^{SPL_s/10} + 10^{SPL_\alpha/10}\right) \tag{C.1}$$

where

$$\begin{aligned} SPL_p &= 10\ \log\left(\frac{\delta_p^* M^5 L\overline{D}_h}{r_e^2}\right) + A\left(\frac{St_p}{St_1}\right) + (K_1 - 3) + \Delta K_1 \\ SPL_s &= 10\ \log\left(\frac{\delta_s^* M^5 L\overline{D}_h}{r_e^2}\right) + A\left(\frac{St_s}{St_1}\right) + (K_1 - 3) \\ SPL_\alpha &= 10\ \log\left(\frac{\delta_s^* M^5 L\overline{D}_h}{r_e^2}\right) + B\left(\frac{St_s}{St_2}\right) + K_2 \end{aligned} \tag{C.2}$$

If the angle of attack (α_*) is greater than 12.5° or γ_0 (described later in this section), then separation-stall noise occurs and the equations become:

$$\begin{aligned} SPL_p &= -\infty \\ SPL_s &= -\infty \\ SPL_\alpha &= 10\ \log\left(\frac{\delta_s^* M^5 L \overline{D}_l}{r_e^2}\right) + A'\left(\frac{St_s}{St_2}\right) + K_2 \end{aligned} \tag{C.3}$$

The variables δ_p^* and δ_s^* represent the boundary layer displacement thickness for the pressure and suction side of the blade, respectively, M is the Mach number, L is the length of the blade section, r_e is the distance between the turbine blade and the observer, and $\overline{D}_h$ and $\overline{D}_l$ represent the directivity functions:

$$\begin{aligned} \overline{D}_h(\Theta_e, \Phi_e) &\approx \frac{2\ \sin^2(\Theta_e/2)\ \sin^2\Phi_e}{(1+M\ \cos\Theta_e)[1+(M-M_c)\ \cos\Theta_e]^2} \\ \overline{D}_l(\Theta_e, \Phi_e) &\approx \frac{\sin^2\Theta_e\ \sin^2\Phi_e}{(1+M\ \cos\Theta_e)^4} \end{aligned} \tag{C.4}$$

In these equations, M_c represents the convective Mach number ($0.8M$ for this research) and Θ_e and Φ_e are angular positions from the blade to the observer in regards to the blade chord reference and span reference, respectively.

The Strouhal definitions are as follows:

$$\begin{aligned} St_p &= \frac{f\delta_p^*}{V} \\ St_s &= \frac{f\delta_s^*}{V} \end{aligned} \tag{C.5}$$

$$St_1 = 0.002M^{-0.6} \tag{C.6}$$

$$\overline{St}_1 = \frac{St_1 + St_2}{2} \tag{C.7}$$

$$St_2 = St_1 \times \begin{cases} 1 & (\alpha_* < 1.33°) \\ 10^{0.0054(\alpha_* - 1.33)^2} & (1.33° \leq \alpha_* \leq 12.5°) \\ 4.72 & (12.5° < \alpha_*) \end{cases} \tag{C.8}$$

where f represents the frequency of the noise produced. V represents the local mean speed of the wind over the blade calculated by:

$$V = \sqrt{(\Omega R)^2 + U_\infty^2} \tag{C.9}$$

where Ω is the rotation rate, R is the local turbine radius, and U_∞ is the free stream wind velocity. The spectral shape functions for A are:

$$A(a) = A_{min}(a) + A_R(a_0)[A_{max}(a) - A_{min}(a)] \tag{C.10}$$

$$A_{min}(a) = \begin{cases} \sqrt{67.552 - 886.788a^2} - 8.219 & (a < 0.204) \\ -32.665a + 3.981 & (0.204 \leq a \leq 0.244) \\ -142.795a^3 + 103.656a^2 - 57.757a + 6.006 & (0.224 < a) \end{cases} \tag{C.11}$$

$$A_{max}(a) = \begin{cases} \sqrt{67.552 - 886.788a^2} - 8.219 & (a < 0.13) \\ -15.901a + 1.098 & (0.13 \leq a \leq 0.321) \\ -4.669a^3 + 3.491a^2 - 16.699a + 1.149 & (0.321 < a) \end{cases} \tag{C.12}$$

$$a = |\log(St/St_{peak})| \tag{C.13}$$

$$A_R(a_0) = \frac{-20 - A_{min}(a_0)}{A_{max}(a_0) - A_{min}(a_0)} \tag{C.14}$$

$$a_0(R_c) = \begin{cases} 0.57 & (R_c < 9.52 \times 10^4) \\ (-9.57 \times 10^{-13})(R_c - 8.57 \times 10^5)^2 + 1.13 & (9.52 \times 10^4 \leq R_c \leq 8.57 \times 10^5) \\ 1.13 & (8.57 \times 10^5 < R_c) \end{cases} \tag{C.15}$$

where R_c is the Reynolds number with respect to the blade's chord length, St is either St_p or St_s, and St_{peak} is St_1, $\overline{St}_1$, or St_2. To produce the spectral function A', the same equations are used replacing R_c with $3R_c$.

The spectral shape functions for B are:

$$B(b) = B_{min}(b) + B_R(b_0)[B_{max}(b) - B_{min}(b)] \tag{C.16}$$

$$B_{min}(b) = \begin{cases} \sqrt{16.888 - 886.788b^2} - 4.109 & (b < 0.13) \\ -83.607b + 8.138 & (0.13 \leq b \leq 0.145) \\ -817.810b^3 + 355.210b^2 - 135.024b + 10.619 & (0.145 < b) \end{cases} \tag{C.17}$$

$$B_{max}(b) = \begin{cases} \sqrt{16.888 - 886.788b^2} - 4.109 & (b < 0.10) \\ -31.330b + 1.854 & (0.10 \leq b \leq 0.187) \\ -80.541b^3 + 44.17b^2 - 39.381b + 2.344 & (0.187 < b) \end{cases} \tag{C.18}$$

$$b = |\log(St_s/St_2)| \tag{C.19}$$

$$B_R(b_0) = \frac{-20 - B_{min}(b_0)}{B_{max}(b_0) - B_{min}(b_0)} \tag{C.20}$$

$$b_0(R_c) = \begin{cases} 0.30 & (R_c < 9.52 \times 10^4) \\ (-4.48 \times 10^{-13})(R_c - 8.57 \times 10^5)^2 + 0.56 & (9.52 \times 10^4 \leq R_c \leq 8.57 \times 10^5) \\ 0.56 & (8.57 \times 10^5 < R_c) \end{cases} \tag{C.21}$$

The amplitude function K_1 and its level adjustment of nonzero angles ΔK_1 are given by:

$$K_1 = \begin{cases} -4.31\ \log(R_c) + 156.3 & (R_c < 2.47 \times 10^5) \\ -9.0\ \log(R_c) + 181.6 & (2.47 \times 10^5 \leq R_c \leq 8.0 \times 10^5) \\ 128.5 & (8.0 \times 10^5 < R_c) \end{cases} \tag{C.22}$$

$$\Delta K_1 = \begin{cases} \alpha_* \left[1.43\ \log\left(R_{\delta_p^*} \right) - 5.29 \right] & (R_{\delta_p^*} \leq 5000) \\ 0 & (5000 < R_{\delta_p^*}) \end{cases} \tag{C.23}$$

where $R_{\delta_p^*}$ is the Reynolds number with respect to the displacement thickness on the pressure side. The amplitude function K_2 is given by:

$$K_2 = K_1 + \begin{cases} -1000 & (\alpha_* < \gamma_0 - \gamma) \\ \sqrt{\beta^2 - (\beta/\gamma)^2(\alpha_* - \gamma_0)^2} + \beta_0 & (\gamma_0 - \gamma \leq \alpha_* \leq \gamma_0 + \gamma) \\ -12 & (\gamma_0 + \gamma < \alpha_*) \end{cases} \tag{C.24}$$

$$\begin{aligned} \gamma &= 27.094M + 3.31 \\ \gamma_0 &= 23.43M + 4.651 \\ \beta &= 72.65M + 10.74 \\ \beta_0 &= -34.19M - 13.82 \end{aligned} \tag{C.25}$$

C.2 Laminar-Boundary-Layer-Vortex-Shedding Noise

The second source of noise comes from the vortex shedding with the laminar boundary only when the flow is laminar and untripped over the blade surface. This source of noise is calculated with the equation:

$$SPL_{LBLVS} = 10\ \log\left(\frac{\delta_p M^5 L \overline{D}_h}{r_e^2} \right) + G_1\left(\frac{St'}{St'_{peak}} \right) + G_2\left[\frac{R_c}{(R_c)_0} \right] + G_3(\alpha_*) \tag{C.26}$$

The Strouhal definitions are given by:

$$St' = \frac{f\delta_p}{V} \tag{C.27}$$

$$St'_1 = \begin{cases} 0.18 & (R_c \leq 1.3\times10^5) \\ 0.001756R_c^{0.3931} & (1.3\times10^5 < R_c \leq 4.0\times10^5) \\ 0.28 & (4.0\times10^5 < R_c) \end{cases} \tag{C.28}$$

$$St'_{peak} = St'_1 \times 10^{-0.04\alpha_*} \tag{C.29}$$

where δ_p is the boundary layer thickness on the pressure side of the blade.

The spectral shape function G_1 is defined by:

$$G_1(e) = \begin{cases} 39.8\ \log(e) - 11.12 & (e \leq 0.5974) \\ 98.409\ \log(e) + 2.0 & (0.5974 < e \leq 0.8545) \\ -5.076 + \sqrt{2.484 - 506.23[\log(e)]^2} & (0.8545 < e \leq 1.17) \\ -98.409\ \log(e) + 2.0 & (1.17 < e \leq 1.674) \\ -39.8\ \log(e) - 11.12 & (1.674 < e) \end{cases} \tag{C.30}$$

$$e = St'/St'_{peak} \tag{C.31}$$

The peak scaled level shape curve G_2 is defined by:

$$G_1(e) = \begin{cases} 77.852\ \log(d) + 15.328 & (d \leq 0.3237) \\ 65.188\ \log(d) + 9.125 & (0.3237 < d \leq 0.5689) \\ -114.052[\log(d)]^2 & (0.5689 < d \leq 1.7579) \\ -65.188\ \log(d) + 9.125 & (1.7579 < d \leq 3.0889) \\ -77.852\ \log(d) + 15.328 & (3.0889 < d) \end{cases} \tag{C.32}$$

$$d = R_c/(R_c)_0 \tag{C.33}$$

$$(R_c)_0 = \begin{cases} 10^{0.215\alpha_* + 4.978} & (\alpha_* \leq 3.0) \\ 10^{0.120\alpha_* + 5.263} & (3.0 < \alpha_*) \end{cases} \tag{C.34}$$

The angle-dependent level for the shape curve G_3 is given by:

$$G_3(\alpha_*) = 171.04 - 3.03\alpha_* \tag{C.35}$$

C.3 Trailing-Edge-Bluntness-Vortex-Shedding Noise

The third source of noise comes from the vortex shedding that occurs from the air moving over the bluntness of the trailing edge of the blade and is calculated by:

$$SPL_{TEBVS} = 10 \log\left(\frac{hM^{5.5}L\overline{D}_h}{r_e^2}\right) + G_4\left(\frac{h}{\delta^*_{avg}}, \Psi\right) + G_5\left(\frac{h}{\delta^*_{avg}}, \Psi, \frac{St'''}{St'''_{peak}}\right) \tag{C.36}$$

The variable Ψ represents the solid angle between the sloping surfaces upstream of the trailing edge, which for a flat plate $\Psi = 0^\circ$ and for the NACA 0012 airfoil (for which all of the equations were developed) $\Psi = 14^\circ$. The variable h represents the trailing edge thickness (calculated as 1% of the chord length) and δ^*_{avg} represents the average boundary-layer displacement thickness given by:

$$\delta^*_{avg} = \frac{\delta^*_p + \delta^*_s}{2} \tag{C.37}$$

The Strouhal definitions are given by:

$$St''' = \frac{fh}{V} \tag{C.38}$$

$$St'''_{peak} = \begin{cases} \frac{0.212 - 0.0045\Psi}{1 + 0.235\left(h/\delta^*_{avg}\right)^{-1} - 0.0132\left(h/\delta^*_{avg}\right)^{-2}} & (0.2 \leq h/\delta^*_{avg}) \\ 0.1\left(h/\delta^*_{avg}\right) + 0.095 - 0.00243\Psi & (h/\delta^*_{avg} < 0.2) \end{cases} \tag{C.39}$$

The peak level of the spectrum G_4 is calculated by:

$$G_4\left(h/\delta^*_{avg},\Psi\right)=\begin{cases}17.5\,\log\left(h/\delta^*_{avg}\right)+157.5-1.114\Psi & (h/\delta^*_{avg}\le 5)\\ 169.7-1.114\Psi & (5<h/\delta^*_{avg})\end{cases} \tag{C.40}$$

The shape of the spectrum G_5 is given by:

$$G_5\left(\frac{h}{\delta^*_{avg}},\Psi,\frac{St'''}{St'''_{peak}}\right)=(G_5)_{\Psi=0^\circ}+0.0714\Psi[(G_5)_{\Psi=14^\circ}-(G_5)_{\Psi=0^\circ}] \tag{C.41}$$

$$(G_5)_{\Psi=14^\circ}=\begin{cases}m\eta+k & (\eta<\eta_0)\\ 2.5\sqrt{1-(\eta/\mu)^2}-2.5 & (\eta_0\le\eta<0)\\ \sqrt{1.5625-1194.99\eta^2}-1.25 & (0\le\eta<0.03616)\\ -155.543\eta+4.375 & (0.03616\le\eta)\end{cases} \tag{C.42}$$

$$\eta=\log(St'''/St'''_{peak}) \tag{C.43}$$

$$\mu=\begin{cases}0.1221 & (h/\delta^*_{avg}<0.25)\\ -0.2175(h/\delta^*_{avg})+0.1755 & (0.25\le h/\delta^*_{avg}<0.62)\\ -0.0308(h/\delta^*_{avg})+0.0596 & (0.62\le h/\delta^*_{avg}<1.15)\\ 0.0242 & (1.15\le h/\delta^*_{avg})\end{cases} \tag{C.44}$$

$$m=\begin{cases}0 & (h/\delta^*_{avg}\le 0.02)\\ 68.724(h/\delta^*_{avg})-1.35 & (0.02<h/\delta^*_{avg}\le 0.5)\\ 308.475(h/\delta^*_{avg})-121.23 & (0.5<h/\delta^*_{avg}\le 0.62)\\ 224.811(h/\delta^*_{avg})-69.35 & (0.62<h/\delta^*_{avg}\le 1.15)\\ 1583.28(h/\delta^*_{avg})-1631.59 & (1.15<h/\delta^*_{avg}\le 1.2)\\ 268.344 & (1.2<h/\delta^*_{avg})\end{cases} \tag{C.45}$$

$$\eta_0=-\sqrt{\frac{m^2\eta^4}{6.25+m^2\eta^2}} \tag{C.46}$$

$$k = 2.5\sqrt{1 - \left(\frac{\eta_0}{\eta}\right)} - 2.5 - m\eta_0 \tag{C.47}$$

The spectrum $(G_5)_{\Psi=0^\circ}$ is calculated using the same procedure as $(G_5)_{\Psi=14^\circ}$ and using $(h/\delta^*_{avg})'$ in place of (h/δ^*_{avg}), which is calculated by:

$$\left(\frac{h}{\delta^*_{avg}}\right)' = 6.724\left(\frac{h}{\delta^*_{avg}}\right)^2 - 4.019\left(\frac{h}{\delta^*_{avg}}\right) + 1.107 \tag{C.48}$$

C.4 Tip-Vortex-Shedding Noise

The final source of noise that is considered in these equations is from the vortex shedding on the tips of the blades in a turbulent boundary layer. This is calculated by:

$$SPL_{TBLTV} = 10\ \log\left(\frac{M^2 M_{max}^2 l^2 \overline{D}_h}{r_e^2}\right) - 30.5(\log St'' + 0.3)^2 + 126 \tag{C.49}$$

The Strouhal number in this case is given by:

$$St'' = \frac{fl}{V_{max}} \tag{C.50}$$

Other terms used in the noise equation are given as follows:

$$\begin{aligned} M_{max} &\approx (1 + 0.036\alpha'_{tip})M \\ V_{max} &= c_0 M_{max} \end{aligned} \tag{C.51}$$

where c_0 is the speed of sound of the air and α'_{tip} is the corrected angle of attack of the tip of the blade. As all of the equations were developed for the NACA 0012 airfoil, corrections must be made for different airfoils used in turbines. Brooks et al. provides an equation for the generalized tip angle of attack involving derivatives [5], but for this model, a cubic spline of correction factors at different aspect ratios between 2.0 and 24.0 is used based on earlier work by Brooks and Marcolini [67]. The spanwise extent of the vortex shedding, l, is defined for a round tip by:

$$l \approx 0.008\alpha'_{tip}c \tag{C.52}$$

and for a flat tip by:

$$l = c \times \begin{cases} 0.0230 + 0.0169\alpha'_{tip} & (0^\circ \leq \alpha'_{tip} \leq 2^\circ) \\ 0.0378 + 0.0095\alpha'_{tip} & (2^\circ < \alpha'_{tip}) \end{cases} \tag{C.53}$$

where c is the chord length of the blade segment.

C.5 Boundary-Layer Thickness and Displacement Thickness Calculations

In the previous equations, the boundary-layer thickness δ and displacement thickness δ^* are often used in the noise calculations. These parameters are calculated for tripped and untripped (natural transition from laminar to turbulent) conditions of the airflow over the airfoils. The zero-angle of attack thickness and displacement thickness (indicated by the 0 subscript) for the tripped case is calculated by:

$$\begin{aligned} \delta_0 &= c \left[10^{[1.892 - 0.9045 \ \log R_c + 0.0596(\log R_c)^2]} \right] \\ \delta_0^* &= c \times \begin{cases} 0.0601 R_c^{-0.114} & (R_c \leq 0.3 \times 10^6) \\ 10^{[3.411 - 1.5397 \ \log R_c + 0.1059(\log R_c)^2]} & (R_c > 0.3 \times 10^6) \end{cases} \end{aligned} \tag{C.54}$$

and for the untripped case:

$$\begin{aligned} \delta_0 &= c \left[10^{[1.6569 - 0.9045 \ \log R_c + 0.0596(\log R_c)^2]} \right] \\ \delta_0^* &= c \left[10^{[3.0187 - 1.5397 \ \log R_c + 0.1059(\log R_c)^2]} \right] \end{aligned} \tag{C.55}$$

The boundary-layer thickness and displacement thickness for the pressure side of the blade for both tripped and untripped cases is calculated by:

$$\begin{aligned} \delta_p &= \delta_0 \left[10^{[-0.04175\alpha_* + 0.00106\alpha_*^2]} \right] \\ \delta_p^* &= \delta_0^* \left[10^{[-0.0432\alpha_* + 0.00113\alpha_*^2]} \right] \end{aligned} \tag{C.56}$$

The boundary-layer thickness and displacement thickness for the suction side of the blade for the tripped case is calculated by:

$$\delta_s = \delta_0 \times \begin{cases} 10^{0.0311\alpha_*} & (0^\circ \leq \alpha_* \leq 5^\circ) \\ 0.3468\left(10^{0.1231\alpha_*}\right) & (5^\circ < \alpha_* \leq 12.5^\circ) \\ 5.718\left(10^{0.0258\alpha_*}\right) & (12.5^\circ < \alpha_* \leq 25^\circ) \end{cases}$$
$$\delta_s^* = \delta_0^* \times \begin{cases} 10^{0.0679\alpha_*} & (0^\circ \leq \alpha_* \leq 5^\circ) \\ 0.381\left(10^{0.1516\alpha_*}\right) & (5^\circ < \alpha_* \leq 12.5^\circ) \\ 14.296\left(10^{0.0258\alpha_*}\right) & (12.5^\circ < \alpha_* \leq 25^\circ) \end{cases} \tag{C.57}$$

and for the untripped case:

$$\delta_s = \delta_0 \times \begin{cases} 10^{0.03114\alpha_*} & (0^\circ \leq \alpha_* \leq 7.5^\circ) \\ 0.0303\left(10^{0.2336\alpha_*}\right) & (7.5^\circ < \alpha_* \leq 12.5^\circ) \\ 12\left(10^{0.0258\alpha_*}\right) & (12.5^\circ < \alpha_* \leq 25^\circ) \end{cases}$$
$$\delta_s^* = \delta_0^* \times \begin{cases} 10^{0.0679\alpha_*} & (0^\circ \leq \alpha_* \leq 7.5^\circ) \\ 0.0162\left(10^{0.3066\alpha_*}\right) & (7.5^\circ < \alpha_* \leq 12.5^\circ) \\ 52.42\left(10^{0.0258\alpha_*}\right) & (12.5^\circ < \alpha_* \leq 25^\circ) \end{cases} \tag{C.58}$$

C.6 1/3 Octave Band Frequency and A-Weighting

To determine the frequencies f that the noise would be calculated over, a 1/3 octave band frequency spectrum is used. As noise at each frequency is perceived differently to the human ear, weighting is done to each of the calculated SPLs to account for the difference. The Table C.1 shows the frequencies used in the equations and the A-weighting performed for the sound correction (in dB; $SPL_{weighted}(f) = SPL_{calculated}(f) + A(f)$). These A-weighting values can be calculated for any frequency (f) using the equations:

$$Ra(f) = \frac{12200^2 \cdot f^4}{(f^2+20.6^2)\cdot(f^2+12200^2)\cdot\sqrt{f^2+107.7^2}\cdot\sqrt{f^2+737.9^2}}$$
$$A(f) = 2 + 20\ \log\left[Ra(f)\right] \tag{C.59}$$

Table C.1: 1/3 Octave Band Frequencies (f) and Respective A-Weighting Values ($A(f)$)

f (Hz)	$A(f)$ (dB)	f (Hz)	$A(f)$ (dB)	f (Hz)	$A(f)$ (dB)	f (Hz)	$A(f)$ (dB)
100.0	-19.145	500.0	-3.248	2500.0	1.271	12500.0	-4.250
125.0	-16.190	630.0	-1.908	3150.0	1.202	16000.0	-6.701
160.0	-13.244	800.0	-0.795	4000.0	0.964	20000.0	-9.341
200.0	-10.847	1000.0	0.000	5000.0	0.556	25000.0	-12.322
250.0	-8.675	1250.0	0.576	6300.0	-0.114	31500.0	-15.694
315.0	-6.644	1600.0	0.993	8000.0	-1.144	40000.0	-19.402
400.0	-4.774	2000.0	1.202	10000.0	-2.488		

C.7 Final SPL Calculation

The final SPL calculation is done by combining the sources of noise described in the previous section with the A-weighting applied to the SPL values at each frequency. The blades are also broken up into segments and the SPL is calculated with respect to each segment as well. The first step is to calculate the distance (r_e) from an observer position to the source of noise on the trailing edge of the turbine blade as well as the directivity angles (Θ_e and Φ_e) used for the SPL calculations (see Fig. 2.3). The equations used for this process come from the work of Vargas in which the turbine blade is divided up into segments and each r_e, Θ_e, and Φ_e is calculated at each blade segment as well as at each rotational position (β_r) with 0° starting vertically upward [68]. Vargas indicated that this process is to be done for at least eight 45° increments and then a root mean square is taken of the SPL calculations for each rotational increment [68]. The equations begin with transforming a given observer location with respect to the turbine ($(x,y,z)_t$) to the coordinate system of the turbine hub ($(x,y,z)_o$):

$$\begin{aligned} x_o &= x_t \\ y_o &= y_t \\ z_o &= z_t - H_{hub} \end{aligned} \tag{C.60}$$

where x_o is the lateral position of an observer from the turbine, y_o is the downstream position of an observer from the turbine, and z_o is the height of an observer with respect to the hub height, H_{hub}. The next step is to calculate the position of the trailing edge of the blade in the lateral and height coordinates (x_s and z_s):

$$x_s = \sin(\beta_r)d - \cos(\beta_r)c_2$$
$$z_s = \cos(\beta_r)d + \sin(\beta_r)c_2 \tag{C.61}$$

where d is the radial position along the blade from the hub and c_2 is the distance from the pitch axis to the trailing edge. The observer position with respect to the trailing edge in the lateral and height coordinates (x'_e and z'_e) can then be calculated:

$$x'_e = x_o - x_s$$
$$z'_e = z_o - z_s \tag{C.62}$$

As the blades rotate incrementally, the observer position with respect to the trailing edge must be rotated with respect to β_r (x_e and z_e):

$$\theta = \pi - \beta_r$$
$$x_e = \cos(\theta)x'_e + \sin(\theta)z'_e \tag{C.63}$$
$$z_e = -\sin(\theta)x'_e + \cos(\theta)z'_e$$

Using these final observer positions transformed to the correct directivity coordinates (the position with respect to the trailing edge of the blade with the blade moving forward into the wind), the observer distance and directivity angles can be computed:

$$r_e = \sqrt{x_e^2 + y_o^2 + z_e^2}$$
$$\Theta_e = \arctan\left(\frac{\sqrt{y_o^2 + z_e^2}}{xe}\right) \tag{C.64}$$
$$\Phi_e = \arctan\left(\frac{y_o}{z_e}\right)$$

One concern presented by Vargas is that Φ_e becomes critical at angles of 0° and 180° leading to unrealistic SPL values [68]. To protect against this, the equations in this thesis use a quadratic smoothing based on the general equation:

$$\Phi_{e,smoothed} = 0.1\Phi_e^2 + 2.5 \tag{C.65}$$

when Φ_e is within 5 degrees of 0° and $\pm 180^\circ$. These values are then used in each of the SPL calculations to produce SPL_{TBLTE}, SPL_{LBLVS}, SPL_{TEBVS}, and SPL_{TBLTV} for each blade segment (with the exception of SPL_{TBLTV} that is calculated only at the tip segment) and frequency. SPLs are combined across N blade segments or N frequencies using the equation:

$$SPL = 10 \log \left(\sum_{i=1}^{N} 10^{SPL_i/10} \right) \tag{C.66}$$

The SPLs from each noise source are then combined, taking into account the noise sources from each blade at the same time, using the same process:

$$SPL_{total} = 10 \log \left(10^{SPL_{TBLTE}/10} + 10^{SPL_{LBLVS}/10} + 10^{SPL_{TEBVS}/10} + 10^{SPL_{TBLTV}/10} \right) \tag{C.67}$$

C.8 Adjustments for VAWT Acoustics

As VAWTs are fundamentally different in their operation than HAWTs, a series of changes are necessary to the BPM equations to account for the differences. The first change is that the directivity angles must be calculated differently than the method presented above. As the blades will always be oriented vertically changing coordinates to an observer due to the vertical-axis rotation of the turbine, the method begins by moving the observer location to the turbine hub as before (Eq. (C.60)) and then calculate the trailing edge position of the blades in the lateral and downstream coordinates (x_s and y_s):

$$\begin{aligned} x_s &= -\cos(\beta_r)R - \sin(\beta_r)c_2 \\ y_s &= -\sin(\beta_r)R + \cos(\beta_r)c_2 \end{aligned} \tag{C.68}$$

for a counter-clockwise rotation from above (positive) and for a clockwise rotation (negative):

$$\begin{aligned} x_s &= -\cos(\beta_r)R + \sin(\beta_r)c_2 \\ y_s &= -\sin(\beta_r)R - \cos(\beta_r)c_2 \end{aligned} \tag{C.69}$$

where β_r is the rotational position with 0° starting at the point where the blade is on the lateral side of the turbine beginning to move towards the flow of the wind of a counter-rotating turbine

and R is the turbine radius. The observer location with respect to the trailing edge in the lateral, downstream, and height coordinates (x'_e, y'_e, and z_e) is than calculated by:

$$\begin{aligned} x'_e &= x_o - xs \\ y'_e &= y_o - ys \\ z_e &= z_o - ht \end{aligned} \tag{C.70}$$

with ht representing the height position along the blade from the bottom of the turbine (similar to d in Eq. (C.61)). The positions are then rotated with respect to β_r (x_e and y_e):

$$\begin{aligned} \theta &= \beta_r \pm \frac{\pi}{2} \\ x_e &= \cos(\theta)x'_e + \sin(\theta)y'_e \\ y_e &= -\sin(\theta)x'_e + \cos(\theta)y'_e \end{aligned} \tag{C.71}$$

with the $\pm$ being positive for counter-clockwise rotation and negative for clockwise rotation as viewed from above. Finally, r_e, Θ_e, and Φ_e are all computed using Eq. (C.64) with y_e replacing y_o. Smoothing is also performed for Θ_e and Φ_e near 0° and 180° using the method described by Eq. (C.65).

The wind velocity over each blade changes by rotational position of the turbine rather than by the radial position along the blade. At each rotational position (β_r), the velocities of the free stream wind (U_∞), nearby wake interference (u_w and v_w), and the rotational motion of the blades are combined in the x- and y-directions to calculate the velocity over each blade (V) using the equations:

$$\begin{aligned} V_x &= U_\infty + u_w + \Omega R\cos(\beta_r) \\ V_y &= v_w + \Omega R\sin(\beta_r) \\ V &= \sqrt{V_x^2 + V_y^2} \end{aligned} \tag{C.72}$$

Because VAWTs have two blade tips, SPL_{TBLTV} is calculated twice, once at each tip, and the noise sources are then combined using in Eqs. (C.66) and (C.67).